DIRECTLY BONDED ELECTROCHEMICAL SENSOR FOR LEAD DETECTION IN WATER

FULLY INTEGRATED ELECTROCHEMICAL SENSOR BASED ON SURFACE ACTIVATED COPPER/POLYMER BONDING FOR LEAD DETECTION

By

MD TAUFIQUE ZAMAN REDHWAN, B.Sc.

A Thesis Submitted to the School of Graduate Studies in Partial Fulfilment of the Requirements for the Degree of Master of Applied Science

McMaster University
Hamilton, Ontario

MASTER OF APPLIED SCIENCE (2018)
(Electrical and Computer Engineering)

TITLE: Fully Integrated Electrochemical Sensor Based on Surface Activated Copper/Polymer Bonding for Lead Detection

AUTHOR: Md Taufique Zaman Redhwan, B.Sc. (North South University, Dhaka, Bangladesh)

SUPERVISOR: Dr. Yaser M. Haddara
Dr. Matiar M. R. Howlader (Co-supervisor)

NUMBER OF PAGES: xxi, 131

Lay Abstract

Lead contamination in tap water has major health risks for which monitoring of its levels is important. In this thesis, we develop a low-cost copper/polymer-based lead sensor. The sensor is fabricated from high-quality metal foil electrodes that are integrated to a polymer substrate by a direct bonding process. This enables strong adhesion of foil-based electrodes to the substrate that is crucial to the sensor performance and packaging integrity. We investigate the bonding mechanism between copper and polymer to understand the fundamentals of materials integration. These findings will lead to the development of polymer-based sensors and integrated systems. The bonded sensor bases are mechanically flexible, which facilitates a rapid and low-cost fabrication process using a laser printer. The developed sensor has a fast response time (30 s) and can detect very low levels of lead, thus making it suitable for water quality monitoring applications in under-developed and developed countries with legacy water systems that have not been upgraded yet.

Abstract

Lead (Pb) levels in tap water below the established water safety guideline are now considered harmful, thus detecting sub-parts-per-billion level Pb is important. This thesis reports on a miniaturized Copper (Cu)−based electrochemical sensor fabricated from thick film electrodes for their superior sensing performance. These thick film electrodes are based on highly conductive rolled-annealed Cu foil that has a compact bulk structure, but these advantages are often offset by the fact that RA Cu foil is difficult to bond to a substrate due to poor film-adhesion property and lack of mechanical interlocks. For this reason, we develop a direct bonding process for Cu/polymer. An integrated three-electrode planar configuration is then fabricated on the bonded specimen to achieve a fully-functional sensor that can detect 0.2 μg/L (0.2 ppb) Pb^{2+} ions from a 100 μL sample in only 30 s. This is the most rapid detection of Pb featured to date by an all Cu-based sensor.

This thesis first focuses on improving substrate adhesion of RA Cu foil to liquid crystal polymer (LCP). This is achieved by a surface activated bonding process where Cu and LCP surfaces are treated with low-power reactive ion etching oxygen plasma followed by low-pressure contact at 230 °C. This treatment produces hydroxyl (OH^-) groups on Cu and LCP surfaces making them highly hydrophilic. When Cu and LCP are contacted and heated, the OH^- chains condense by dehydration and form an intermediate oxide layer. This layer mainly develops as Cu_2O nanoparticles from the plasma-treated Cu side due to

thermal oxidation in air. These nanoparticles diffuse into the polymer substrate when heated under mechanical pressure, resulting in a strongly bonded flexible specimen for the sensor.

A simple, inexpensive, and production-friendly fabrication process is then developed for these sensors. Following direct bonding, flexible Cu/LCP is fed into a LaserJet printer for a one-step transfer of polyester resin−based electrode mask on Cu. This is followed by etching, packaging, and a chlorinating process to achieve a fully-functional integrated sensor. The sensing performance of directly bonded Cu/LCP is comparable to that of commercially available Cu/polyimide (PI) laminate. Our approach holds promise towards realizing low-cost integrated water quality monitoring systems.

Acknowledgements

I want to express my sincere gratitude to Dr. Yaser M. Haddara and Dr. Matiar M. R. Howlader, who have been excellent mentors throughout my graduate study. They have always encouraged an independent thought process and provided me with the necessary guidance on experiment designs, publications, and exploring the fundamentals throughout this work. It has been quite a journey, and truly an honor to have worked with them.

I would like to thank Dr. M. Jamal Deen for granting me access to the Micro- and Nano- Systems lab at McMaster University. Members of his research group have been exceptional peers whose works inspired this research from some aspects. I want to thank Dr. Deen and Dr. Chih-Hung Chen for reviewing this thesis. Dr. Moon Kim from the University of Texas at Dallas is recognized for his support with the high-resolution electron microscopy.

I want to thank Dr. John Bandler for his time and effort behind the rehearsals of a 3MT® presentation of this work. His guidance has helped me to effectively present this work to a larger audience – the response to which has fueled this research to some extent. I want to acknowledge Fangfang Zhang, Arif U. Alam, and Dr. Yiheng Qin for their support at the Micro- and Nano-Systems lab.

This thesis is dedicated to my parents, Dr. Kamruzzaman and Afroza Akhter, and to my wife, Mosarrat Sadia, for their endless love and support.

Table of Contents

List of Figures

List of Tables

List of Abbreviations

Al_2O_3	Aluminum oxide
ASV	Anodic stripping voltammetry
Sb-BDD	Antimony on boron doped diamond
Ar	Argon
Ar-RF	Argon radio frequency
AFM	Atomic force microscope
ATR	Attenuated total reflectance
AE	Auxiliary electrode
BON6	Bi-oxide 6-naptholine acid
Bi	Bismuth
BDD	Boron doped diamond
BF	Bright field
Cd	Cadmium
CDW	Canadian Federal-Provincial-Territorial Committee on Drinking Water
C	Carbon
CNT	Carbon nanotube
CHEMFET	Chemically modified field effect transistor
Cl^-	Chloride ion
Cr	Chromium
CAD	Computer-aided design
Cu_2O	Copper (I) oxide
$CuCl_2$	Copper (II) chloride
CuO	Copper (II) oxide
$Cu(OH)_2$	Copper hydroxide
CV	Cyclic voltammetry
DI	Deionized
DNA	Deoxyribo nucleic acid
DTPA	Diethylenetriaminepentaacetic acid
DSA	Drop shape analysis system
EDS	Energy-dispersive x-ray spectroscope
FAB	Fast atom beam
FET	Field effect transistor
FIB	Focused ion beam
FTIR	Fourier-transform infrared spectroscope
GaAs	Gallium Arsenide

GaP	Gallium Phosphide
Ge	Germanium
GCE	Glassy carbon electrode
GSH	Glutathione
Au	Gold
AuNP	Gold nanoparticle
GFAAS	Graphite furnace atomic absorption spectrometry
HRTEM	High resolution transmission electron microscope
HV	High vacuum
HAADF	High-angle annular dark-field
HCl	Hydrochloric acid
H_2O_2	Hydrogen peroxide
OH^-	Hydroxyl ion
ITO	Indium tin oxide
ICP-AES	Inductively coupled plasma atomic emission spectroscopy
ACP-MS	Inductively coupled plasma mass spectrometry
Fe	Iron
Pb^0	Lead atom
Pb^{2+}	Lead ion
LOD	Limit of detection
LCP	Liquid crystal polymer
LV	Low vacuum
MAC	Maximum acceptable concentration
Hg	Mercury
Cu	Metallic copper
Ag	Metallic silver
N_2	Nitrogen
N_2-MW	Nitrogen microwave
O_2	Oxygen
O	Oxygen atom
O_2-RIE	Oxygen reactive ion etching
PHB	Para-hydronyl benzoic acid
ppb	Parts per billion
ppq	Parts per quadrillion
PPE	Personal protective equipment
PSAB	Plasma surface activated bonder
Pt	Platinum

PDMS	Polydimethylsiloxane
PI	Polyimide
KCl	Potassium chloride
CTX100	Proprietary polymer from Kuraray, Japan
QCM	Quartz Crystal Microbalance
RF	Radio frequency
RIE	Reactive ion etching
rGO	Reduced graphene oxide
RE	Reference electrode
RA	Rolled-annealed
SCE	Saturated calomel electrode
SEM	Scanning electron microscope
STEM	Scanning transmission electron microscope
SPE	Screen-printed electrode
Si	Silicon
SiC	Silicon carbide
SiO_2	Silicon dioxide
AgCl	Silver chloride
SW-CNT	Single-walled carbon nanotube
SW-ASV	Square wave anodic stripping voltammetry
SHE	Standard hydrogen electrode
SAB	Surface activated bonding
SERS	Surface enhanced Raman scattering
SPP	Surface plasmon polariton
TRGO	Thermally reduced graphene oxide
Ti	Titanium
TEM	Transmission electron microscope
UHV	Ultra high vacuum
UV	Ultraviolet
USB	Universal serial bus
H_2O	Water
WE	Working electrode
WHO	World Health Organization
XPS	X-ray photoelectron spectroscope
Zn	Zinc

List of Symbols

E	Cell potential
$[Pb^0]$	Concentration of lead atoms
$[Pb^{2+}]$	Concentration of lead ions
C	Coulomb
I	Current
°C	Degree Celsius
ΔI	Difference between forward and reverse current
e^-	Electron
eV	Electronvolt, approximately equal to 1.6×10^{-19} Joules
F	Faraday's constant, 96,485 $C.mol^{-1}$
I_F	Forward current during anodic stripping voltammetry
Hz	Frequency in Hertz
J	Joule
K	Kelvin
L	Liter
MPa	Megapascal
μA	Microampere
μg/L	Micrograms per liter
μL	Microliter
μm	Micrometer
mA	Milliampere
mg/L	Milligrams per liter
mL	Milliliter
mm	Millimeter
mM	Millimolar
mV	Millivolt
M	Molar
R	Molar gas constant, 8.314 $J.mol^{-1}.K^{-1}$
mol	Mole
ng/L	Nanograms per liter
nm	Nanometer
nM	Nanomolar
Q	Net charge
n	Number of moles of electrons per moles of reactant
Pa	Pascal

N/m	Peel strength in Newton per meter
IR	Reverse current
s	Second
sccm	Standard cubic centimeters per minute (gas flow rate)
E^O	Standard cell potential
T	Temperature in Kelvin
V	Voltage
W	Watts

Declaration of Academic Achievement

This thesis was written by me, Md. Taufique Zaman Redhwan, under the supervision of Dr. Yaser M. Haddara and Dr. Matiar M. R. Howlader from the Department of Electrical and Computer Engineering, McMaster University.

- Chapter 1: I summarized the research motivations and challenges.
- Chapter 2: I conducted the literature review and decided on the key design parameters for the sensor. Description and cleanroom training of characterization tools were provided by Dr. Howlader, Arif Ul Alam, Dr. Yiheng Qin, and Fangfang Zhang.
- Chapter 3: I bonded all the Cu/LCP specimens. Initial training on specimen bonding using PSAB was provided by Fangfang Zhang. Dr. Howlader supervised the Cu/LCP bonding and Dr. Haddara supervised the optimization of bonding parameters. Arif Ul Alam performed the Fourier transform infrared spectroscopy measurements and data analysis. All experiments and data analysis related to peel test, XPS, water contact angle, AFM, and SEM were conducted by me with training support from Arif Ul Alam. Dr. Moon Kim's group performed the HRTEM studies, and data analysis was supervised by Dr. Howlader.
- Chapter 4: I designed and fabricated all the sensors. Dr. Haddara supervised the sensor characterization, sensing parameters optimization, and interference studies. All data analysis was done by me.
- Chapter 5: Dr. Haddara and I identified future extensions of this work.

Chapter 1

Introduction

Tap water lead (Pb) levels well below the established water guideline are now considered harmful, thus detecting sub-parts-per-billion (sub-ppb) level Pb is important. Conventional sensing methods for detecting low levels of Pb are challenging because they are lab-based and require bulky and expensive instrumentation. In contrast, electrochemical sensing of Pb is an attractive analytical technique because they can provide similar parts-per-billion (ppb) detection limit using only a three-electrode setup. However, to realize a truly low-cost and consumer-friendly sensor, these sensing electrodes should ideally be fully-integrated and be based on inexpensive materials.

In this chapter, we introduce the importance and conventional approaches for sensing Pb in drinking water. We discuss about existing and proposed water safety guidelines that define the acceptable levels of Pb concentrations in drinking water. We also identify the challenges of conventional analytical tools and highlight recent developments in Pb sensing tools. Based on these, we identify the motivating factors for this research followed by proposing an all copper-based electrochemical Pb sensor fabricated on polymer substrates. We conclude this chapter by outlining the layout of this thesis.

1.1 Research background

Heavy metals are defined as metals with atomic weights between 63.5 and 200.6 g/mol. These metals are non-biodegradable, so they accumulate in the biosphere and enter living organisms through alimentary chain. Among various heavy metals, lead (Pb), cadmium (Cd), mercury (Hg), arsenic (As) and chromium (Cr) are the most probable causes of heavy metal-related diseases. Some heavy metals are required in trace quantities for biological functioning of living organisms and its presence at higher concentration leads to toxic effects. This is due to the bond formation of these metals with thiol groups of regular protein sites instead of natural binding sites that alters biochemical lifecycle.

1.1.1 Contamination by heavy metal ions and their detection

Table 1-1 lists various sources, permissible limits, health effects, and different sensing materials used to detect heavy metal ions [1]. Surface water gets contaminated due to leaching of heavy metals from the mentioned sources. Unsafe disposal of consumer products and industrial wastes also exacerbate the presence of these ions in water. A brief outline of the different types of material that can detect these heavy metal ions by some sensing mechanism is also included in Table 1-1.

Like other heavy metals, Pb (atomic number 82) occurs naturally in the environment, and it has been historically used in water pipes and plumbing as well as an additive in gasoline and paints. However, Pb is carcinogenic [2][3] and has toxic effects [4] on almost every organ in human body for which its use has been phased out in many applications. Today a major source of Pb is surface water. In underdeveloped countries, unsafe disposal

of lead-acid batteries has led to increased Pb levels in drinking water. In developed countries, the threat is equally severe mainly due to Pb leaching into drinking water from old water pipes and plumbing.

According to the World Health Organization (WHO), the maximum acceptable concentration (MAC) of Pb in drinking water is 0.01 mg/L (10 μg/L). This guideline was last updated in 1992. The Canadian Federal-Provincial-Territorial Committee on Drinking Water (CDW) has recently proposed to update this existing guideline to 5 μg/L (5 ppb). The proposal is based on the observation that low-levels of Pb that were previously considered safe can now cause adverse health effects in humans. Pb intake through drinking water is linked to reduced cognition, increased blood pressure, kidney damage, and renal dysfunction in adults, as well as neuro-degenerative diseases, behavioral disorders, and hyperirritability in children [5][6][7]. The exact safe limit of Pb in water is still unknown, so detecting Pb in the sub-ppb levels is important for ensuring safe drinking water and enabling health studies researches.

Table 1-1. Safe limits, sources, and toxic effects of heavy metal ions on human health. A brief outline of different materials used for the detection of these heavy metals is also presented. Source: [1]

Heavy metal	WHO limit (mg/L)	Sources	Effects	Sensing materials
Lead (Pb)	~~0.05~~ (0.01)	PVC pipes, plumbing accessories, agriculture, recycled PVC lead paints, lead-acid batteries.	May be a risk factor for Alzheimer's disease. Causes neuro-degenerative disease, lower IQ, kidney damage, hyperirritability.	SW- and MW- CNT, Nafion, bismuth, mercury, gold, carbon tape.
Cadmium (Cd)	0.005	Rechargeable batteries, paints, pigments, plastics, synthetic rubber, photoconductors, photovoltaic cells.	Renal toxicity, hypertension, weight loss, fatigue, pulmonary fibrosis, atherosclerosis, lung cancer, peripheral neuropathy.	SW- and MW- CNT, copper, gold nanoparticles, bismuth.
Mercury (Hg)	0.001	Combustion of coal, municipal solid waste, volcanic eruption.	Affects digestive system, immune system, lungs, kidneys, skin and eyes.	rGO, DNA grafted graphene, silver and gold nanoparticles, CNT, zinc oxide nanorods.
Arsenic (Ar)	0.05	Surface water, wooden electricity poles treated with Ar-based preservatives, pesticides, fertilizers.	Affects central and peripheral nervous systems. Causes cardiovascular and pulmonary diseases, skin cancer.	Boron-doped diamond, silver disk electrode with diamond, gold and cobalt oxide nanoparticles.
Chromium (Cr)	0.05	Leather industry, tanning, and chrome plating industries.	Reproductive toxicity, embryotoxicity, mutagenicity, lung cancer, skin ulcers.	Graphene, gold nanoparticles, MW-CNT, carbon composite.
Silver (Ag)	0.1	Refining of copper, gold, nickel, and zinc-based jewelry, electroplating industries.	Neuronal disorders, mental fatigue, rheumatism, cartilage knotting, cytopathological effects in fibroblast.	Self-assembled CNT monolayer, DNA oligonucleotides, glucose oxidase, metallothionein.
Zinc (Zn)	5	Mining ores, soldering, cosmetics, pigments.	Respiratory and neuronal disorders, prostate cancer risk, impotence.	Copper, polyaniline, MW-CNT, carbon paste, Fe_3O_4 nanocrystals.
Copper (Cu)	1.3	Mining ores, minerals, fertilizers, tanning, electric wires.	Arthritis, autism, cystic fibrosis, diabetes, hemorrhaging, kidney disorders, allergies.	Gold nanoparticle, self-assembled nanofibrils, mesoporous silica.

1.1.2 Conventional ways of lead determination in water

1.1.2.1 Spectroscopy

Pb in drinking water has conventionally been detected using spectroscopic analysis in a laboratory environment. These elemental detection techniques include graphite furnace atomic absorption spectrometry (GFAAS) [8], inductively coupled plasma atomic emission spectroscopy (ICP-AES) and inductively coupled plasma mass spectrometry (ICP-MS) [9]. Each of these techniques has a different operation principle but in common, they are all instrumentally intensive.

In GFAAS, the sample containing the analyte is heated and vaporized in a pyrolytic carbon coated graphite tube. This atomizes the analyte which then absorbs light at characteristic frequencies or wavelengths. The analyte concentration can then be determined in ppb levels based on the amount of absorption. ICP-AES on the other hand uses a high temperature (6,000 to 10,000 K) plasma torch to produce an electromagnetic radiation signature of the analyte. The concentration of the analyte is then determined from the intensity of the emission. ICP-MS is a powerful tool [9] that can detect concentrations in the parts-per-quadrillion (ppq) range. To do this, the aqueous sample containing the analyte is nebulized followed by ionization with inductively coupled plasma. The generated ions are then separated and quantified using a mass spectrometer. GFAAS, ICP-AES, and ICP-MS are all expensive, time-consuming, and labor-intensive procedures that require a well-trained analyst [7]. As such they are not always the ideal choice for easy analysis of drinking water samples.

1.1.2.2 Anodic stripping voltammetry

Anodic stripping voltammetry (ASV) is a popular technique to this day for quantitative Pb detection [10]. Specifically, ASV is used together with a three-electrode setup for quantifying the Pb redox reaction in terms of electrical means. This three-electrode setup comprises of a working electrode (WE), a reference electrode (RE), and an auxiliary electrode (AE) [11]. The reaction of interest (deposition and oxidation of Pb) takes place on the WE, thus WEs are made of materials that show good affinity towards Pb and are not too easily oxidized. The RE is usually made of silver/silver chloride, Ag/AgCl, in a glass tube with a saturated inner filling solution (usually concentrated KCl) while the AE is made of an inert material like platinum (Pt) wire or graphite rod. The three-electrode setup is connected to a potentiostat that controls an applied potential and measures the current against it during Pb oxidation. Specifically, Pb^{2+} ions in water is first reduced (deposited) to Pb^{0} atoms on the WE by the application of a deposition potential more negative than the standard reduction potential of Pb. The deposited Pb^{0} atoms are then oxidized back to Pb^{2+} ions as the potential is swept to a more positive value. During this oxidation, 2 electrons per mole of Pb are released which are detected as a current flow between the WE and AE. This redox process is written as:

$$Pb_{(s)} \leftrightharpoons Pb^{2+}_{(aq)} + 2e^{-} \tag{1.1}$$

The detected current peak correlates to the concentration of Pb^{2+} ions in water and is registered at a potential that is characteristic to Pb oxidation. This is governed by the Nernst equation [11]:

$$E = E^0_{Pb^{2+}/Pb} - \frac{0.05916}{2} log \frac{1}{[Pb^{2+}]} \quad (1.2)$$

where E is the potential applied to the working electrode measured versus the reference electrode, $E^0_{Pb^{2+}/Pb}$ is the standard cell potential, which is a function of the standard potential of the reference electrode (relative to a standard hydrogen electrode) and the resistivity of the internal solution, and $[Pb^{2+}]$ is the concentration of Pb^{2+} ions on electrode.

1.1.2.3 Colorimetric sensors

Other ways to determine Pb include the use of fluorescent and colorimetric sensors. These sensors are based on different binding mechanisms of Pb ions to a chemical or biological receptor. The color or fluorescence of these receptors change when they react with Pb. For example, fluorosensors based on fluorescently labeled organic chelators, proteins, or peptides have been used to detect Pb [12]. Based on the type of receptors used, these sensors can be categorized into several groups such as small molecule-based sensors, calixarene-based chemosensors, polymer-based chemosensors, DNA functionalized sensing systems, and nanoparticle-based sensing systems [13]. Colorimetric or fluorescence sensors provide only a qualitative indication of Pb levels thus they do not provide a high measurement accuracy. They can however be used with different matrices such as painted surface, tap water, or blood serum, and can provide ppb detection limits. These sensors are commercially available as multi-parameter water quality test kits and costs anywhere from $9−$399/kit.

1.1.3 Recent trends in Pb determination

1.1.3.1 Anodic stripping voltammetry with integrated microelectrodes

Some of the recently reported electrochemical Pb sensors are miniaturized and have a fully-integrated three-electrode setup. The WE is usually made of an inert material such as gold, silver, platinum, glassy carbon electrodes, boron doped diamond, pyrolytic carbon, and mercury. For the RE, Ag/AgCl and saturated calomel electrodes (SCE) remain the popular options. Most commonly used AEs today are the ones made from gold, platinum, and graphite. Currently an increased effort on miniaturizing and integrating the WE, RE, and the AE to a common planar substrate have been noticed. Exploring the use of different material combinations towards fabricating integrated microelectrodes has a common goal of miniaturization, achieving ppb limit of detection (LOD), lab-on-chip integration, and bringing down fabrication cost and complexity without compromising the sensor performance. A more detailed literature review of integrated electrochemical Pb sensors is provided in Chapter 2.

1.1.3.2 DNA functionalized biosensors

Pb detection has been demonstrated previously using a DNAzyme-functionalized electrochemical biosensor [14]. More recently, a similar DNAzyme-functionalized mechanical biosensor has been reported [15]. This mechanically transduced sensor is facilitated by a DNAzyme-based quartz crystal microbalance (QCM) and functionalized gold nanoparticles (AuNPs) on the sensor surface. When Pb^{2+}−specific DNAzymes are first immobilized onto the QCM sensor surface, the DNAzymes hybridize with the substrate-

functionalized AuNPs. In the presence of Pb^{2+}, these DNAzymes catalyze the substrate and removes the AuNPs from the sensor. This removal is then detected by piezoelectric principles. The DNAzyme-based QCM biosensor has 14–20 nM Pb detection limits.

1.1.3.3 CHEMFET sensors

CHEMFET sensors have a chemically-modified field-effect-transistor (FET) electrode configuration [16]. Recently, a pulse-driven chemo-capacitance-based transduction method for Pb sensing has been demonstrated [17]. The FET-based structure is fabricated from a thermally reduced graphene oxide (rGO) channel. The top gate is passivated with a thin layer of aluminum oxide (Al_2O_3) combined with sputtered AuNPs. These AuNPs link with a chemical probe called glutathione (GSH) to attract Pb^{2+} ions in water. A microcontroller generates square-wave control pulses, whose shape and related time constants get modified in the presence of Pb^{2+} ions. This sensor takes only 1−2 seconds to detect Pb and has <1 ppb LOD.

1.1.3.4 Surface plasmon polariton-based sensors

Optical transduction, specifically a surface plasmon-polariton (SPP) based functionalized surface-enhanced Raman scattering (SERS) platform has recently been demonstrated for Pb detection [18]. This sensor needs to be connected to a Raman spectrophotometer and is based on a periodical gold grating. This grafting is created by the excimer laser patterning of polymer surface followed by vacuum sputtered gold deposition. For efficient Pb^{2+} trapping, the gold surface is then functionalized with 4-aminopheylene layers and diethylenetriaminepentaacetic acid (DTPA). DTPA has a high affinity to Pb^{2+}

ions and thus show a high SERS response in the presence of Pb^{2+} ions due to SPP excitation and propagation on the gold grafting. The sensor can detect 10^{-9} parts-per-million Pb^{2+} ions.

1.2 Research motivation

Among the numerous research activities (Section 1.1.3) carried out for quantitative detection of Pb, very few of them has successfully made it to the market. Electrochemical sensors can easily detect very low concentration of analyte and offer the choice of a wide range of electrode materials and fabrication process [19][20][21]. Therefore, this research is aimed at developing an integrated electrochemical Pb sensor [22] that can be easily commercialized with the following target features:

- Sensor should be miniaturized and integrated to a common substrate. This will allow future integration to external microfluidic systems.
- Sensor electrode material should be cost-effective, without compromising performance.
- Sensor should provide parts-per-billion limits of detection.
- Sensing protocol should be simple and response time should be reduced.
- Sensor should require only a few microliters (μL) sample volume.
- Sensor fabrication should be production-friendly, simple, and low-cost.
- Sensor should provide a stable response during the course of measurement.
- Sensor integration should be reliable, and electrodes should be not easily consumed or delaminated during fabrication or sensing.

In recent years, considerable work has been done on electrochemical sensors for Pb detection [23]. A wide range of materials including graphene [24][25], Nafion-based composites [26][27], sol-gel silica [28][29], mercury [30], bismuth [31][32][33][34], bismuth/copper [35], copper [36], bimetallic mercury-bismuth with carbon nanotubes (CNTs) [37], CNT-composites [38], boron-doped diamond (BDD) [39][40][41][42][43], gold [44], platinum [45], and silver/carbon [46] have been used for electrodes in Pb sensors. Most of these sensors are miniaturized and can detect parts-per-billion level Pb, but there are limitations and drawbacks. First, these disposable sensors are not always ideal due to high material cost. Second, most sensors are limited by expensive and time-consuming fabrication procedures like e-beam evaporation, vacuum sputtering, or in situ plating followed by multi-step photolithography. These processes typically result in a thin layer (<1 μm) of sensing electrodes. Thin-film electrodes can get consumed during sensing in acidic electrolyte or delaminate from the substrate due to insufficient adhesion [33][45][47][48]. Substrate adhesion can be improved by depositing a metallic underlayer of titanium (Ti) [48], but this also increases process complexity and cost. Third, these electrochemical sensors usually take about 2−15 minutes to detect Pb, but faster sensing can be achieved.

The motivation of this research is to address these challenges. This thesis reports on an integrated (Cu)-foil-based electrochemical sensor that can detect trace Pb ions in water. Cu has high conductivity, shows good affinity towards Pb [36], is cheaper than Au or Pt, and is compatible with different fabrication approaches. Cu can be rolled-annealed (RA) or electrodeposited, both of which yield thick-foil (>10 μm) electrodes. Thin-film (<1 μm) Cu

electrodes are usually vacuum sputtered from a 99.99% pure Cu target. In this work, we use thick RA Cu-foil electrodes over thin-films because the bulk of RA Cu has a compact grain structure [49] and a larger cross-sectional area that lowers sheet resistance. These bulk features promote good signal integrity [50][51] and facilitate the flow of small (few nanoamperes) electrolytic cell current during trace Pb detection. Thicker electrodes also provide sacrificial Cu oxidation layers for extended operation in acidic electrolyte [47][36], so the electrodes are not readily consumed or degraded. However, these benefits of RA Cu electrode are sometimes offset by the fact that they are difficult to bond to the substrate due to poor adhesion property caused by lack of mechanical interlocks [52]. A strong bonding is necessary to reduce etchant-caused Cu foil under-cuts during fabrication, to prevent electrode delamination, and to ensure electrode performance that often depends on surface/interface adhesion [48][53].

These integration issues were previously addressed by our group using argon radio frequency plasma (Ar-RF) activation of Cu and LCP [54][55]. However, these processes required intense process parameters such as high activation power (~700 W), high irradiation time (~ 30 min), and high contact pressure (~ 800 MPa). Furthermore, the Ar-plasma-based bonding required deposition of a metallic underlayer of Cu on LCP prior to bonding. Therefore, one of the motivations of this thesis is to significantly simplify the integration of Cu/LCP. For this, we successfully develop a low-temperature, low-pressure, surface-activated bonding (SAB) process [47][56] based on O_2-RIE plasma treatment of Cu and LCP. Our bonded specimen is flexible and can be fed directly into an inexpensive LaserJet printer for a one-step-transfer of polyester resin-based electrode mask. This

eliminates the need for several photolithographic mask processing steps, thus significantly reducing fabrication complexity and time in addition to offering a low-cost path to mass scale sensor production.

To summarize, this research focuses on the development of a fully-integrated electrochemical sensor for Pb detection with the proposed design specifications as listed in Table 1-2.

Table 1-2. Proposed specifications for lead sensor.

Parameters	Value
Electrode material	Directly-bonded rolled-annealed Cu on polymer
Sensing range	0.2 – 2000 ppb (or 0.2 – 2000 μg/L) Pb^{2+}
Response time	< 1 min
Sensitivity	0.1 – 0.3 μA/μM
Sample volume	100 μL injection into a sealed PDMS well
Drift in potential response	< 5 mV
Drift in current response	< 15 nA
Dimensions	17 × 20 mm^2
Material cost	< 50¢/sensor
Electrode type	> 1 μm (thick-film)
Stability	At least up to 20 sensing cycles
Storage condition	Dry
Maintenance required?	No (disposable)
Fully-integrated?	Yes

1.3 Research contributions

The major contribution of this work can be broadly categorized into two aspects. The first aspect focuses on the materials integration (Cu and polymer) using a direct bonding process. The second aspect of this research demonstrates a simple and low-cost fabrication process towards fabricating electrochemical sensors on mechanically flexible Cu/polymer. These contributions are summarized as follows:

1) **Direct bonding of Cu foil and polymer.** An oxygen reactive-ion-etching (O_2-RIE) plasma-based bonding process is developed for integrating 50 μm-thick Cu foil to 50 μm-thick liquid crystal polymer substrates. Similar direct bonding processes are used to integrate heterogeneous materials without the use of chemical adhesives. For Cu/LCP integration, the bonding parameters are optimized to obtain a good peel strength. The directly bonded interface is characterized through investigation of chemical composition, cross-sectional electron microscopy, film morphology, and surface roughness. These findings are used to describe the fundamentals of Cu/LCP bonding.
2) **LaserJet printing of electrode mask.** The mechanical flexibility of directly-bonded Cu/LCP is utilized for a one-step electrode mask print-and-transfer process. In contrast to photolithographic processing, the LaserJet printing eliminates the need for spin-coating of a photoresist, does not require separate mask development or UV exposure tools, and does not require a developer solution or oven-bake to harden the photoresist. The LaserJet printing directly prints a polyester resin-based electrode mask on the Cu side of Cu/LCP. The toner then serves as the resist during wet etching of Cu electrodes.

3) **Development of Cu-based sensor for Pb detection.** Cu-foil based electrochemical Pb sensors are finally developed on directly bonded Cu/LCP as well as on commercially available Cu/polyimide (PI) laminate, and their sensor performances are compared. Anodic stripping voltammetry is used to quantify different concentrations of Pb. The lowest experimentally-achieved detection limit for both types of sensors is 0.2 μg/L (0.2 ppb) Pb which is lower than the proposed safety regulation guideline of 5 μg/L. The sensors require only a 100 μL sample and 30 s for analysis. Interference effects of cadmium (Cd) and zinc (Zn) on the sensor performance are also studied.

Publications:

1) Redhwan, T. Z., Alam, A. U., Catalano, M., Wang, L., Kim, M. J., Haddara, Y. M., & Howlader, M. M. (2018). Direct bonding of copper and liquid crystal polymer. *Materials Letters*, *212*, 214-217.
2) Redhwan, T. Z., Alam, A. U., Haddara, Y. M., & Howlader, M. M. (2018). Copper and liquid crystal polymer bonding towards lead sensing. *Japanese Journal of Applied Physics*, *57*(2S1), 02BB03.
3) Redhwan, T. Z., Alam, A. U., Qin, Y., Howlader, M. M., & Haddara, Y. M. (2018). Fully-integrated sensor based on surface activated Copper/polymer bonding for sub-parts-per-billion-level lead detection. *ACS Sensors (under review).*

1.4 Thesis organization

In Chapter 1, an introduction to the significance of Pb sensors for water quality monitoring is presented. Conventional approaches and recent trends in Pb determination techniques are briefly discussed. This is followed by identifying the motivations and challenges of developing an accurate, easy-to-use, and low-cost electrochemical Pb sensor. Finally, the contributions of this research and the thesis layout are presented.

In Chapter 2, a detailed review of electrochemical sensing technique and developed electrochemical Pb sensors are presented. This review helps identify several design considerations for our sensor. The different approaches for surface-activated bonding are reviewed. This chapter concludes with a brief outline of different fabrication and characterization tools used in this research.

In Chapter 3, we describe the materials and reagents used for sensor fabrication. We describe the SAB process for integrating Cu and LCP, followed by outlining the sensor fabrication procedure. We discuss on the process parameter optimization of SAB to obtain adequate electrode−substrate adhesion. Finally, we characterize the directly-bonded Cu/LCP and describe the fundamentals of bonding mechanism.

In Chapter 4, we discuss on the feasibility of fabricated sensors towards quantitative detection of ppb level Pb^{2+} ions in water. This is followed by an outline of the reagents, sample preparation, and experimental setup. We report on the optimization of sensing process parameters towards obtaining fast sensing response and good sensitivity. The sensing performance of directly bonded Cu/LCP-based sensors are then compared with that

of commercial Cu laminate-based sensors, together with a study of interference effects on the Pb sensor caused by Cd and Zn ions.

Finally, we conclude this thesis in Chapter 5 with indications of future research. The fundamentals of Cu/LCP bonding may enable integration of novel material combinations by SAB, while the directly bonded Cu/LCP can be utilized for fabrication of other types of flexible sensors.

Chapter 2

Theory, review, and experimental methods

Electrochemical Pb sensors are based on an analytical technique known as voltammetry that uses a measurement of potential and current to determine Pb^{2+} concentrations in an aqueous solution. This area of analytical chemistry is termed *electrochemistry* because it studies the movement of electrons in an oxidation-reduction reaction. In this chapter, we present four main principles of electrochemistry that forms the basis of electrochemical Pb sensing. Next, we present a review of different Pb sensors that operate based on these principles.

We also review surface-activated bonding techniques that can provide effective integration of electrodes to the sensor substrate without using chemical adhesives. Based on these SAB approaches, we develop the direct bonding process of Cu/polymer specimens that are used to fabricate Pb sensors in this work. This bonding is integral to the sensor performance and ensures that the sensing electrodes do not delaminate during wet etching. Finally, brief outlines of the fabrication and characterization tools are provided.

2.1 Basis of electrochemical sensing

Electrochemical technique is commonly divided into bulk technique or interfacial technique. In bulk technique, we measure a property of the solution (such as conductivity in the presence of dissolved ions) in the electrochemical cell. In an interfacial technique such as the one used in this work, the potential, charge, or current depends on the species present at the electrode−solution interface. Other than Pb sensing, determination of pH using a pH electrode is an example of an interfacial electrochemical technique.

Electrochemical sensing of Pb is based on four main interrelated principles of electrochemistry: (1) the electrode's potential determines the oxidation state of analyte; (2) interfacial concentration may not equal bulk concentration; (3) current is a measure of the rate of reaction; and (4) current and potential in an electrochemical cell cannot be simultaneously controlled. A discussion of these principles requires the introduction of Nernst equation that provides a mathematical relationship between the sensing electrode potential, E, and net charge transfer, Q, due to oxidation or reduction of one mole Pb:

$$Pb^{0}_{(s)} \leftrightharpoons Pb^{2+}_{(aq)} + 2e^{-} \tag{2.1}$$

$$E = E^{O} - \frac{RT}{nF}\log Q \tag{2.2}$$

(E^{O} is the standard-state reduction potential for Pb; R is the molar gas constant, 8.314 J.mol^{-1}.K^{-1}; T is the temperature in K and assumed 25 °C (298 K); n is the number of moles of electrons per moles of reactant; and F is the Faraday's constant, 96,485 C.mol^{-1}).

2.1.1 Electrode potential determines the oxidation state

For a redox reaction, the electrode potential determines the reaction's equilibrium position [11]. Fig. 2-1 shows a ladder diagram for the Pb^{2+}/Pb^{0} equilibria. If an electrode is placed in a solution containing Pb^{2+} ions and adjust its potential, E, to −0.500 V, Pb^{2+} ions are reduced to Pb^{0} atoms that deposit on the electrode surface. Alternatively, if the electrode potential is set to 0.000 V, Pb^{2+} remains unchanged and the electrode sees the bulk concentration of the solution on its surface. The standard-state reduction potential of Pb redox couple is −0.126 V against a standard hydrogen electrode, which signifies that an electrode potential more positive than −0.126 V will favor the oxidized form of Pb redox pair, whereas the reduced forms are the predominate species at a potential more negative than E^{0}:

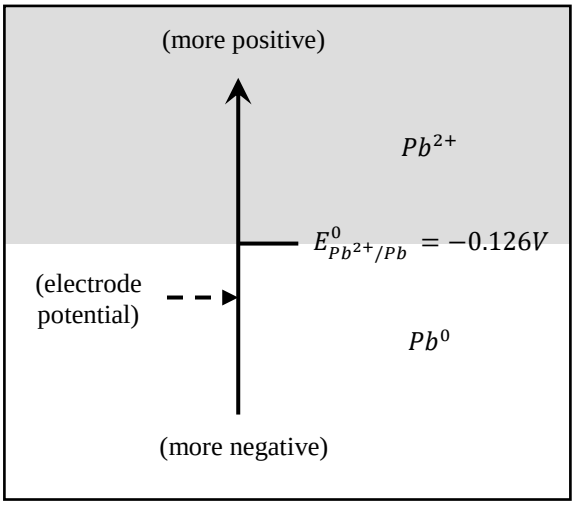

Figure 2-1. Redox ladder diagram for Pb redox couple. At electrode potentials more negative than E^{0}, Pb^{0} deposits on electrode. At more positive potential, Pb^{2+} dominates.

This behavior can also be explained by the Nernst equation in its rearranged form:

$$E - E^{O} = \frac{RT}{nF} \ln \frac{[Pb^{2+}]}{[Pb^{0}]} \tag{2.2}$$

For $E^0 = -0.126$ V and when $E = -0.500$ V, the left side of equation 2.2 is negative. To balance the right side of the equation, $[Pb^0]$ must exceed $[Pb^{2+}]$. Similarly, $[Pb^{2+}]$ must be greater than $[Pb^0]$ when E is more positive than E^0.

2.1.2 Interfacial concentration and bulk concentration

Since the potential of the electrode determines the form of Pb at the electrode's surface, the concentration terms in Nernst equation are those at the electrode's surface, not the concentrations in bulk solution. Therefore, when an electrode is placed in a solution containing Pb^{2+} and E is made more positive than E^0, the concentration of Pb^{2+} on the electrode surface remains unchanged (same as bulk concentration) at any distance away from the electrode surface (Fig. 2-2a). At values of E more negative than E^0, the concentration of Pb^{2+} very close to the electrode's surface decreases to approximately zero (Fig. 2-2b). This is because Pb^0 atoms are then the dominant species that forms on the electrode surface. However, the concentration of Pb^{2+} increases linearly as we move away from the electrode's surface until the point where it equals the bulk concentration. Therefore, the deposition (reduction) of Pb^{2+} ions from solution to Pb^0 atoms on the electrode surface is a diffusion-controlled process and interfacial concentration may not equal bulk concentration [11].

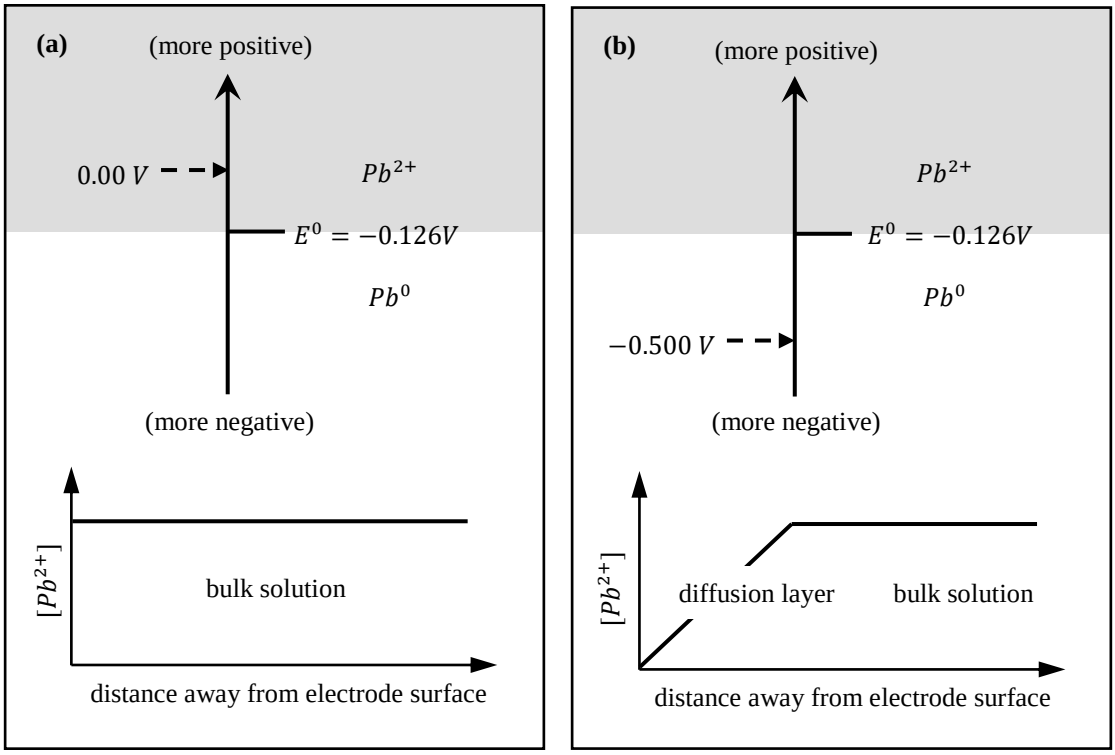

Figure 2-2. Concentration of [Pb^{2+}] as a function of distance from the electrode surface at: (a) E more positive than E^0, and (b) E more negative than E^0.

2.1.3 Current is a measure of rate of reaction

The rate of a reaction, such as the reduction of Pb^{2+} to Pb^0 is defined as the change in concentration of Pb^{2+} as a function of time. This reduction process consumes 2 electrons per mole of Pb that are drawn from an electrode serving as the electron source. During oxidation, Pb^0 atoms release 2 electrons per mole to become Pb^{2+}, and these electrons are taken by an electrode serving as the electrode sink. In both the cases, the flow of electrons between two electrodes (WE and AE, discussed later in Section 2.1.5) provides a measurable *Faradaic* current which is a measure of the rate of respective reactions.

2.1.4 Simultaneous control of current and potential

Considering the two-electrode operation as described in Section 2.1.3, the Faradaic current is zero for a Pb redox reaction at equilibrium. At this instance, if one of the electrode potentials is changed, there will be a current flow until the equilibrium oxidation state of Pb is reached. This causes a current change in response to the applied potential. Alternatively, a fixed current can be passed through the two electrodes, but this forces a reduction reaction which is offset by a change in electrode surface potential. Thus, with a two-electrode setup, if we choose to control the electrode potential then we must accept a current drift, and we must accept a drift in electrode potential if we choose to control the current. This is a crucial observation that leads to the consideration of a three-electrode electrochemical Pb sensor design.

2.1.5 Three-electrode sensor and voltammetry

2.1.5.1 Three-electrode setup

Voltammetry is an analytical method that is based on the discussed principles of electrochemistry. This method investigates the half-cell[1] reactivity of an analyte such as Pb. It is the study of current, I, as a function of applied potential, E. The potential is varied arbitrarily both step by step or continuously, and the current value is measured as the dependent variable. The curve of $I = f(E)$ is called a voltammogram, and it is the

[1] A half-cell is one of the two electrodes in a galvanic cell or simple battery. Placing a piece of reactant in an electrolyte solution makes a half-cell. Unless it is connected to another half-cell via an electric conductor and salt bridge, no reaction will take place in a half-cell.

electrochemical equivalent of a spectrum in spectroscopy [57]. A voltammogram provides quantitative and qualitative information about Pb oxidation or reduction, and its shape depends on the nature of potential variation (frequency, type, amplitude etc.) and on whether the solution is stirred or quiescent [11]. Voltammetry requires at least two-electrodes, a WE and an AE. However, as discussed in Section 2.1.4, simultaneous control of potential and current is difficult with a two-electrode setup. For this reason, the roles of supplying electrons while maintaining a stable reference potential are divided between two separate electrodes, namely AE and RE, respectively.

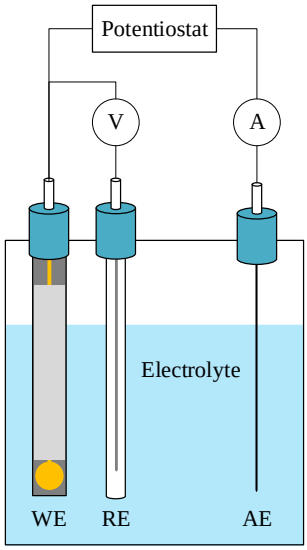

Figure 2-3. Schematic illustration of a three-electrode setup using commercial electrodes.

The oxidation or reduction of Pb occurs on the WE, so it must apply the potential variation in a controlled way and facilitate the transfer of charge to and from the analyte. The AE sustains the Faradaic current during this charge transfer by completing the circuit.

A third-electrode, namely the RE, only acts as a reference in measuring and controlling the working electrode's potential. As such, no significant current passes between WE and RE at any point. This solves the problem of simultaneous control of potential and current. The schematic of a three-electrode setup is illustrated in Fig. 2-3. The sensor developed in this work is a miniaturized form of this setup on a flexible, planar substrate.

2.1.5.2 Square-wave anodic stripping voltammetry

Square wave anodic stripping voltammetry (SW-ASV) uses a square-wave for anodic stripping voltammetry (ASV) of Pb. SW-ASV is distinct from other voltammetric techniques in terms of the signal that is applied to the WE. A symmetrical square wave is superimposed on a staircase waveform where the forward pulse of the square wave is coincident with the staircase step. The current is sampled twice during each square wave cycle, one at the end of the forward pulse, I_F, and again at the end of the reverse pulse, I_R. This technique discriminates against charging current by delaying the current measurement to the end of the pulse. The difference in current, ΔI, between the two measurements is plotted versus the potential staircase. SW-ASV can perform an experiment much faster than normal and differential pulse techniques, which typically run at scan rates of 1 to 10 mV/s. SW-ASV employs scan rates of up to 1 V/s or faster, allowing much faster determinations. A typical experiment requiring 3 minutes by normal or differential pulse techniques can be performed in seconds by SW-ASV [11].

In SW-ASV, Pb^{2+} is first electroplated (reduced to Pb^0) on the WE by application of a deposition potential. This is followed by a brief rest period to allow the deposited Pb

atoms to settle on the electrode surface. The deposited Pb atoms are then oxidized (stripped) back to Pb^{2+} ions. The stripping current is measured against the peak's potential that is characteristic to Pb oxidation. A calibration curve of stripping current peaks versus known Pb concentrations is then constructed. This entire protocol is programmed in an analog front-end potentiostat that connects directly to the sensor. A visual representation of SW-ASV protocol is given in Fig. 2-4.

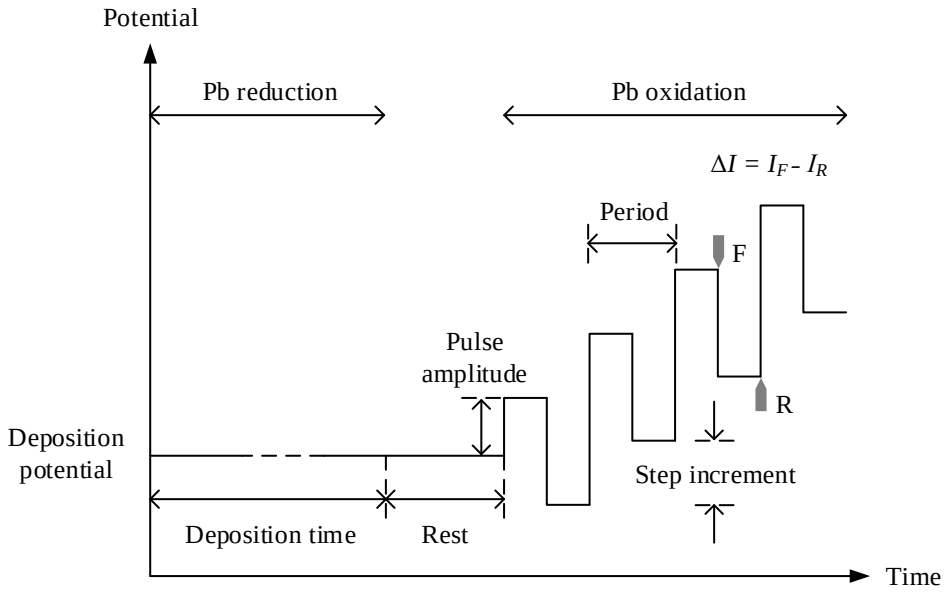

Figure 2-4. Square wave anodic stripping voltammetry protocol.

2.2 Review of electrochemical Pb sensors

In recent years, several microfabricated electrochemical Pb sensors have been reported in the literature. These sensors have a three-electrode configuration as described in Section 2.1.5.1. The sensors have unique miniaturized footprints, different substrate and electrode material combinations, and employ different types of voltammetry for sensing Pb (SW-ASV is most commonly reported). Different materials have different fabrication process compatibilities and thus some sensors are fabricated in a more complicated way than the others. The most commonly used techniques include vacuum sputtering, electrodeposition, and screen-printing [58] followed by photolithographic micro-patterning and wet etching of the electrodes. In some works, the use of a metallic adhesive underlayer is also observed. This review section has been grouped based on important findings that are used as design considerations of the Pb sensor.

2.2.1 Use of nanostructures

Xuan (2016) [24] reported a reduced-graphene-oxide on gold (TRGO/Au)-based working electrode to detect 0.4 μg/L lead and 1.0 μg/L cadmium in water. Bismuth was electrodeposited on TRGO/Au to enhance the Pb/Cd stripping characteristics of the sensor [24]. They used SW-ASV technique together with a sputtered Au CE and a screen-printed Ag/AgCl RE on a silicon wafer substrate. Their results show that TRGO/Au-based WE can provide stronger current response than Au-WE during cyclic voltammetry (CV) analysis. TRGOs have unique nanostructures [59]. Incorporation of such nanostructures [35][60][61] and nanoparticles [62] on WEs are usually done to increase the effective electrode-surface-

area [62] that compensates for the miniaturized electrode footprints. For example, hexagon-shaped bismuth nano- and micro-structures [35] electrodeposited onto polycrystalline copper electrodes have been used to detect ultra-trace levels of Pb (0.05 ppb). A more commonly used material is carbon nanotubes (CNTs) [60][61]. Hwang (2008) [61] studied the sensitivities of different carbon materials including CNTs, activated carbon, glassy carbon, and graphite. Their results show that bismuth coated CNTs produce about 3−10 times stronger stripping peak currents in the investigated series. This is because CNTs have three-dimensional hair-like networks that provides a much larger electrode surface area than the apparent geometric area. An increased surface area results in the enhancement of the capacitance at the CNT electrode which provides stronger signals. An increased surface area provides more binding sites for Pb atoms on the electrode surface, thus increasing sensor sensitivity and lowering detection limits.

Urbanová (2010) [63] developed another technique to increase the surface area of the WE. They reported a colloidal template-based approach to fabricate porous structures on thick-films (~12 μm). Their technique increases the effective surface area of the electrode by introducing spherical nanopores in the bulk and on the surface of the thick-film WE. Thick film electrodes provide more nanopores compared to thin film electrodes. However, such spherical nanopores may not always produce repeatable results from multi-use experiments. This is because the reduced Pb atoms that explore the deeper layers of the porous structure may not be completely stripped away from the electrode during ASV oxidation cycle. An alternate approach could be the fabrication of high aspect ratio nanopillars that utilize the depth of thick films.

2.2.2 Use of nanocomposites

Wang (2014) [59] reported a Pb sensor where bismuth was in situ deposited on a graphene/ionic liquid composite modified screen-printed electrode. In contrast to other works based on directly used screen-printed electrodes (SPEs), their work is unique because of a pre-modification to the SPEs with an ionic liquid (*n*-octylpyridinum hexafluorophosphate). By doing so, they produced a conductive composite of the ionic liquid and graphene oxide, which was then used as the WE. For electrochemical detection, SW-ASV was used along with a commercial Ag/AgCl and Pt wire for RE and CE respectively. Although not fully-integrated, this sensor exhibited detection limits of 0.10 μg/L lead and 0.08 μg/L cadmium in rice samples.

Another work reported by Ouyang (2011) [64] demonstrates yet another potential of nanocomposite modification of WEs. They modified a glassy carbon electrode (GCE) by adding bimetallic mercury-bismuth and single-walled carbon nanotubes (SW-CNTs)-based composite. This composite working electrode was used in conjunction with a commercial Ag/AgCl RE and Pt wire CE to detect 0.12 ng/L Pb. A similar work based on RGO/Bi nanocomposite electrode could detect 0.55 μg/L Pb [65]. A possible reason for such low detection limits of Hg-Bi/SWCNT WE could be two-folds. First, CNTs increase the effective surface area of the electrode (Section 2.2.1). Also, CNTs have high conductivity which improves the electron transfer kinetics during Pb oxidation and reduction on the WE. Finally, the sensor performance may be superior due to the co-deposition of mercury and bismuth films, both of which have excellent stripping characteristics. The Hg-Bi/SWCNT nanocomposite, however, tends to easily come off the

GCE [64]. Therefore, a sensor's performance is not only determined by its low detection limit but is also complemented by its reliable integration. Improving the substrate adhesion of thick foil-based electrodes is in fact one of the focus areas of this thesis.

2.2.3 Thick film electrodes

One advantage of thick film electrode [63] has been mentioned in Section 2.2.1. Wang (2001) [66] identified more benefits of thick-film electrodes. Specifically, they fabricated a Pb sensor based on thick-film electrodes and applied SW-ASV to demonstrate a low detection limit of 0.3 ppb Pb in water. This sensor used a bismuth-coated screen-printed carbon electrode for the WE, an Ag/AgCl RE, and a Pt wire for CE. One of the major observations in this work recognizes that short deposition times (~30 s) may be enough to obtain favorable stripping peak signals with thick-film electrodes. Therefore, thick film electrodes may be a viable alternative to thin film electrodes if a faster sensor response is desired. Thick film electrodes can provide longer potential stability compared to thin-film electrodes [67]. One can also access the bulk property of a material (e.g. conductivity) using thick-film electrodes. When used for sensing in acidic electrolyte or harsh environment, thick-film electrodes can also provide additional sacrificial layers so that the electrodes are not easily consumed by oxidation or during stripping of the analyte.

2.2.4 Electrode size and layout

The surface morphology of an electrode plays an important role in electrochemical detection of Pb, but so does the electrode film quality, electrode areas, and the three-

electrode layout [45][68][69]. Lin (2017) [45] reported that sensors with smaller electrode gaps have shorter response time but has a noisy response when detecting low concentrations of Pb. This observation was confirmed by Jothimuthu (2011) [68]. They reported a Pb sensor based on a bismuth WE, an integrated Ag/AgCl RE, and an Au AE – all of which were fabricated using a combination of metal seed layers (Ti/Au) evaporation, electrodeposition, and soft photolithography. They investigated the effect of hydrogen gas bubbles that are generated due to the hydrolysis of water by $H_2O + e^- \leftrightharpoons H_2\,(g) + OH^-$. Hydrogen gas bubbles disrupt the flow of electrons between the AE and the WE, causing high resistance of the solution and loss of potential control of the WE. This also results in broadening of the sensing peak and delamination of the electrodes from the substrate due to adhesion loss or flaking [68]. The authors addressed this problem by placing the AE further away from the WE and by increasing the AE surface area. They argued that an increased distance between the AE and WE causes the bubbles to traverse longer distance to affect the WE, thus reducing interference effects. An increase in AE area while still maintaining the WE area means that under same quantity of gas production, the AE experiences less concentrated gas bubbles, and hence the sensor goes through reduced hydrolysis effect.

2.2.5 Adding convection effects to microsensors

In a conventional non-integrated three-electrode setup, the solution containing the analyte is usually stirred in a beaker with a magnetic stir bar when electrochemical sensing is performed. This introduces convection in the electrochemical cell that brings quicker

deposition, higher sensitivity, and lower detection limits [70]. With an integrated microelectrode setup, the sample injection chamber is usually small (dimensions may vary from a few millimeters up to a centimeter) and a magnetic stir bar cannot be used. Recently, similar convection effect has been introduced by attaching a micro-sized vibrator to an on-chip Pb sensor [70]. With the micro-vibrator turned on, the stripping peak current was almost 3−4 times higher than that obtained for same Pb concentration with the micro-vibrator disabled. Alternatively, the use of a micro-vibrator can reduce the deposition time, thereby providing faster microsensor response.

2.2.6 Microelectrode arrays

A comprehensive overview of the fabrication and operation principles of nanoscale electrochemical sensor arrays was presented by Wolfrum (2016) [71]. They identified important design considerations of nanoarray-based electrochemical sensors. Similar nanocavity crossbar array-based sensing mechanism was reported by Kätelhön (2014) [72]. Wan (2014) [73] reported a hybrid Pb sensor based on gold microelectrode array on a silicon substrate. Kokkinos (2012) [74] fabricated a fully-integrated bismuth microdisk WE array on a silicon wafer for Pb detection. They also developed similar integrated Pb sensor using antimony film WE, Ag RE, and Pt AE [75].

2.2.7 Low-cost electrodes

Feng (2013) [76] reported a low-cost Pb sensor based on bismuth modified inexpensive carbon tape WE, integrated Ag/AgCl RE, and Pt wire AE. The double-sided

adhesive layer of the carbon tape allowed easy integration of electrodes (top) and an indium tin oxide (ITO) substrate (bottom). This sensor was integrated with paper-based analytical devices to detect Pb from only a 15 μL sample. The only limitation of this Pb sensor was its relatively high detection limit (2 μg/L) compared to other works reported in this review. This is because carbon tape is not highly conductive even after conductivity enhancement by the ITO substrate. However, considering the fabrication process simplicity and low material-cost (US$ 0.05/sensor), this sensor appears to be a good candidate for applications where sub-ppb level Pb detection is not required.

Jung (2011) [77] developed a silver/polymer-based sensor with integrated microfluidic channel. They used Ti adhesive layer to integrate Ag electrodes on a polymer substrate using a combination of e-beam metal evaporation, photolithography, electroplating, plastic injection molding, and thermoplastic fusion bonding. The increased complexity, time, and cost incurred for fabricating the sensor appear to offset the reasonable material costs of polymer and silver. This work, however, shows prospect of polymer substrates in fabricating low-cost Pb sensors if a simple fabrication process is developed.

Another low-cost (US$ 0.10) sensor based on all-platinum-tip electrodes has been reported [45]. Although Pt is expensive, the micro-size electrode tip (~1 mm^3) accommodated to this low-cost sensor. This work focused entirely on investigating the qualitative, long-term response of the sensor without quantifying Pb concentration, so the performance or detection limit of this sensor cannot be reported.

2.2.8 Copper as sensing electrodes

We conclude this review with a discussion on the potential of copper-based electrodes in fabricating disposable Pb sensors. Sensing electrodes, especially working and auxiliary electrodes, are made of inert materials to prevent electrode oxidation or potential drifts. Copper is prone to oxidation in air or water, but it also offers significant advantages that trades-off its non-inert nature and makes it suitable for use in a disposable sensor. These benefits include high conductivity, low-cost, affinity towards Pb [36], and compatibility with several fabrication processes like vacuum sputtering, electrodeposition, or roll-annealing. Only a few Cu-based sensors have been identified in the literature. These include the work of Rajamani (2014) [35] who developed nano- and micro-hexagonal bismuth structures on a polycrystalline Cu-based WE. Kang (2017) [36] reported a similar Cu-based Pb sensor based on physically sputtered thin film electrodes. They identified that thin film (~200 nm) Cu electrodes are stable long enough for at least one measurement. This sensor required ~5 min to detect Pb in water and exhibited a detection limit of 4.4 ppb Pb.

2.3 Surface activated bonding (SAB)

2.3.1 Significance of SAB

Throughout the review of electrochemical Pb sensors (Section 2.2), several fabrication approaches have been noticed. Sensing electrodes that have been electrodeposited or physically sputtered to a substrate often require the use of a metallic underlayer (typically titanium or chromium). This underlayer enhances the adhesion between the electrodes and the substrates, but also increases process complexity and

fabrication cost. Some electrodes were also fabricated by a screen-printing process. Screen printed electrodes offer simple fabrication, low-cost, and mass production. However, in most cases, the printing inks for preparing SPEs contain some nonconductive binders or insulating polymers to improve substrate adhesion. For example, certain amounts of polymer composition in the carbon-based composite inks may shield the electrochemically active carbon particles and increase the electron transfer resistance [78] between WE and AE. This slows down the kinetics of heterogeneous reaction responsible for sensing the analyte, and thus adversely affect the sensor performance. Also, like most thin-film and composite electrodes, SPEs can degrade or delaminate from the substrate when exposed to harsh sensing environments. In fact, several works have reported these issues of electrodes being consumed or delaminated from the substrate [33][36][45][47][48][53][64][68].

The integration of various sensing components on the same planar substrate has been identified as a key challenge in packaging, especially for miniaturized, low-cost, and high-sensitivity sensors [79]. For these applications, direct bonding is a particularly attractive option because it enhances the overall system's performance. Current bonding and packaging technologies like thermocompression bonding, fusion bonding, or adhesive bonding are not suitable for sensors due to the needs of high pressure, high temperatures, or chemical solvents that may degrade the electrode performance or cause deformation of flexible organic substrates like polymer [23][79]. Current bonding techniques also do not provide high bond strength, high electrical conductivity, void-free sealing, or sub-micrometer alignment accuracy [79]. For developing Cu/polymer-based sensor, a void-free,

strong bonding is required in this work to prevent under-etching of sensor electrodes during fabrication and to ensure sensor integrity during sensing operation.

2.3.2 Different approaches of SAB

Surface activated bonding (SAB) [79] is a promising low-cost integration technology for similar or dissimilar materials without using high temperature or high pressure. Fig. 2-5 shows 4 different SAB approaches: a) direct bonding in ultrahigh vacuum (UHV), b) nano-layers adhesion in UHV and HV, c) sequential plasma activation in air, and d) hybrid adhesion in air (sequential plasma activation + electrostatic) [79]. The plasma treatment is a physical ion bombardment process that removes adsorbed contaminants and native oxides on the surfaces. The activated surfaces are atomically clean and reactive for formation of direct bonds when they are brought into contact at low temperature.

In the first approach, mating surfaces are cleaned with argon fast atom beam (Ar-FAB) followed by bonding in UHV. This method is particularly attractive for bonding between hard materials such as Cu/Cu [80], Si/GaAs [81][82], GaP/GaAs [83], and aluminum/stainless steel [84]. In the Cu/Cu direct bonding at the wafer-level, carbon and oxygen constituents were removed from the Cu surfaces by bombardment with low-energy Ar beam for about a minute. This produced a void-free contact between the Cu surfaces without the formation of any intermediate oxide layer. Such intermediate layers are usually undesirable for applications where electrical conductivity cannot be compromised.

In the second approach, metallic nano-adhesion layers (such as transparent Fe layers) are introduced on the mating surface during plasma-cleaning stage. The bonding

can be achieved in UHV with a low energy Ar ion source, or in HV with an Ar radio-frequency (Ar-RF) plasma. This technique is particularly attractive for flexible electronics and MEMS device packaging where bonding of ionic materials and flexible polymers is of significance [23][85][86].

In the third approach, the bonding surfaces are sequentially cleaned using oxygen reactive ion etching plasma (O_2-RIE) followed by nitrogen microwave radical treatment in low vacuum (LV). The activated surfaces become highly hydrophilic and undergo spontaneous bond formation at room temperature. This type of bonding is mediated by the formation of hydroxyl groups and oxynitride layers on the mating surfaces due to O_2-RIE and N_2 MW radicals respectively. Examples include bonding of wafer level glass/glass [87], Si/glass [88], and Si/Si [89][90].

The fourth approach is a hybrid extension of the sequential plasma activation technique. The O_2-RIE and N_2 MW radical-treated surfaces are contacted followed by the application of a potential during heating. This has been used to create void-free strong bonding at the wafer-level between Si/glass [91], Ge/glass [92], and glass/polymer [93]. Like sequential plasma activated bonding, hybrid plasma bonding is also mediated by hydroxyl groups that results in covalent bonds. The post-bonding anodic treatment causes opposite migration of cations and anions across the bonded interface [92]. It also enhances the amorphous oxide layer at the bonded interface and causes thermal rearrangement of plasma-induced reactive sites [93]. An illustration of the bonding mechanisms discussed above is presented next. For simplicity, two Si wafers are considered although the SAB fundamentals can be applied for integration of hard, flexible, and soft materials [23].

Figure 2-5. Different SAB approaches for bonding two silicon (Si) wafers [79].

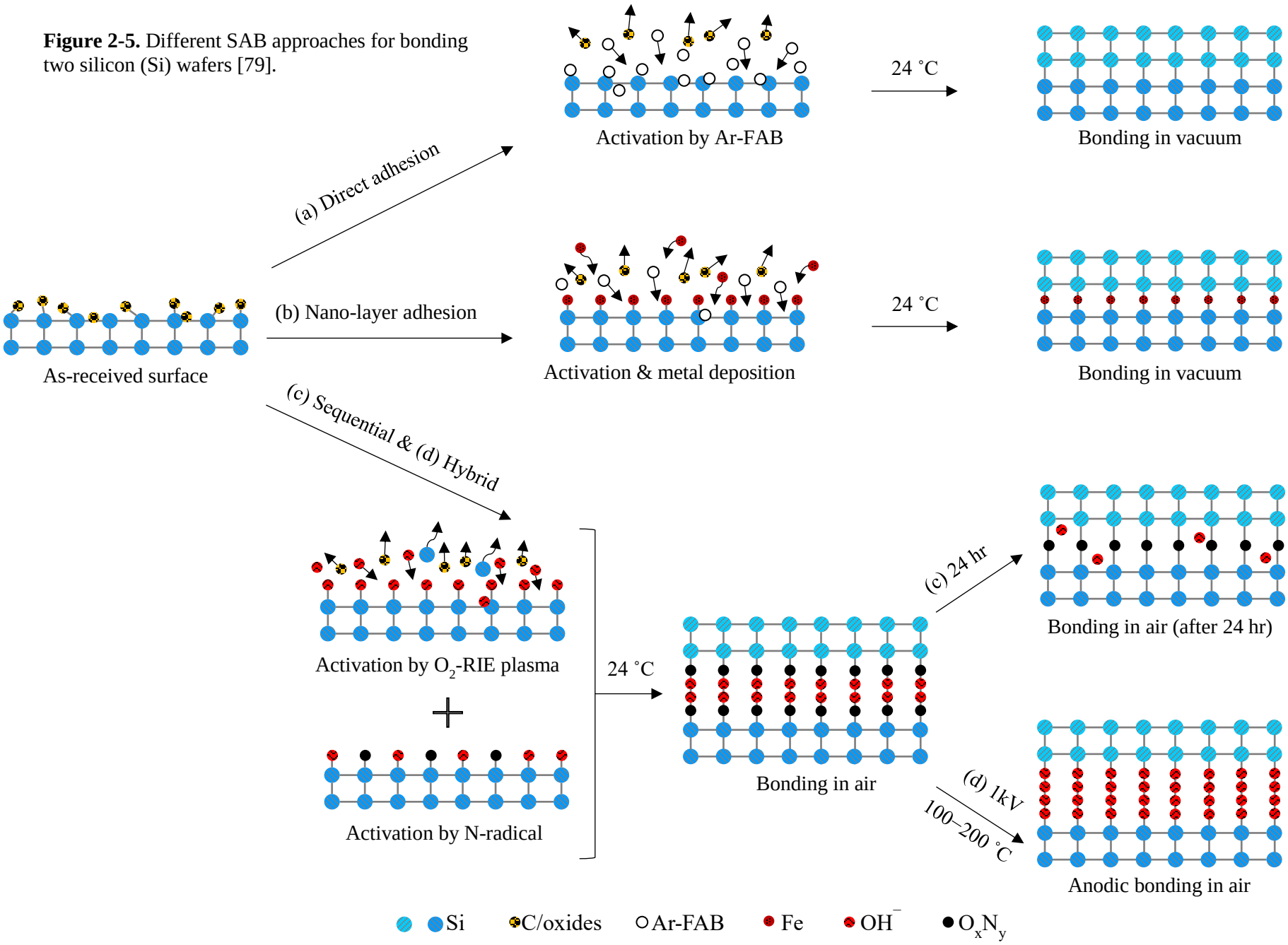

2.4 Fabrication and characterization tools

The Pb sensors developed in this work are based on Cu-foil sensing electrodes. These electrodes are fabricated on a plain sheet of Cu-foil that is directly-bonded to a polymer substrate. For this, we have developed a surface-activated bonding process for Cu/LCP (described in Chapter 3) followed by a comprehensive investigation of the bond mechanism using several characterization tools. Once fabricated, the sensors performances have been evaluated using electrochemical instrument. Here, we present a brief introduction of the bonding and characterization tools that have been used in this thesis.

2.4.1 Plasma surface activated bonder (PSAB)

Simultaneous activation of Cu-foil and LCP was carried out using a custom-built PSAB from Bondtech Co., Ltd (Japan). The PSAB has a vacuum chamber connected to a mechanical pump that can bring down the chamber pressure rapidly to a low vacuum (~1.33×10^{-1} Pa). We require this vacuum mainly due to two reasons: a) ionization of the gases introduced into the chamber, and b) the vacuum allows specific control of the type of gas in the chamber, hence providing control on the type of species we want to develop on the mating surfaces. The PSAB has O_2, N_2, and Ar gas inlets for generation of O_2-RIE plasma, N_2-MW radicals, or Ar-ion plasma, respectively. Plasma cleaning removes organic or carbon-based impurities, oxides, and other contaminants from the surface. PSAB also has a bonding head that can apply mechanical pressure, thermal heat, or an anodic potential. More discussion on process parameters used in this thesis are provided later in Chapter 3.

2.4.2 X-ray photoelectron spectroscopy (XPS)

XPS is a surface characterization technique that can identify the elemental composition, nature of the chemical bonds present, and electronic state of the elements that exist with a material. The fundamental operation principle of an XPS is based on the photoelectric effect, where electrons are ejected from a material because of the adsorption of very short wavelength radiation from standard x-ray sources. The emitted photoelectrons that reach a detector have a specific kinetic energy. This energy is in turn related to a binding energy that quantifies the energy required to remove the electron from material. Since binding energy is specific to the orbital of the element from which it came, XPS can identify an element and relate the peak intensity to the amount of the element within the sample. XPS is conducted in UHV conditions (~1×10^{-7} Pa) to remove as much adsorbed gas as possible (such as O_2, H_2O) from the sample prior to XPS analysis. This ensures a clear path for ejected electrons to reach the detector. In this thesis, we used a custom-designed XPS from JEOL (JPS-9200) to investigate the elemental composition of the bonding interfaces and material surfaces. For generating the x-ray, we used Magnesium source (Mg-α operated at 10 keV and 15 mA). Wide-scan and narrow-scan spectra were obtained with a binding energy resolution of 0.1 eV.

2.4.3 Fourier-transform infrared spectroscopy (FTIR)

Molecular bonds vibrate at various frequencies depending on the elements and the type of bonds. FTIR relies on the fact that the most molecules absorb light in the infra-red region of the electromagnetic spectrum. This absorption corresponds specifically to the

bonds present in the molecule. We obtained the attenuated total reflectance Fourier transform infrared (ATR-FTIR) transmittance spectra over the wavelength range 400−2000 cm^{-1} using a Bruker Platinum-ATR. By studying the absorbance spectra, we validated our XPS findings for the type of bonds present at the bonded Cu/LCP interface as well as on the surfaces of Cu and LCP.

2.4.4 High-resolution transmission electron microscopy (HRTEM)

The XPS and FTIR findings gave us evidence on chemical composition changes of activated Cu and LCP surfaces. We used these results to hypothesize a plausible bonding mechanism for Cu/LCP, and later validated our theory using high-resolution transmission electron microscopy of the bonded interface. HRTEM allows for direct imaging of the sample's atomic structure. Both High Angle Annular Dark Field (HAADF) and Bright Field (BF) Scanning Transmission Electron Microscopy (STEM) images were obtained, together with Energy Dispersive X-ray Spectroscopy (EDS) line scans to study the interfaces both structurally and chemically. TEM cross-sectional samples were prepared with a FEI Nova 200 dual-beam FIB/SEM by using the lift-out method. To protect the region of interest during focused ion beam milling, SiO_2 and Pt layers were deposited on top of the sample. Atomic STEM images were obtained in a JEOL ARM200F microscope equipped with a spherical aberration (Cs) corrector (CEOS GmbH, Heidelberg, Germany) and operated at 200 kV. The corrector was carefully tuned by the Zemlin-tableau method with Cs = 0.5 μm and the resolution was demonstrated to be around 1 Å. EDS line scan experiments were

performed with an Aztec Energy Advanced Microanalysis System with X-MaxN 100 N TLE Windowless 100 mm^2 analytical silicon drift detector.

2.4.5 Scanning electron microscope (SEM)

The SEM is a type of electron microscope that produces micro- and nano- scale images of a sample by scanning the surface with a focused electron beam. A scanning electron micrograph provides a clear view of the surface morphology. The electron beam is scanned in a raster-scan pattern, and the position of the beam is combined with the detected signal to produce an image with sub-nanometer resolution. In this thesis, we observed the pristine and post-activated-heated surfaces of Cu foil using a model JSM-7001F SEM from JEOL. The vacuum pressure of the SEM was 9.6×10^{-5} Pa.

2.4.6 Atomic force microscope (AFM)

Surface roughness of the bonding material is an important parameter in SAB processes and it affects the bond quality [23][79]. AFM is a very high-resolution type of scanning probe microscopy (more than 1000 times better than the optical diffraction limit) that can measure the roughness of a surface. In AFM, a mechanical probe (such as a Si-based tip) is tapped on the surface of interest to obtain information about the surface topography. For this thesis, we measured the surface roughness of 1×1 μm^2 Cu and LCP using an AFM (Dimension Icon, Bruker) with etched silicon tip tapping at 0.977 Hz. By investigating changes in surface roughness, we were able to identify the role of O_2-RIE plasma in Cu/LCP bonding.

2.4.7 Drop shape analyzer for water contact angles

In addition to surface roughness, surface hydrophilicity also plays an important role in bond quality [79]. The hydrophilicity of a surface is determined from its water contact angle – specifically this is the angle that the edge of a tiny droplet makes with the underlying surface. Highly hydrophilic surfaces (<< 45˚) are usually easier to bond with SAB. We measured the water contact angles of pristine and activated Cu and LCP surfaces using a drop shape analysis system (DSA100 from KRÜSS) with a 6 μL de-ionized water droplet. These results were used to conclude the Cu/LCP bonding mechanism.

2.4.8 Tensile peel tester

An indicator of good bonding and substrate adhesion is a high peel strength. This is integral to the reliable performance of the sensing electrodes. For the peel test, directly-bonded 1 cm wide × 5 cm long strip of Cu/LCP was debonded (~1 cm) from one side using a razor blade. These razor-peeled ends of Cu and LCP were then clamped to the top and bottom tensile jigs of a Shimadzu AG-X tensile pulling tester and pulled apart (180˚) at 30 mm/min. The real-time peel force was recorded over the remaining specimen length.

2.4.9 Electrochemical sensing with potentiostat

All electrochemical experiments with the fabricated Pb sensors were performed with a miniature USB powered potentiostat (EmStat3) from PalmSens. Voltammograms were analyzed with PSTrace data analyzer. Further details on electrochemical sensing parameters optimization is provided in Chapter 4.

Chapter 3

Sensor fabrication

For sensor fabrication, we report two approaches to prepare the electrode base. The first approach is based on surface activated bonding (SAB) of rolled-annealed (RA) Cu-foil and liquid crystal polymer (LCP) substrate. Throughout this thesis, sensors that were fabricated on these directly bonded Cu/LCP specimens are referred to as Type 1 sensors. This thesis required the fabrication of a significant number (~200) of sensors for sensing parameter optimization (further detailed in Chapter 4). To accommodate this need and to compare the sensing performance between directly bonded and commercially available laminate, we fabricated a Type 2 sensor based on Cu/polyimide (PI). Both Type 1 and Type 2 sensors are similar in terms of electrode material (RA Cu-foil) and polymer substrate (LCP or PI), so they provide comparable sensing response and compatibility with a single fabrication process.

We commence this chapter by outlining the materials and reagents used for sensor fabrication. We describe in detail the SAB process parameter optimization towards accomplishing an adequate bond strength of Cu/LCP to prevent delamination during use. We then demonstrate an inexpensive LaserJet printing process for developing Pb sensors

on Cu/LCP and Cu/PI, followed by sensor packaging. Finally, we discuss the fundamentals of the Cu/LCP bonding mechanism.

3.1 Materials and reagents

The proprietary LCP film (Vecstar CTX-100) used as Type-1 sensor substrate was from Kuraray Co., Ltd. Japan. CTX100 is a 50 μm-thick sheet of an aromatic polyester made from block co-polymers of 4-hydroxybenzoic acid (also known as para-hydroxybenzoic acid, PHB) and 2-hydroxy-6-naptholic acid (also known as bi-oxide 6-naptholine acid, BON6) as shown in Fig. 3-1 [93][94]. The electrodes of Type-1 sensors were based on 50 μm-thick Cu-foil purchased as 6" × 50" rolled stock from McMaster-Carr. For fabricating Type-2 sensors, we used proprietary Cu clad (18 μm-thick) laminate on a 12 μm-thick flexible PI substrate from DuPont (Pyralux AC181200R). All specimens of Cu, LCP, and Cu/PI were cleaned with acetone in a class 1000 cleanroom environment prior to SAB. Cu etchant was prepared using a 1:1 v/v mixture of 1 M HCl and 30% H_2O_2. $Cu/CuCl_2$ reference electrode was anodically chlorinated with 1.0 M KCl.

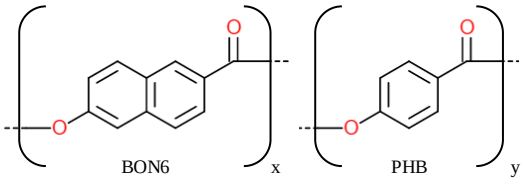

Figure 3-1. Schematic diagram of the chemical structure for Vecstar CTX100 [93].

3.2 Sensor fabrication

3.2.1 Surface activated bonding of Cu and LCP

The direct bonding of Cu/LCP was achieved with plasma surface activated bonder (PSAB). Pre-cleaned Cu and LCP were placed on the stage of the plasma chamber. The mechanical pump controlling the vacuum of the chamber was then turned on and the gas valve was slowly released to initiate vacuuming. After about 30 minutes, the chamber base pressure reached 2×10^0 Pa and the system was ready to generate plasma. As mentioned in Section 1.2, previous works on argon radio frequency (Ar-RF) plasma-assisted Cu/LCP bonding required high activation power (~700 W), high irradiation time (~ 30 min), high contact pressure (~ 800 MPa), and a metallic adhesion underlayer on LCP [54][55]. In this thesis, we bonded Cu/LCP using less stringent process parameters, similar to the O_2-RIE assisted hydrophilic bonding of Si wafers [95]. We introduced 98 sccm O_2 gas flow into the chamber and generated 100 W O_2-RIE plasma at 100 Pa chamber pressure. Simultaneous activation of Cu and LCP surfaces was carried out for 240 s. Once activated, the specimens were taken out in cleanroom ambient followed by contacting the plasma-treated surfaces. The contacted Cu/LCP was then heated at 230 ˚C for 1 hour under 0.3 MPa mechanical pressure exerted by a bonding head. Following heat treatment, the bonded specimen was taken out of the bonding chamber and the Cu side was polished using 800/2400 grit SiC paper. This removed the oxides from Cu surface that formed due to thermal oxidation in air. Further discussion on SAB process parameter optimization is provided in Section 3.3.3. The described SAB process is illustrated in Fig. 3-2.

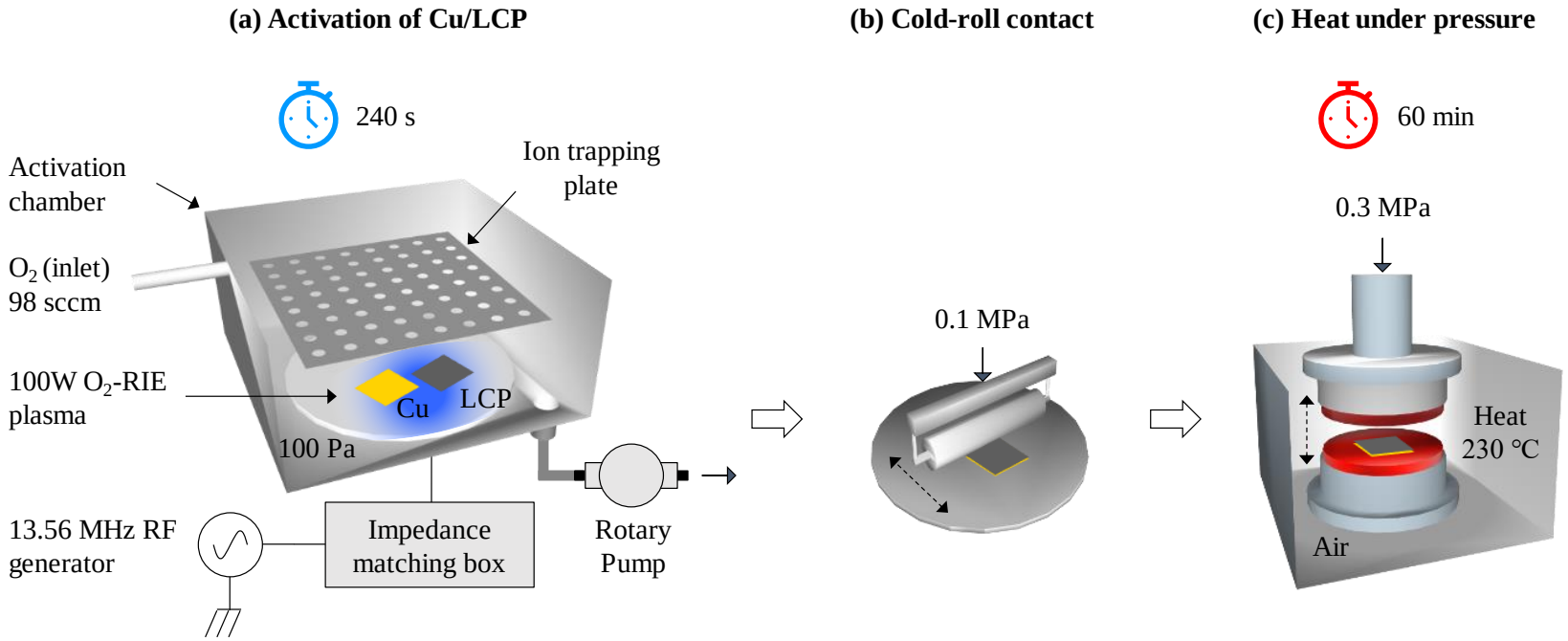

Figure 3-2. Illustration of the SAB process for Cu/LCP.

Table 3-1. SAB process parameters for Cu/LCP bonding.

Process Parameter	Value
RIE power (W)	100
RIE time (s)	240
O_2 flow (sccm)	98
Vacuum Pressure (Pa)	100
Bonding temperature (ºC)	230 for 1 hour
Bond-head pressure (MPa)	0.3

3.2.2 Electrode patterning and sensor packaging

The fabricated sensor has a three-electrode configuration − the auxiliary, working, and reference electrode. These electrodes collectively establish control and measurement of both potential and current through the sensor to detect the electrochemical signature of Pb. The WE and the CE sustain the cell current while the RE measures and controls the potential of the WE. From the review of electrochemical Pb sensors, we identified some important design criteria for our sensor:

1) The inter-electrode spacing should not be too low. Smaller electrode gaps provide faster response, but also introduce noise at low Pb levels [43].
2) The WE surface area should be sufficiently large. This provides more binding sites for deposition of Pb atoms, hence results in stronger stripping currents [11].
3) The AE should be placed further away from the WE to minimize the effect of interference caused by bubble generation at the AE [68].
4) The AE area should be higher than that of WE to reduce hydrolysis effect [68].
5) The RE should not be easily polarized [96]. For this reason, commercial Ag/AgCl RE are installed inside a porous glass tube with an inner filling of concentrated KCl. For microelectrodes not embedded in any solution, this can be achieved by increasing the thickness of the chloride layer, as demonstrated for $Cu/CuCl_2$ and Ag/AgCl reference microelectrodes [36][68].
6) The electrolyte should not consume the electrodes [96]. This issue may be addressed by using thick film electrodes.

We designed our sensor layout based on these considerations. The design is shown in Fig. 3-3, which also schematically shows the fabrication process. The main steps in fabricating these electrodes are mask transfer followed by wet etching (steps (b) and (c) in Fig. 3-3). In most other studies reported in the literature, the electrodes are fabricated using a photolithography process which involves: a) spin-coating a photoresist on the specimen, b) preparing and aligning a physical mask, c) curing the resist in UV light followed by patterning in developer solution, and d) bulk etching and cleaning the photoresist. We used an inexpensive and fast alternative. The CAD drawn mask was transferred directly on the Cu side of both Type 1 and 2 specimens using a HP LaserJet 4250n printer. The toner ink is a polyester-based resin that can serve as a protective mask during wet etching of Cu electrodes. Sensors were cut out from the printed Cu/polymer sheets and etched in a beaker. After etching, the mask was wiped off using acetone followed by rinsing in DI water for 30 s. The all-polymer side of the sensor base was then attached to a clean glass slide using epoxy adhesive. A standard single-hole puncher was used to create a 6-mm-diameter hole through the center of a 17×15 mm^2 sized, 4-mm-thick PDMS encapsulant (separately prepared). The encapsulant hole was then aligned with the electrodes and bonded to the base specimen using plasma discharge and transparent epoxy [97]. Next, we chlorinated the reference electrode by adding 1.0 M KCl into the PDMS-well and setting up an electrolytic cell between RE (anode) and AE (cathode). When a 5V potential was applied to this cell for 300 s, the surface of the Cu RE was anodically chlorinated to $CuCl_2$. Finally, the sensor was briefly rinsed in DI water, dried, and stored in a sealed container before use. The material cost estimated to fabricate a sensor using our technology is 15 ¢/sensor.

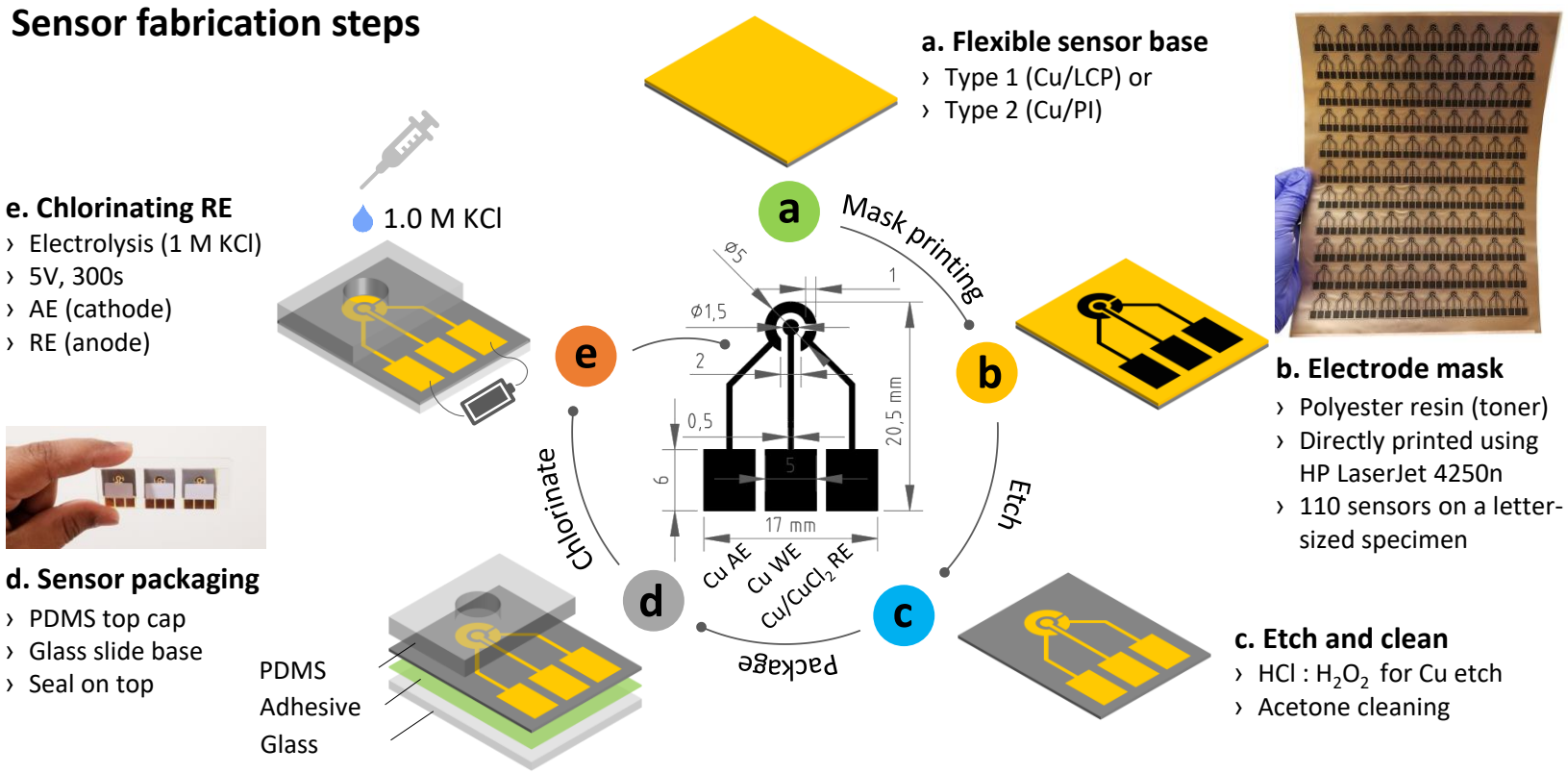

Figure 3-3. (a-e) Pb sensor fabrication steps. Inset illustrates the electrode size. A letter-sized flexible specimen can accommodate 10×11 sensors.

3.3 Development of SAB process for Cu/LCP

The effects of SAB parameters on adhesion of the bonded Cu/LCP specimens were evaluated in terms of their peel strengths. The peel strength was determined as a function of the O_2-RIE plasma power, irradiation time, and bonding temperature.

3.3.1 Preliminary development

As a preliminary investigation, we activated both Cu and LCP using a 100 W O_2-RIE plasma for 60 s. The plasma was generated at 100 Pa that was maintained by adjusting a mass flow controller to introduce 20 sccm O_2 into the chamber. Following activation, Cu and LCP were contacted and heated at 200 ºC in the bonding chamber. The resulting specimen showed no adhesion. Increasing the O_2 flow rate into the PSAB to a maximum 98 sccm supported by our setup improved the adhesion. Raising the irradiation power to 300 W increased the adhesion further to some extent but caused surface burns in the Cu foil. We therefore considered a two-stage activation next.

3.3.2 Two-stage activation and bonding of Cu/LCP

Cu foil surface seemed to degrade at RF power greater than 100 W, thus we adopted a two-stage process with the intention of activating LCP using a stronger plasma while not degrading the Cu foil. In this two-stage process, the as-received LCP film alone was activated at 100, 200, or 300 W (stage 1) and then both the pre-activated LCP and the as-received Cu underwent simultaneous activation with 100 W RF plasma (stage 2). The pre-

activated LCP was included in stage 2 activation so as not to keep the specimen exposed to air during Cu activation. The process parameters used in this two-stage activation were:

Table 3-2. SAB parameters of two-stage activation and bonding of Cu/LCP. The numbers in boldface were found to produce the best results for the two parameters optimized (stage 1 activation power and bonding temperature).

Parameters	Stage 1 (LCP only)	Stage 2 (LCP & Cu)
RIE power (W)	100, 200, or **300**	100
RIE time (s)	100	100
O_2 flow (sccm)	98	98
Vacuum pressure (Pa)	100	100
Bonding temperature (ºC)	200 or **230 ºC** for 1 hour	
Bond head pressure (MPa)	0.215	

The peel strengths obtained from Cu/LCP specimens bonded using the two-stage activation process were significantly higher than our preliminary attempts. The peel strength of Cu/LCP for specimens that were bonded at 230 ºC were higher than that of 200 ºC. We did not heat Cu/LCP at temperatures higher than 230 ºC to preserve the structural integrity of LCP. The glass transition temperature of LCP is ~280 ºC, but the heat should be kept below 260 ºC to avoid thermal contraction that yields poor adhesion [47][54].

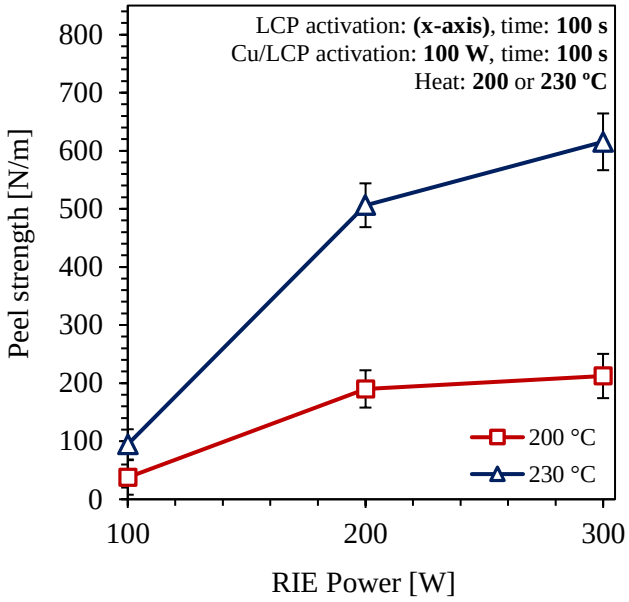

Figure 3-4. Influence of (LCP) activation power and bonding temperature on peel strength [47]. The peel strength of three specimens was tested against each combination of plasma power and bonding temperature to obtain the standard deviation (n = 3 repeats).

As shown in Fig. 3-4, the peel strength increased with increasing plasma power and bonding temperature. An increase in RF power causes more precursor molecules of oxygen to ionize in the chamber at low vacuum. In other words, a more intense plasma produces more reactive ions to attack and atomically clean the surfaces of Cu and LCP whereas a low-power plasma may not completely remove carbon contaminants and native oxides. Oxygen plasma etching forms hydroxyl (OH^-) groups [98] on the treated Cu and LCP surfaces. An increase of plasma power (from 100 to 300 W) and bonding temperature (from 200 to 230 ºC) result in better surface activation. These suggest that both higher temperature and higher plasma power yield better Cu/LCP adhesion.

3.3.3 Single-stage-activated bonding of Cu/LCP for sensor base

The scope of this thesis is to develop a simple approach to develop Pb sensors, thus a reduction in materials processing stages is desirable. For this, we varied plasma irradiation time according to Table 3-3 to investigate the trade-off between activation times and powers of the discussed two-stage activation process. In this experiment, we wrapped the contacted Cu/LCP specimen with tissue pads before heating them under mechanical pressure in the bond chamber. It is a common practice to heat specimens in between glass wafers to obtain uniform bonding. Tissue pads are low-cost alternative that accommodate Cu foil expansion during heating, thus avoiding voids or thermally induced stress at the bonded interface.

Table 3-3. SAB parameters of two-stage activation and bonding of Cu/LCP.

Parameters	Stage 1 (LCP only)	Stage 2 (LCP & Cu)
RIE power (W)	150	100
RIE time (s)	60	60
	100	100
	180	180
O_2 flow (sccm)	98	98
Vacuum pressure (Pa)	100	100
Bonding temperature (ºC)	230 ºC for 1 hour	
Bond head pressure (MPa)	0.215	

Fig. 3-5 shows the result of this experiment. The peel strength of Cu/LCP is improved by prolonging the plasma irradiation time. This is because longer activation cleans the surfaces for longer duration and creates more OH^- bonding sites. This makes the surfaces more hydrophilic that are easy to bond. More discussion on surface hydrophilicity will be provided in Section 3.4. Fig. 3-6 shows that heat pads improve the bond uniformity.

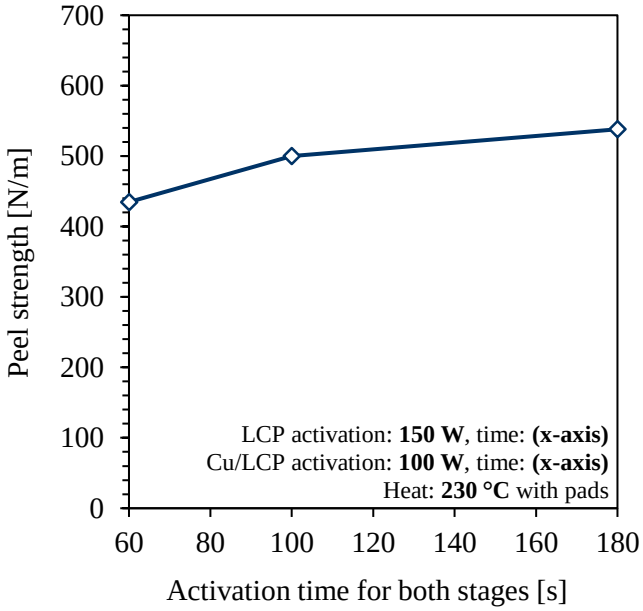

Figure 3-5. Influence of plasma irradiation time on peel strengths of double-stage-activated and bonded Cu/LCP.

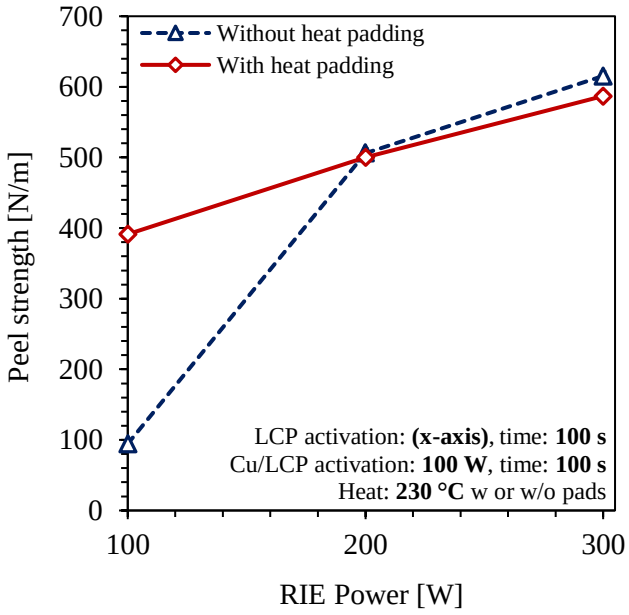

Figure 3-6. Improvement of Cu/LCP adhesion by using tissue pads.

The results of Figs. 3-5 and 3-6 provided us with evidence based on which we further optimized the bonding process: a) Cu/LCP adhesion increases with increasing RF power and bonding temperature, b) longer activation time increases the peel strength, c) wrapping the Cu/LCP specimen with tissue pads during heating improves the bond quality, and d) LCP bonds with Cu even at lower RF power. These observations led us to developing a single-stage activation process for bonding Cu/LCP.

For the single-stage-activated bonding of Cu/LCP, pre-cleaned Cu and LCP specimens were simultaneously subjected to 100 W O_2-RIE plasma. Peel strength dependencies on irradiation time and bonding temperature were investigated by varying activation times between 120, 180, and 240 s and heated at 215 or 230 °C:

Table 3-4. SAB parameters of single-stage activation and bonding of Cu/LCP. The numbers in boldface were found to produce the best results for the two parameters optimized (single stage plasma activation time and bonding temperature).

Process Parameter	Value
RIE power (W)	100
RIE time (s)	120, 180, or **240**
O_2 flow (sccm)	98
Vacuum Pressure (Pa)	100
Bonding temperature (°C)	215 or **230 °C** for 1 hour
Bond-head pressure (MPa)	0.3

As expected, higher temperature (230 °C) and longer activation (240 s) provided the highest peel strength (Fig. 3-7). We also investigated the reproducibility of single-stage activation and bonding of Cu/LCP at various activation times using 4 specimens at each combination.

For this investigation, plasma power and bonding temperature were fixed at 100 W and 230 °C respectively. Fig. 3-8 shows the deviation in peel strengths obtained from these specimens. Overall, we settled for 100 W, 240 s, and 230 °C as optimized SAB parameters for bonding Cu/LCP specimens using single-stage plasma activation.

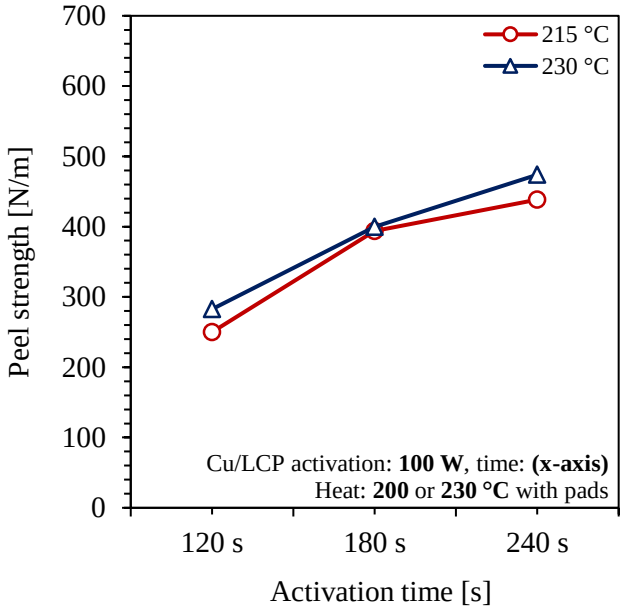

Figure 3-7. Influence of plasma irradiation time and heat on peel strengths of single-stage-activated and bonded Cu/LCP.

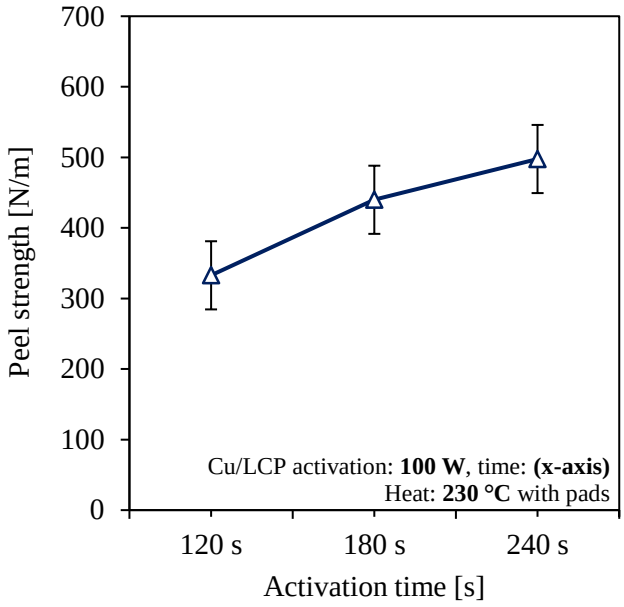

Figure 3-8. Peel strength reproducibility of single-stage-activated and bonded Cu/LCP.

3.4 Characterization of directly bonded Cu/LCP

We characterized the surfaces of as-received (pristine) Cu and LCP films, the activated surfaces of Cu and LCP prior to contact, the delaminated surfaces of Cu and LCP after peel test, and the activated and heated Cu foil surface not contacted with LCP or any other surface at all. The results are discussed in this section.

3.4.1 FTIR analysis

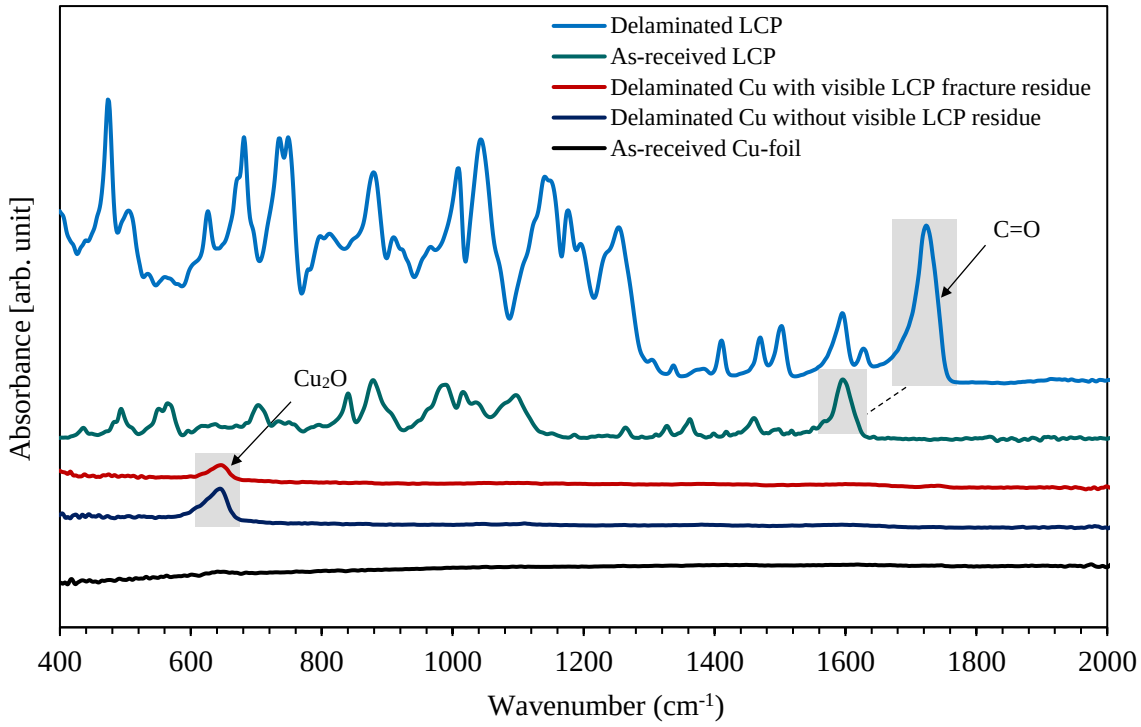

Figure 3-9. Attenuated total reflectance FTIR absorbance spectra of different interest regions as marked (bottom to top).

The FTIR−ATR absorbance spectra of the electrode specimen were obtained for the range 400−2000 cm^{-1} (Fig. 3-9). In contrast to as-received Cu foil, delaminated Cu foils (after peel test) show coincided peaks of varying intensities at 650 cm^{-1} (shaded). These peaks represent Cu_2O on Cu [99][100]. The Cu_2O peak is higher for the delaminated Cu foil without any residual LCP covering it than its counterpart where Cu surface is covered with visible fractured LCP. The reason is because an absence of visible residue lets us

examine the actual debonded interface of Cu/LCP where Cu_2O is higher. In the presence of visual LCP residue, our observation is mostly on the fractured bulk of LCP. Presence of Cu_2O in this region may suggest that some Cu_2O bonds from Cu side might have crossed the LCP interface into its bulk during bonding.

Furthermore, we identify stretching of C=O peak [101] at approximate frequencies of 1660 cm^{-1} and 1710 cm^{-1} for as-received and delaminated LCP films respectively. The C=O peak intensity of the delaminated LCP is higher than the as-received LCP film, although it is expected that the C=O peak of the delaminated LCP should be weaker because of the breaking of C=O bonds during oxygen plasma activation. One reason why we observe a stronger C=O peak in delaminated LCP may be due to the shearing of the activated layers on LCP surface during delamination, thereby exposing the bulk LCP itself which has more C=O bonds. The other reason could be an increase of C=O bonds between the C side chains of LCP and oxide layer at the Cu/LCP interface due to plasma-induced thermal oxidation in air. The frequency shift of the C=O peak is because of a change in population of different chemical species [101]. These observations are confirmed next from XPS analysis.

3.4.2 Elemental analysis with XPS

We identified the bonding mechanism and validated our FTIR findings using XPS analysis. All curve fitting was performed using a Gauss/Lorentz mixed function and employing Shirley background correction [103][104][105].

LCP is made from a mixture of acetoxy benzoic acid and acetoxy naphthoic acid by polycondensation reaction that produces end groups of −COOH (from BON6) and $-O-C=O-CH_3$ from PHB components respectively [93][102]. The deconvolved C_{1s} spectra in Fig 3-10 show the concentration of different bonds present in as-received and activated LCP. The peaks labeled (1) to (5) are identified as C−H, C−C=O, C−O, O−C=O and C=O groups respectively. Plasma activation removes organic contaminants and hydrocarbons from the LCP surface [47]. This is indicated by the decrease in the C−H peak (1) on the surface of activated LCP. Plasma cleaning also causes physical etching of the surface, thus exposing the LCP bulk. For this reason, the intensity of major C−C peak (2) at 284 eV is higher in activated LCP than that in as-received. An increase in C−C bond could also signify that O_2-RIE attacks the unsaturated C=C bonds on LCP surface to form singly bonded C−C. The saturated C−O peaks (3) at 285.3 eV are slightly affected by activation, but significant increase of O−C=O peak (4) at 286 eV and C=O peak (5) at 288 eV are observed. These suggest an increase in overall surface oxide on LCP. Alam (2016) [93] reported a similar increase in O−C=O peak. An increase in highly reactive oxide groups accelerates the bonding between contacted surfaces.

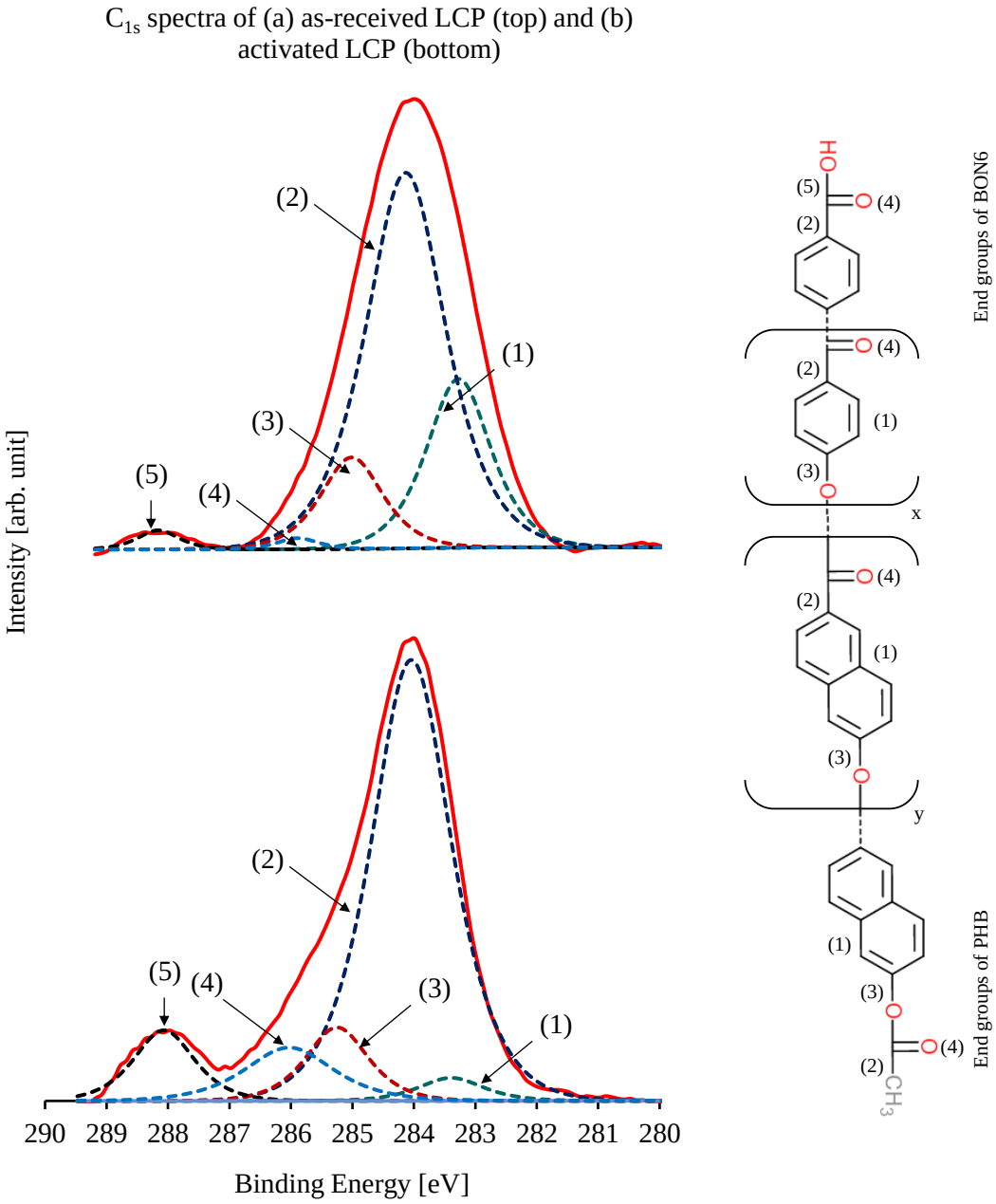

Figure 3-10. C_{1s} spectra of (top) as-received and (bottom) activated LCP. Inset shows the end chain groups of BON6 and PHB in LCP.

To further investigate on the nature of the oxide developed at the Cu/LCP interface, we turn to XPS analysis of the as-received and activated Cu foil. Figs. 3-11 and 3-12 show the $Cu_{2p3/2}$ and O_{1s} spectra of these regions respectively.

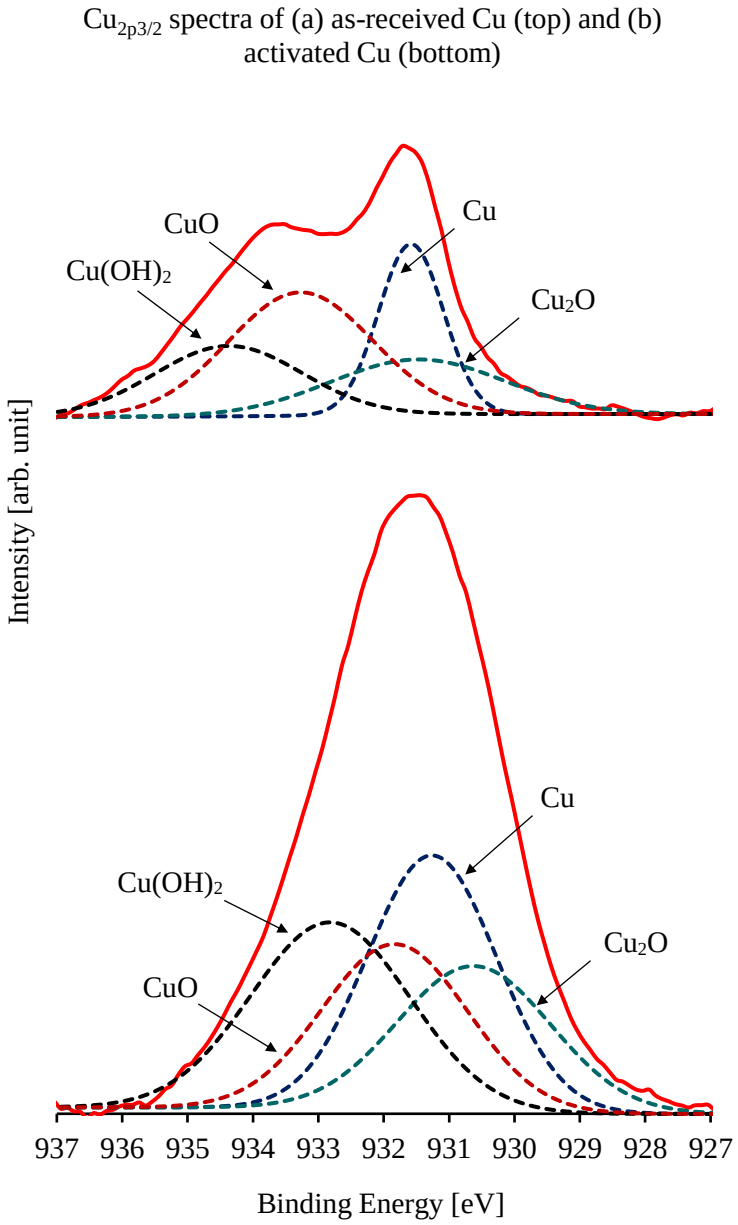

Figure 3-11. $Cu_{2p3/2}$ spectra of (top) as-received and (bottom) activated Cu.

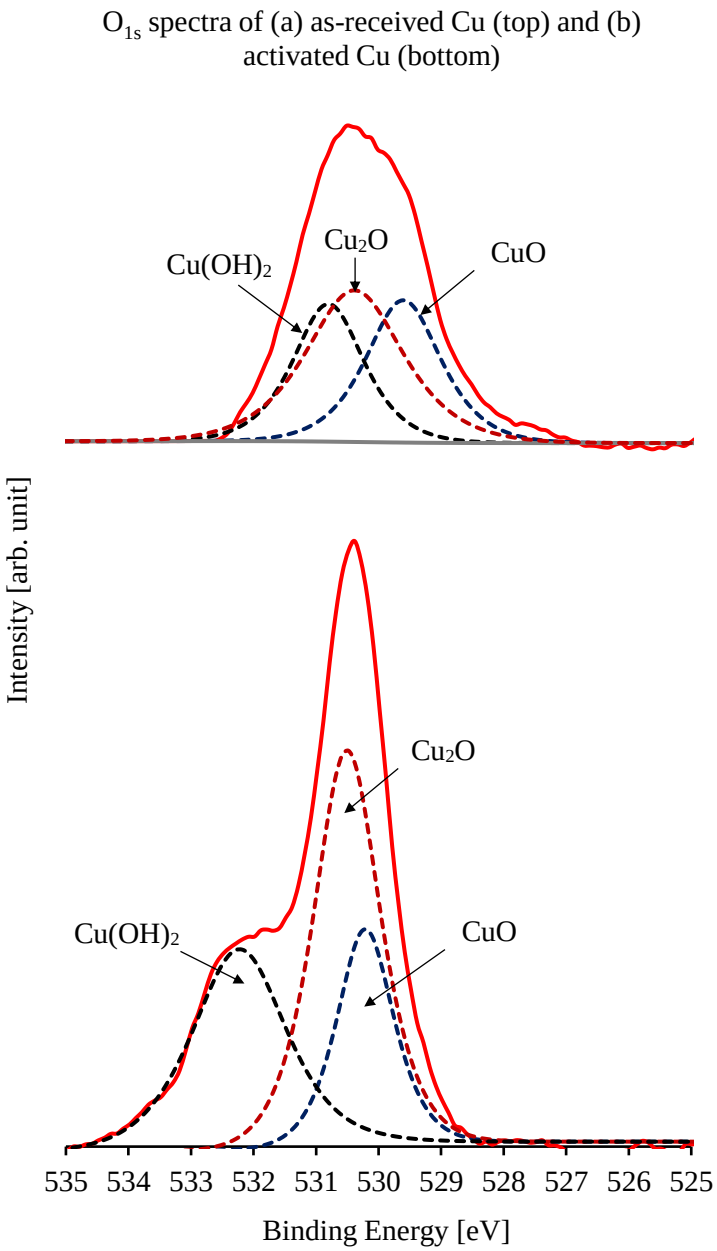

Figure 3-12. O_{1s} spectra of (top) as-received and (bottom) activated Cu.

As Fig 3-11 shows, Cu_2O makes up 20.6% of the surface constituents for activated Cu compared to a 19.5% presence in as-received Cu. The peaks at ~931.2 eV correspond to metallic Cu. Since O_2-RIE plasma cleaning removes hydrocarbons and other contaminants from the surface, more atomically clean Cu surface is obtained that results in higher concentration of Cu in activated Cu (30.2%) than that in as-received Cu (22.6%). Plasma cleaning also removes native oxides of CuO from the Cu surface, and this is confirmed from the decrease in CuO peak from 36.5% in as-received Cu to 22.1% in activate Cu. Finally, the formation of hydroxyl groups on the dangling sites of activated Cu foil is a characteristic behavior of O_2-RIE plasma. This formation is followed by the adsorption of water molecules when the activated specimen is exposed to air [47]. The result is an overall increase of $Cu(OH)_2$ bonds from 21.3% to 27.1%.

The results of $Cu_{2p3/2}$ spectra in Fig. 3-11 are consistent with the O_{1s} spectra of Fig. 3-12. The CuO peak at ~530 eV is higher for as-received Cu (30.4%) which decreases to 21.2% after activation. This plasma-assisted removal of native oxide is accompanied by the formation of new oxide groups of Cu_2O at ~530.5 eV (from 41.9% to 45.7%) in activated Cu. Formation of new hydroxyl groups are also confirmed from O_{1s} spectra. The XPS findings discussed in this section are in good agreement with the FTIR spectra. A summary of these results can be made as follows:

1) O_2-RIE plasma cleans native oxides of CuO from Cu surface.
2) The removal of CuO is accompanied by the formation of new oxides of Cu_2O in Cu.
3) Plasma modification creates new hydroxyl groups on Cu and LCP surfaces.
4) Highly reactive oxide groups O−C=O and C=O are formed on LCP.

3.4.3 Surface hydrophilicity and roughness

Surface hydrophilicity and surface roughness play an important role in surface activated bonding [79]. The hydrophilicity of the surface is an indicator of the surface energy that affects the quality of the direct bonding [106]. Specifically, surfaces that are highly hydrophilic are easier to bond [90]. Surface roughness on the other hand is a general indicator of the type of mechanical interlocks present on a surface that affect adhesion between surfaces. While a high surface roughness may be desirable for some integration or adhesive applications, a smooth surface is required for surface activated bonding [79]. In this section, we investigate the effect of O_2−RIE plasma activation on changes in surface hydrophilicity and roughness.

Surface hydrophilicity of a specimen is studied by measuring the contact angle of a drop of water on its surface. For hydrophilic surfaces, the contact angle usually remains much less than 45˚, and it is usually higher than 45˚ for hydrophobic surfaces [90]. Our investigation shows that the surfaces of as-received Cu and LCP are hydrophobic with contact angles of 79˚and 83˚ respectively (Figs. 3-13(a)-(b)). This is mainly due to the benzene and naphthalene groups of LCPs [93] and the native oxide on Cu that have low chemical affinity to hydroxyl groups in water. The Cu and LCP surfaces become highly hydrophilic after O_2−RIE plasma activation and their contact angles reduce to 13˚ and 11˚ respectively (Figs. 3-13(c)-(d)). This is due to the formation of OH^- groups on the dangling bonds (free bonds) at the oxide and carbonyl groups of Cu and LCP [47][93][107]. When the contacted Cu and LCP are heated, these OH^- chains condense through dehydration and forms a strong bond between Cu/LCP via an intermediate oxide layer [47].

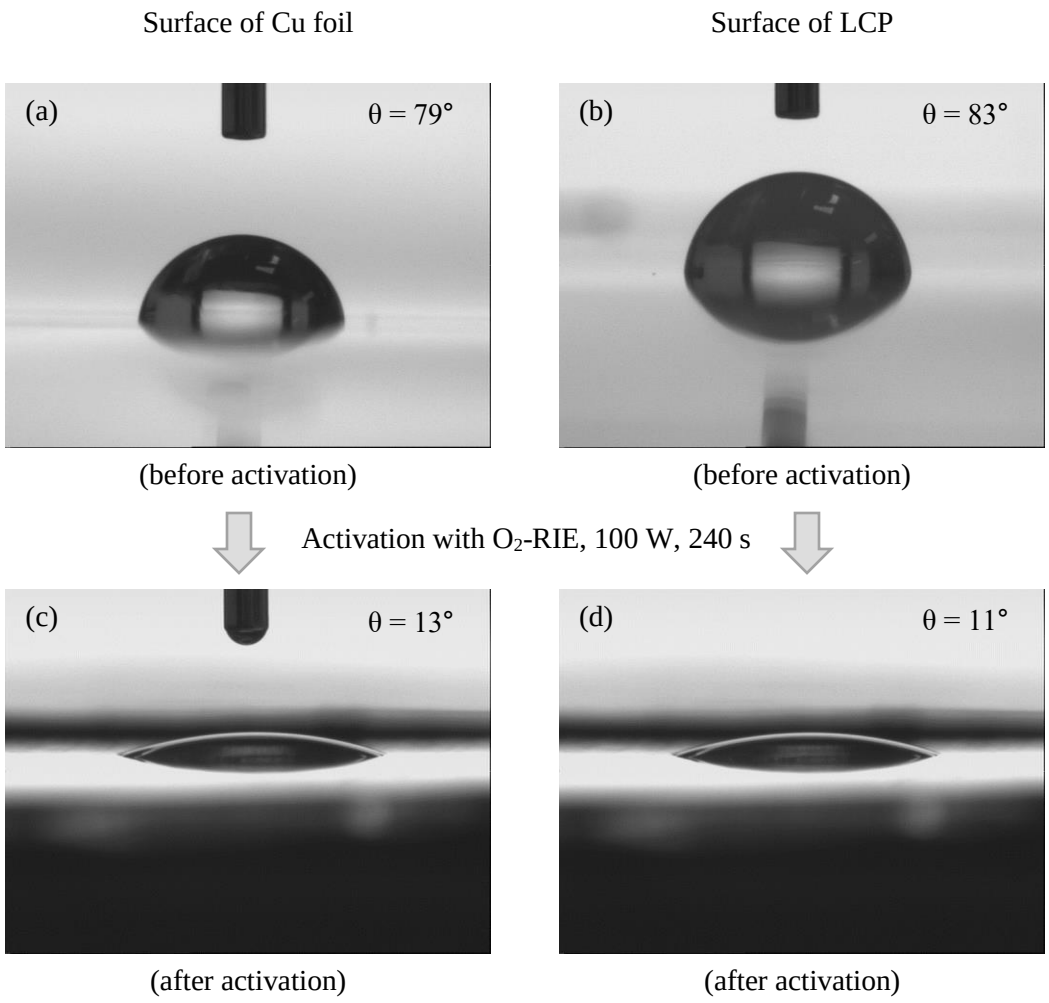

Figure 3-13. Water contact angles measured on: (a) as-received Cu foil, (b) as-received LCP, (c) activated Cu foil, and (d) activated LCP.

A decrease in water contact angle as demonstrated above signifies the highly hydrophilic behavior of activated films, but water contact angle needs to be studied in conjunction with surface roughness. This is because water contact angle depends on both surface hydrophilicity and surface roughness [90]. A surface with a higher surface roughness has microgaps where air gets trapped between the surface and the water droplet.

This trapped air then increases the water contact angle, which is why rough surfaces usually have higher contact angles compared to smooth surfaces. The O_2−RIE plasma treatment is a physical bombardment process that etches the surface and can change the surface roughness. For this reason, we measured the root mean square (rms) surface roughness of activated films to study the effect of O_2−RIE activation.

The rms roughness of as-received and activated LCP were 2.06 nm and 5.09 nm respectively (Fig. 3-14). The increase in roughness is due to etching or ion bombardment during plasma activation. For Cu, there was no prominent change in surface roughness after activation (Fig. 3-15). The roughness of as-received Cu was 8.91 nm that slightly increased to 9.01 nm after plasma treatment. These roughness investigation results suggest the following:

1) Fig. 3-14(b) shows clear evidence of a cleaner surface in activated LCP. This could indicate removal of hydrocarbon-based contaminants in activated LCP that accounts for C−H peaks reduction (C_{1s} spectra in Fig. 3-10).

2) Since plasma changes the roughness of activated LCP, it is possible that the contact angle of 11˚ in Fig. 3-13(d) is slightly affected by surface roughness change. However, that would tend to increase the contact angle making the surface appear more hydrophobic. The formation of hydroxyl groups plays a dominant role in the contact angle since the activated LCP is still highly hydrophilic after an increase in rms roughness value.

3) The contact angle change in as-received and activated Cu is due to the formation of hydroxyl groups alone. The bonding conditions of Table 3-4 are sufficiently optimized to form enough OH^- groups for Cu/LCP bonding without sacrificing Cu roughness.

(a) as-received LCP

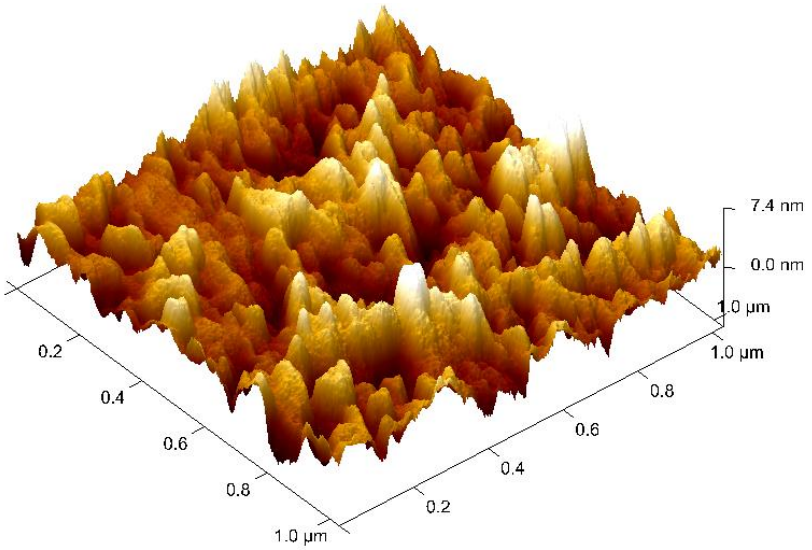

(b) activated LCP

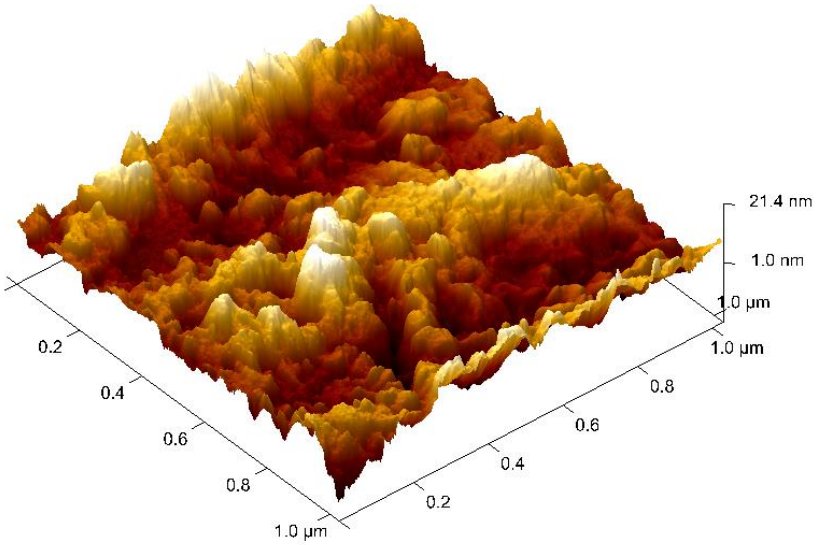

Figure 3-14. Root mean square surface roughness of: (a) as-received LCP, and (b) activated LCP.

(a) as-received Cu

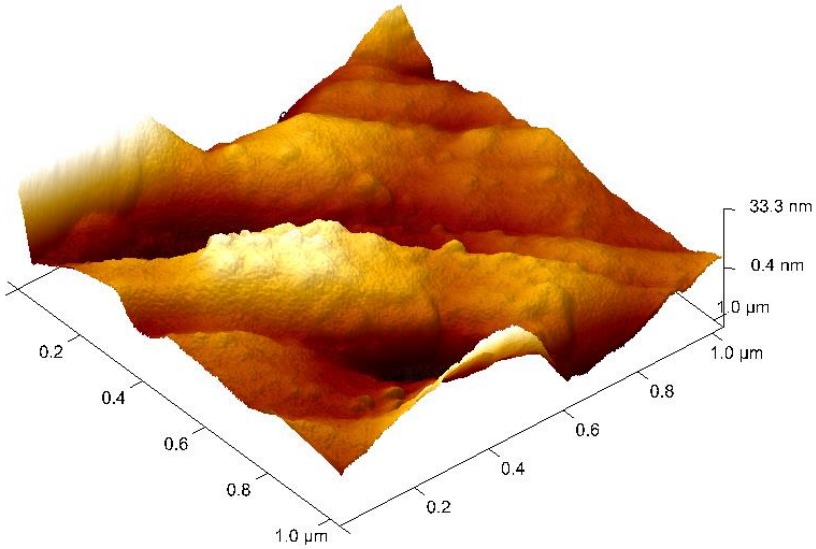

(b) activated Cu

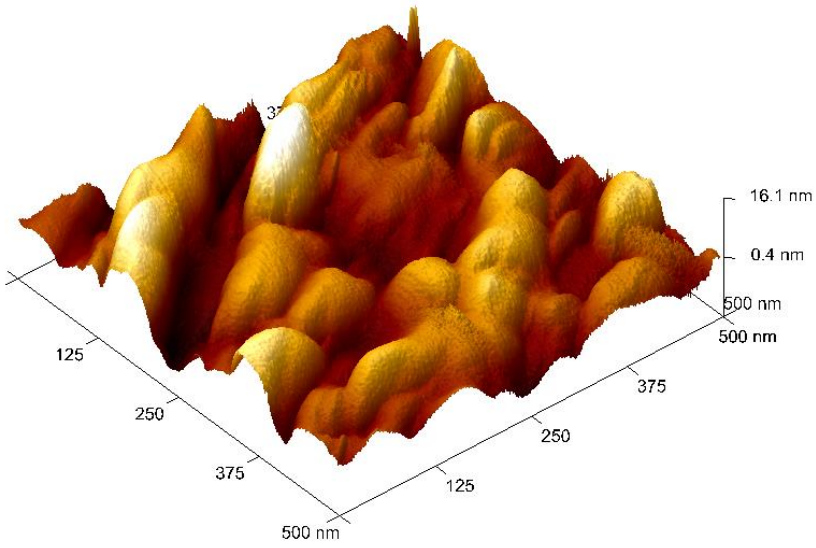

Figure 3-15. Root mean square surface roughness of: (a) as-received Cu, and (b) activated Cu.

3.4.4 Surface imaging and interface profiling

O_2-RIE activation of Cu and LCP forms a direct bonding that is mediated by OH^- groups formation on both mating surfaces, and an increase in Cu_2O species on the surface of Cu. Since the bonding is achieved by heat conditioning, we expect thermal growth of an oxide layer on Cu. To verify this, we observed the bonded interface of Cu/LCP with HRTEM. Additionally, we heated a plasma-treated Cu foil separately without LCP contact, and observed the resulting Cu surface with a SEM.

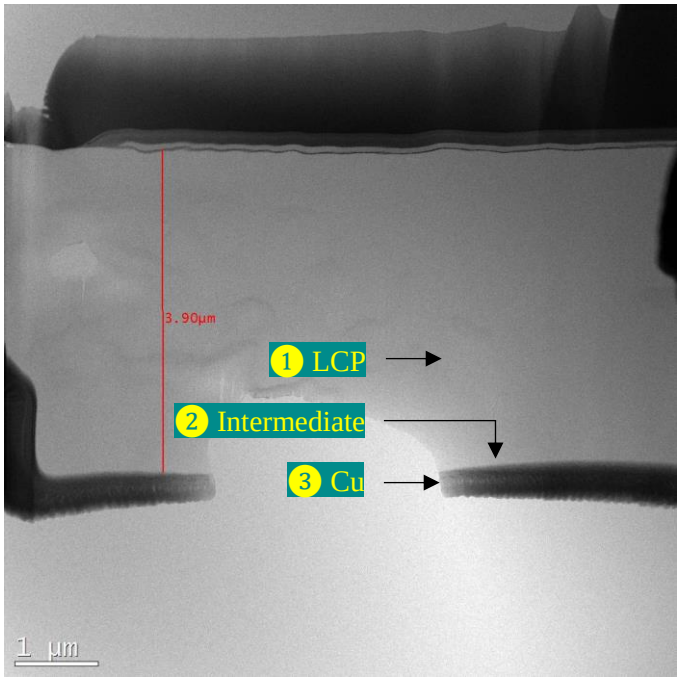

Figure 3-16. Low-magnification (cross-section) image of Cu/LCP showing a smooth bonding interface.

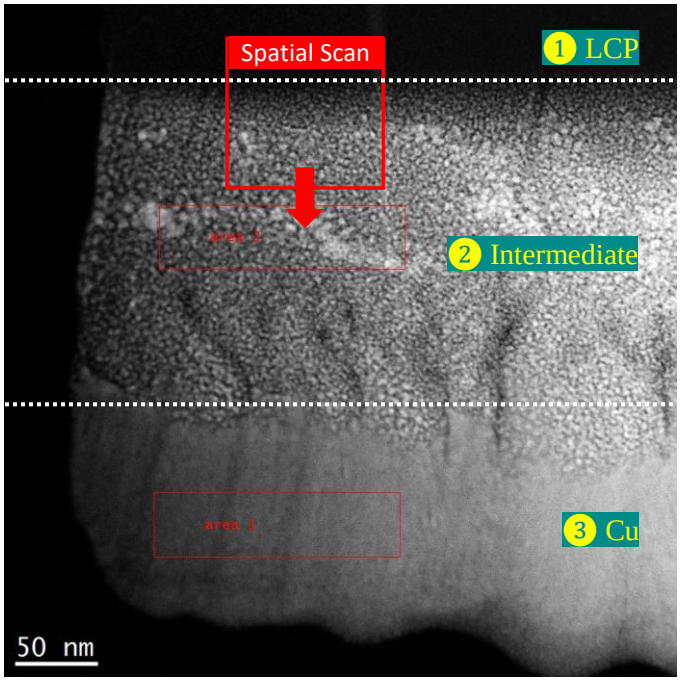

Figure 3-17. STEM HAADF cross-section image of Cu/LCP showing spatial scan window for elemental analysis.

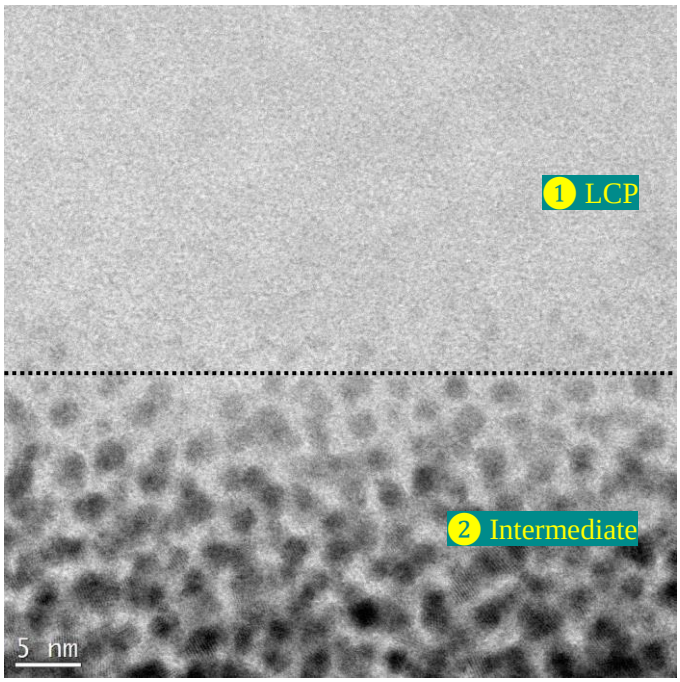

Figure 3-18. STEM BF magnified view of the LCP/intermediate layer showing grain boundary.

The quality of the smooth bonded interface can be observed in the low-magnification image of the specimen prepared for HRTEM analysis (Fig. 3-16). Higher magnification of the interface shows that Cu atoms form three-dimensional metal clusters and islands at the intermediate layer of the Cu/LCP interface (Fig. 3-17). As Fig. 3-18 shows, these islands penetrate the LCP forming a gradually fading grain boundary due to diffusion actuated by heat and plasma-induced compressive stress. This behavior is identical to the epitaxial growth of metal film on crystalline surface – a mechanism known as the Volmer-Weber growth mode [108]. In the Volmer-Weber mode, metal films nucleate as discrete islands with different crystallographic orientations (or no crystallinity at all in the case of amorphous solids). These islands then gradually form a continuous film [109].

The quantitative analysis of the elemental distribution of Cu, C, Pt (Pt is the material used as protection layer during FIB lamella deposition and its presence is due to accidental re-deposition effects), and O atoms across the interface reveals some interesting phenomena. The EDS spatial scan analysis with results shown in Fig. 3-19 was performed from LCP side (1) to intermediate layer (2), and it shows almost constant Cu counts in LCP up to the interface after which Cu count increases rapidly in the intermediate layer. This suggests diffusion of Cu into LCP via the intermediate layer. Gradual increase of Cu atoms from intermediate layer (44.1%) to Cu side (82.5%) is confirmed from Figs. 3-20 and 3-21. Furthermore, Fig. 3-19 shows that the intensities of C and O atoms remain constant in both regions (1) and (2). This behavior may be due to the carbon diffusion from bulk LCP towards Cu surface and the thermal reconstruction of oxide layer that forms a homogenous distribution upon annealing. Again, diffusion gradient causes a gradual decrease of C atoms

from intermediate layer (49.3%) to Cu side (16.4%) as confirmed from Figs. 3-20 and 3-21.

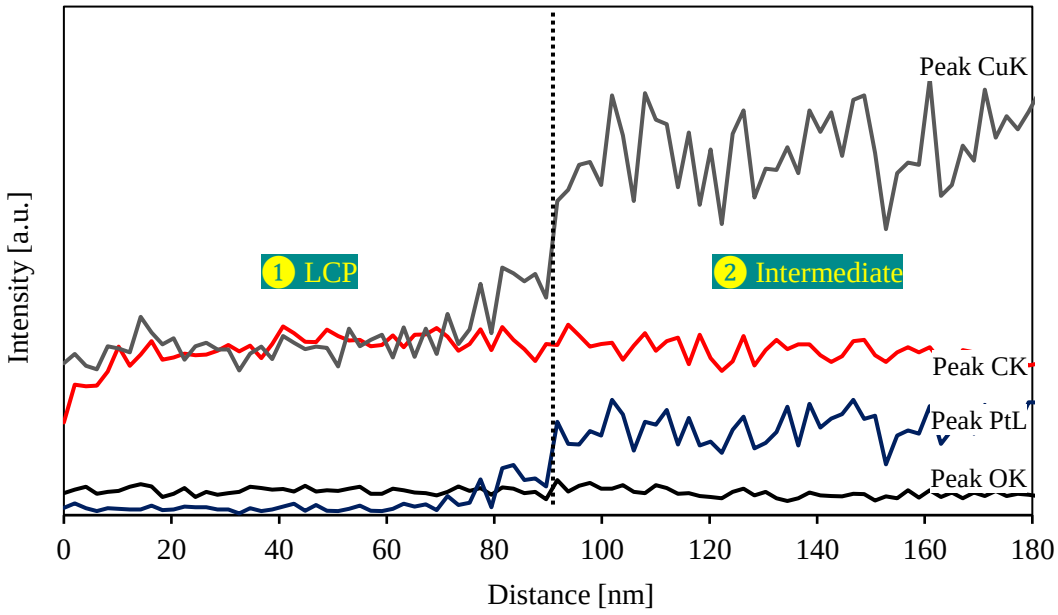

Figure 3-19. EDS line scan profile of element distribution across LCP/Intermediate interface.

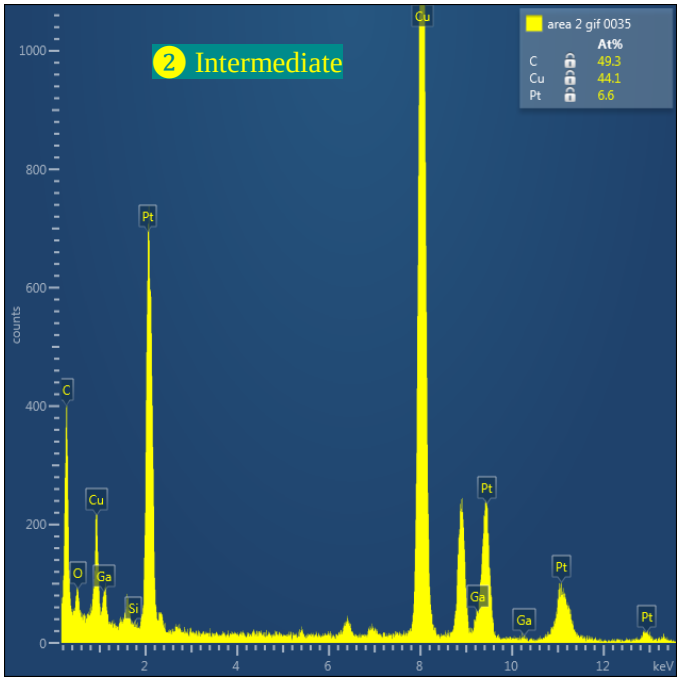

Figure 3-20. EDS profile of elements in intermediate layer.

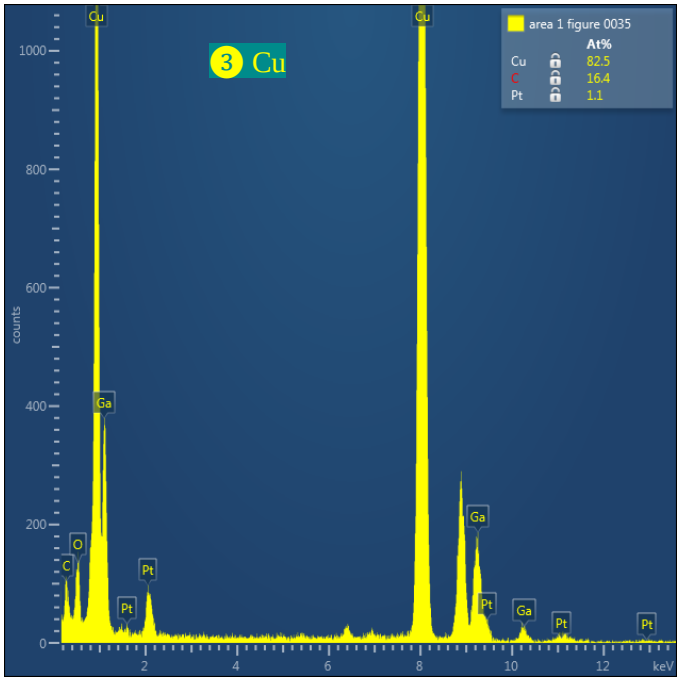

Figure 3-21. EDS profile of elements in Cu side.

Scanning electron micrographs of Fig. 3-22 complete the final picture. We observed growth of Cu_2O nanoparticles on an isolated (not contacted with LCP) plasma- and heat-treated Cu foil. It is possible that when activated Cu and LCP are contacted and heated under mechanical pressure, these thermally grown nanoparticles fill up the microgaps of the electrode-substrate interface and diffuse into LCP [107]. This results in the grain boundary of Fig. 3-18. The elemental interdiffusion gradients of Fig. 3-19 to Fig. 3-21 are also in good agreement with the possibility of nanoparticles diffusion into LCP. The surface roughness of Cu surface with nanoparticles is measured to be 3.08 nm (Fig. 3-23), which is less than that of pristine Cu (8.91 nm). This reduction in surface roughness is also advantageous for Cu/LCP bonding because surface activated bonding requires smooth mating surfaces [79].

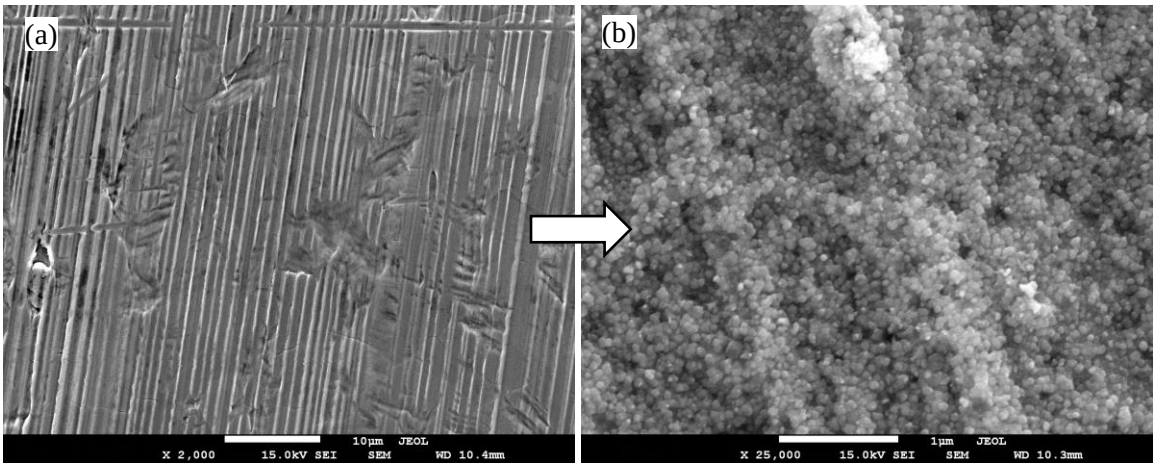

Figure 3-22. Scanning electron micrographs show the surface morphology of: (a) as-received Cu foil, and (b) activated Cu foil with thermally grown Cu_2O nanoparticles.

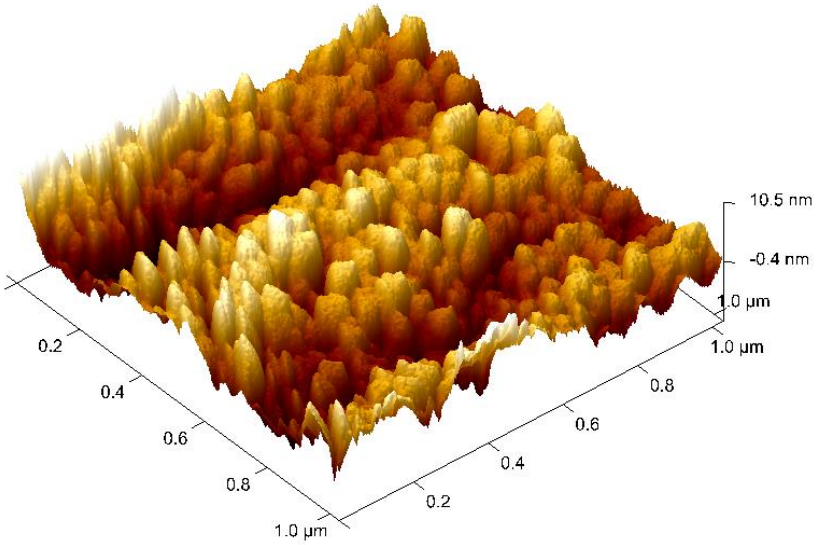

Figure 3-23. Surface topography of isolated Cu foil activated-and-heated without contact to LCP.

3.4.5 Summary of Cu/LCP bonding mechanism

Based on the results discussed above, we can summarize the bonding mechanism of Cu/LCP sensor base by SAB. O_2-RIE plasma cleans native oxides of CuO from Cu and hydrocarbons from LCP. Plasma cleaning creates dangling sites on Cu and LCP where new OH^- groups are formed. This makes the activated surfaces highly hydrophilic. Plasma modification produces Cu_2O bonds on Cu side and highly reactive O−C=O and C=O bonds on LCP side. When the plasma-treated surfaces are contacted, a weak hydrogen bond is formed initially between the OH^- groups. Thermal treatment under mechanical contact pressure dehydrates the Cu/LCP interface followed by condensation of OH^- chains. This forms an intermediate oxide layer together with diffusion of Cu_2O nanoparticles into LCP forming dominant bonding sites of Cu−O−C.

Figure 3-24. Illustration of surface activated bonding of Cu/LCP by comparing between: (a) as-received Cu and LCP, (b) activated Cu and LCP, and (c) contacted and heated Cu and LCP.

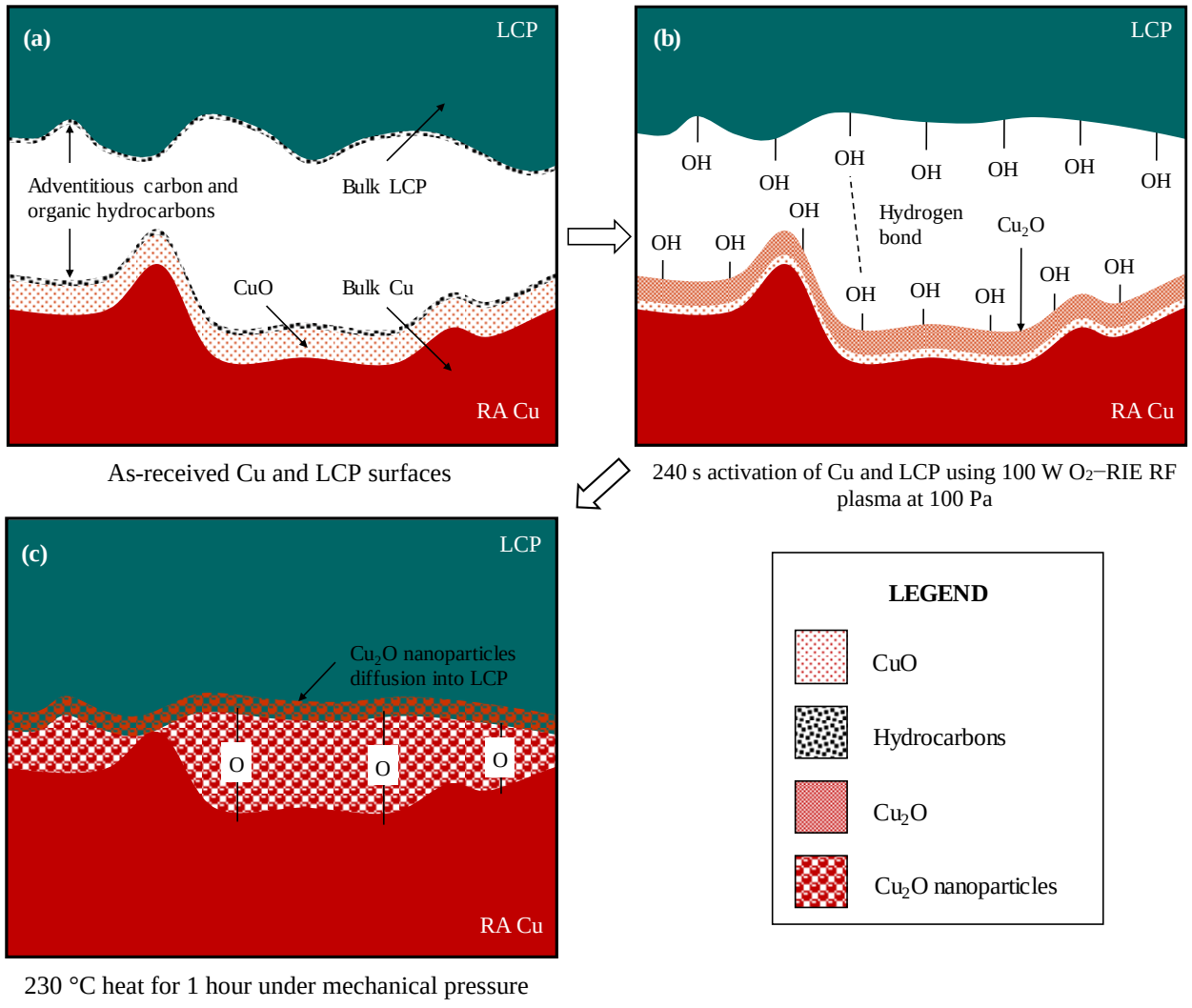

Chapter 4

Sensor performance

In this chapter, we investigate the performance of fabricated Cu/polymer-based Pb sensors. We discuss the feasibility and limitations of all-Cu-based electrodes in terms of potential window, stability, and other factors that enable quantitative detection of sub-ppb level Pb^{2+} ions in water. This is followed by an outline of the reagents, sample preparation, and experimental setup for this work. Optimization of the voltammetric sensing parameters is also discussed. Sensing performed with these optimized parameters enabled 30 s rapid detection of 0.2 μg/L Pb using only a 100 μL sample.

In terms of performance, we report on the Cu-based electrodes' response over a sufficiently long interval suited for a disposable, point-of-care application. The response of the 2 types of Cu/polymer-based sensors described in Chapter 3, with same electrode dimensions, are collected and calibrated from samples containing different concentrations of Pb. We also investigated the interfering effects from other metal ions like Cd and Zn that coexist in surface water with Pb. Our results show that the fabricated sensor can be used for trace Pb detection even in the presence of interfering ions.

4.1 Reagents

Electrochemical sensing of Pb is based on a redox process that requires a supporting electrolyte, such as the one we used in this work (0.2 M sodium acetate buffer, pH 5.2). The buffer was deoxygenated by nitrogen bubbling for 120 s to eliminate the effects of dissolved oxygen on Pb sensing peaks. Stock solution containing 10 mM Pb was prepared by dissolving 828 mg lead (II) nitrate (MilliporeSigma, Prod. ID 228621) in 250 mL DI water. The stock solution (or nearest lower concentration) was then diluted with deoxygenated acetate buffer in 1:9 v/v ratio. For example, 1 mL of 1 mM Pb solution was mixed with 9 mL acetate buffer to obtain 100 μM Pb. Solutions containing 10 μM, 1 μM, 100 nM, 10 nM, and 1 nM Pb concentrations were prepared for sensor calibration. Additionally, the interference effects of Cd and Zn were investigated because they commonly co-exist with Pb in surface water [36]. For this, cadmium nitrate (MilliporeSigma, Prod. ID 642045) and zinc nitrate (MilliporeSigma, Prod. ID 228737) were used.

4.2 Feasibility of all-Cu-based electrodes

4.2.1 Cu working electrode

The feasibility of Cu WE is determined by whether it can provide a potential range within which Pb oxidation during anodic stripping voltammetry can be registered as a current peak. The idea here is to make use of the zero-current response of WE in a blank solution (no Pb) at these potentials. This current response serves as the baseline on which

the Pb oxidation peak can be *superimposed* and quantified. We identified this potential window by performing cyclic voltammetry (CV) of Cu WE in blank acetate buffer electrolyte. CV scan rate was 100 mV/s and commercial Ag/AgCl RE and Pt AE were used. In cyclic voltammetry, the potential of the WE is ramped linearly versus time. After the set potential is reached, the WE potential is ramped back to the initial potential in the opposite direction. This way it is possible to control the redox behavior of a species that is adsorbed onto the electrode. The Pb oxidation peak is characteristic to a stripping potential that is contained within this potential window, hence the use of Cu WE is justified.

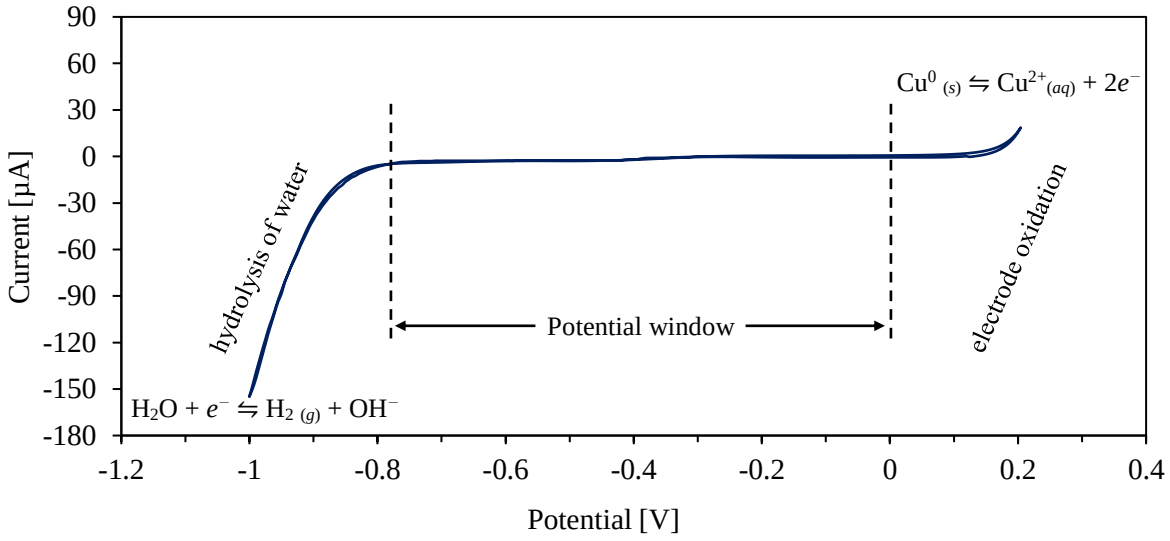

Figure 4-1. Cyclic voltammogram of fabricated Cu WE in blank acetate buffer with Ag/AgCl RE and Pt AE. Scan rate was 100 mV/s.

As shown in Fig. 4-1, Cu WE offers a potential window from −0.8 V to 0 V. At potentials more negative than −0.8 V, water hydrolysis (see Section 2.2.4) produces bubbles of hydrogen gas on the Cu WE that: (a) disrupt the flow of electrons between the AE and

the WE, (b) cause high resistance of the solution and loss of potential control of the WE, and (c) degrade the WE. At potentials more positive than 0 V, Cu WE turns black and loses sensitivity due to heavy oxidation.

4.2.2 Cu auxiliary electrode

For auxiliary electrode, an inert material like Pt is usually preferred. During a redox reaction, the AE sustains the current with the WE and completes the circuit [47]. To sustain this cell current during voltammetry, the potential of the AE changes according to our discussion in Section 2.1.4. However, this change is undesirable as it results in unstable electrochemical cell conditions. For this reason, AEs are made of highly polarizable[2] material like Pt. This prevents potential drifts when current passes between AE and WE. Cu on the other hand is non-polarizable[3] and is easily oxidized, which results in potential drift. However, Kang (2017) [36] have demonstrated that Cu AE can maintain a stable potential long enough (up to an hour for Cu electrodes thicker than 1 μm). We used thick-foil (> 10 μm) Cu electrodes for fabricating the sensors, so the cell stability should not be a major concern. It has been reported that coating the AE with a more polarizable material like palladium (Pd) may enhance electrode stability [36].

[2] A perfectly polarizable electrode is one where no actual charge crosses the electrode-electrolyte interface when a current is applied. Charge simply accumulates on electrode surfaces like a capacitor with no ion exchange.

[3] A non-polarizable electrode is one where current flow freely, but the electrode potential does not change from equilibrium potential upon application of current. This is because the electrode reaction is extremely fast (has an almost infinite exchange current density). The electrode-electrolyte interface behaves like a resistor.

4.2.2 $Cu/CuCl_2$ reference electrode

The miniaturization efforts of high-performance electrochemical sensors become limited mostly due to integration challenges of a stable reference microelectrode. One of the major design requirements for RE is that it should have a high exchange current density to minimize potential drift over time [110]. In conventional macroscopic REs such as the Ag/AgCl, this is achieved by chlorinating the surface of the underlying Ag electrode followed by immersing it in a concentrated Cl^- ion rich solution enclosed in a glass tube with a membrane interface. The idea here is that the saturated filling solution prevents buildup of net dipoles (i.e. dipoles that result in a non-zero net dipole moment) at the electrode-electrolyte interface by preventing sudden concentration changes near the electrode when the external test solution is introduced. This guards against changes in electrode surface potential.

The $Cu/CuCl_2$ RE of the fabricated sensor is often termed as a "quasi"-reference electrode as it does not have a filling solution and is in direct contact with the test electrolyte. These two features cause potential drift over longer periods of time, which is why quasi-REs have become more popular for disposable sensors where the experiment time is lower than the intended lifetime of the electrode [110]. We investigated the feasibility of $Cu/CuCl_2$ quasi-RE by measuring its open-circuit potential with respect to a commercial Ag/AgCl RE over 20 minutes.

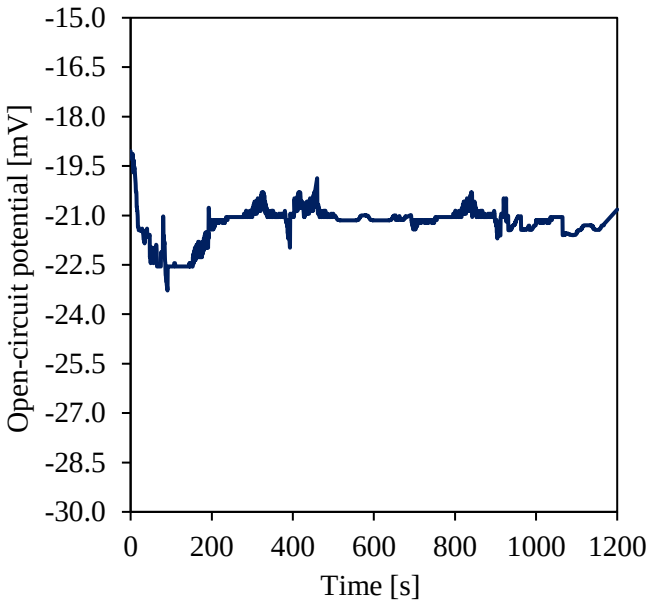

Figure 4-2. Open-circuit potential response of fabricated $Cu/CuCl_2$ RE measured against a commercial Ag/AgCl RE in acetate buffer.

As Fig. 4-2 shows, the potential response of $Cu/CuCl_2$ remains stable over the 1200 s with a potential drift of < 5 mV. This is adequate for a disposable sensor and are not bad when compared to the ease of fabrication. Apart from the considerations discussed so far, potential drifts may also arise from convective mixing of the solution [110]. However, this does not apply to our fabricated sensor because in our design sensing is performed in an undisturbed, sealed PDMS well with only 100 μL sample. The small noise variation in open circuit potential is likely due to slow dissolution of $CuCl_2$ in buffer, as is also the case with commercial Ag/AgCl electrodes [110].

As reported in the literature, the most notable challenge faced during RE miniaturization is the rapid dissolution of small electrode volumes (such as Ag and AgCl) which leads to shorter lifetimes [110]. Thinner electrodes get depleted faster thus the

underlying support metals (e.g. titanium or chromium adhesive layer) and terminals get exposed, creating mixed potential response (interference). We have overcome this challenge by replacing thin-film electrodes with thick foil electrodes. We have also eliminated the use of any metallic underlayer by directly bonding Cu electrodes to the polymer substrate, thus reducing possible potential shift arising from metallic underlayers.

4.3 Deoxygenation and sensor sealing

Once we fabricated the sensors, we initially performed cyclic voltammetry using our Cu-based sensors in as-received (diluted to 0.2 M) acetate buffer containing 1 mM Pb. CV analysis is required prior to sensing parameters optimization because it identifies the Pb oxidation peak position. More on peak positions and sensing parameters will be detailed in Section 4.4. Primary analysis results in Fig. 4-3 showed that this peak was located between −400 mV to −500 mV. We wanted to further check the reproducibility of the cyclic voltammogram after performing 20 sensing cycles at 1 min interval. Therefore, we repeated the CV analysis after 20 minutes and observed secondary peaks both during the forward and reverse CV cycles. This was interesting because we did not introduce any foreign ions into the sensor and yet obtained these peaks. Fig. 4-4 shows that the secondary peak forms gradually after each sensing cycles. We also observed a slight shift of the peak potential to a more positive value. This may indicate that the additional peak introduction was due to rapid dissolution of $CuCl_2$ from the RE under the corrosive influence of dissolved oxygen in buffer. The degradation of RE releases Cl^- ions in buffer that may be responsible for this change, although the oxidation of Cu electrode to CuO is another possibility. To confirm if

dissolved oxygen or sensor exposure to air was responsible, we deoxygenated the buffer by nitrogen bubbling for 120 s. We then repeated the same experiment with deoxygenated buffer containing 1 mM Pb, but this time we sealed the sensor with a glass slide after introducing the test solution. The disappearance of the secondary peak in Fig. 4-5 confirms that the peak broadening was indeed due to oxidative corrosion of electrodes and can be avoided by using deoxygenated buffer and sealed sensor.

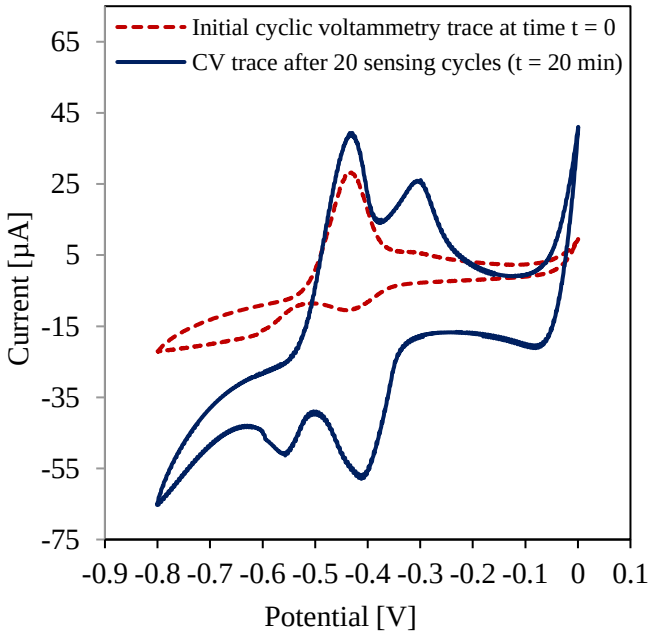

Figure 4-3. Cyclic voltammetry of all Cu-based sensor in 0.2 M, pH 5.2 acetate buffer with 10 μM Pb. CV was performed at t = 0 and at t = 20 min. Scan rate was 100 mV/s.

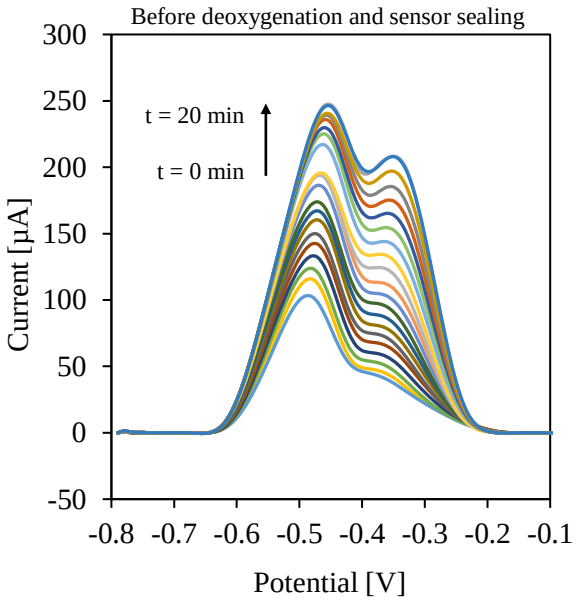

Figure 4-4. Anodic stripping voltammetry of all Cu-based sensor in 0.2 M, pH 5.2 acetate buffer with 1 mM Pb. ASV was performed every 1 minute for 20 sensing cycles.

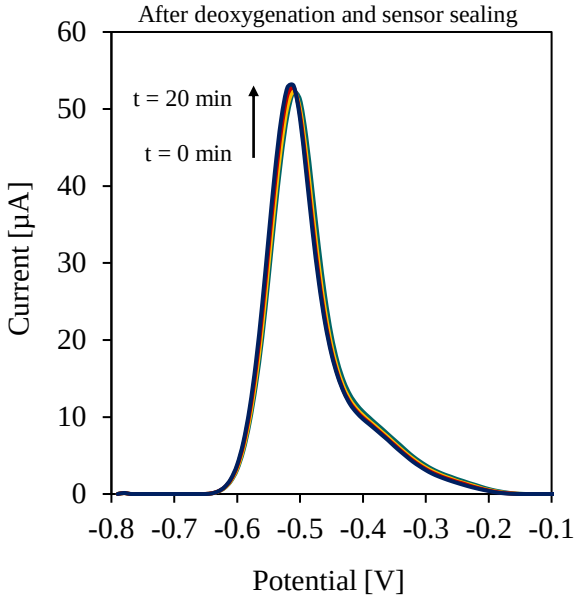

Figure 4-5. Repetition of anodic stripping voltammetry using deoxygenated acetate buffer and a sealed sensor.

4.4 Electrochemical sensing of Pb

4.4.1 Experimental setup

A miniature USB powered potentiostat (EmStat3, PalmSens) with PSTrace data analyzer software was used in electrochemical experiments. In each experiment, the EmStat3 was probed to a fresh sensor. A 100 μL sample was placed in the PDMS-well. This electrolytic chamber was then covered with a 22×22 mm^2 glass slide to prevent oxidation of the electrode and sample during voltammetry, as discussed. Cyclic voltammetry was initially repeated 3 times in acetate buffer (0.2 M, pH 5.2) with 1 mM Pb to determine the oxidation and reduction peak positions of Pb. CV scan rate was 100 mV/s and CV potential sweep range was −0.8 V to 0 V. Square wave anodic stripping voltammetry is popular for fast detection of analyte and was used to record current peaks corresponding to different concentrations of Pb in buffer. These data were used to calibrate the sensor. For stripping voltammetry, a −0.6 V deposition potential was first applied on the Cu WE for 10 s to reduce Pb^{2+} ions to Pb^0. The electrodeposited Pb atoms were then stripped from the surface of the Cu WE by sweeping the electrode potential from −0.8 V to −0.2 V. The optimized SW-ASV settings were 10 mV, 100 mV, and 10 Hz for step potential (increment), pulse amplitude (half peak-to-peak value) and frequency, respectively, as will be detailed in the next section. All optimization experiments were repeated 10 times using a fresh Type 2 (Cu/PI) sensor each time for each Pb concentration. Finally, both Type 1 (Cu/LCP) and Type 2 (Cu/PI) sensors were calibrated using the averaged ASV peak currents for 1 nM−10 μM Pb.

4.4.2 Optimization of sensing parameters

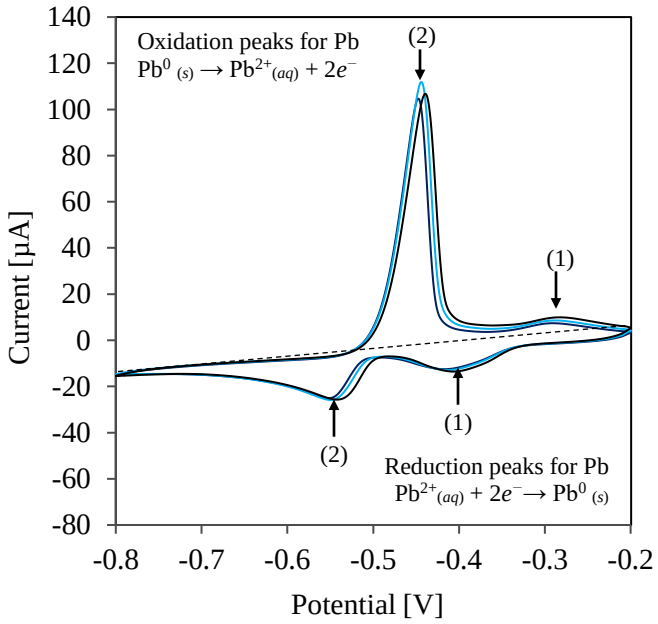

Figure 4-6. CV in 0.2 M, pH 5.2 acetate buffer with 1 mM Pb. Scan rate = 100 mV/s.

Fig. 4-6 shows the cyclic voltammogram of 1 mM Pb in acetate buffer (0.2 M, pH 5.2). CV results show two sets of peaks for both Pb deposition (reduction of Pb^{2+} to Pb^0) and Pb stripping (oxidation of Pb^0 to Pb^{2+}). In both cases, the double peaks occur because of high concentration of Pb [36] and not due to dissolved oxygen (since deoxygenated sample and sealed sensor were used). For lower concentrations of Pb, only a single peak appears as we will see next. The smaller peaks (1) are due to a thin layer of Pb atoms directly deposited on the surface of the Cu WE. The larger peaks (2) are due to further deposition of Pb on the already present Pb layer instead of the Cu electrode. Therefore, the peak at −413 mV (−8.7 μA) corresponds to Pb deposition on Cu electrode followed by

thickening of deposition layer at −552 mV (−17.7 μA). During oxidation, the thick layer of Pb first depletes at −447 mV (103.7 μA) and finally at −270 mV (8.9 μA) where Pb atoms are removed from the electrode. The described process is similar to the first-in last-out (FILO) model. After identifying the peak positions from CV, we optimized the SW-ASV parameters (deposition potential, time, and stripping waveform settings) to obtain a good tradeoff between low signal variation, rapid detection, and peak current.

Deposition potential is one of the important parameters for ASV and its value is often selected at 300−500 mV more negative than the standard reduction potential E^0 of the metal to be reduced (E^0 for $Pb^{2+} + 2e^- \leftrightharpoons Pb_{(s)}$ is −0.126 V versus a SHE) [11]. To understand this selection, we need to appreciate the Nernst equation [11] that relates the concentration of the Pb^{2+}/Pb^0 redox couple on the working electrode (surface concentration, $[Pb^{2+}]_{electrode}$) and the applied potential, E:

$$E = E^0_{Pb^{2+}/Pb} - \frac{0.05916}{2} log \frac{1}{[Pb^{2+}]_{electrode}} \tag{4.1}$$

If we choose a quantitative reduction of 99.99% Pb^{2+} to Pb^0, then the surface concentration of Pb^{2+} is related to the known bulk concentration of Pb^{2+} in buffer, $[Pb^{2+}]_{bulk}$, by:

$$[Pb^{2+}]_{electrode} = 0.0001 \times [Pb^{2+}]_{bulk} \tag{4.2}$$

Rewriting Equations 4.1 and 4.2, the minimum potential required for quantitatively reducing 1 nM Pb^{2+} to Pb^0 can be calculated:

$$E = -0.126 - \frac{0.05916}{2} log \frac{1}{0.0001 \times (1 \times 10^{-9})} = -0.51\ V \quad (4.3)$$

To experimentally optimize the deposition potential used in this work, we tested different values from −0.4 V to −1.5 V and recorded the ASV peak currents corresponding to 10 μM Pb in buffer (Fig. 4-7). From −0.4 V to −0.6 V, the peak current was almost unchanged, however variation (indicated by error bars on the graph) was lowest (9%) at −0.6 V. The current peaks were higher at −0.7 V and at −0.8 V but also had a 14%−20% coefficient of variation. The variation was even larger (39%) at −1.5 V although the peak current was higher. This steep change in current is due to the hydrolysis of water by $H_2O + e^- \leftrightharpoons H_2\ (g) + OH^-$ as discussed. The signal variation became higher because ASV in the presence of trapped hydrogen bubbles produces noise as discussed in Section 2.2.4 (electrode layout design considerations). We therefore settled for −0.6 V as the optimized potential with lowest variation coefficient.

Another explored ASV parameter is the deposition time. Longer deposition (up to 15−30 min) usually yields stronger peak current and is recommended for sensing low concentrations of analyte [11]. However, thick RA foil electrodes could provide strong peak current even with short deposition. As results in Fig. 4-8 show, peak current increases with deposition time from 10−50 s with <8% variation. In the tradeoff between faster process and lower LOD, we settled for 10 s deposition which resulted in a 260 nA peak current for 1 nM Pb in 0.2 M buffer. It should be noted that a thick-foil electrode such as the one fabricated in this work can support deposition time longer than 10 min, if desired, which is not often possible with thin-film electrode due to oxidation and delamination issues.

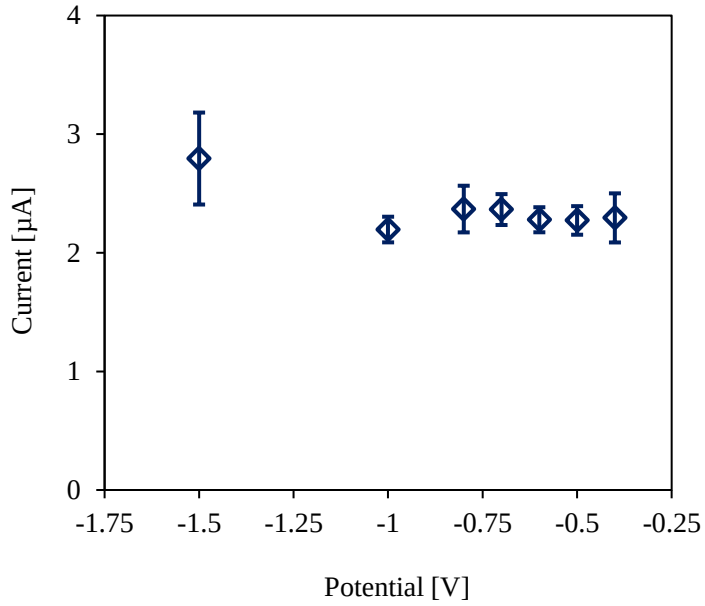

Figure 4-7. Optimization of deposition potential to −0.6 V for ASV of fabricated sensor in acetate buffer containing 10 μM Pb.

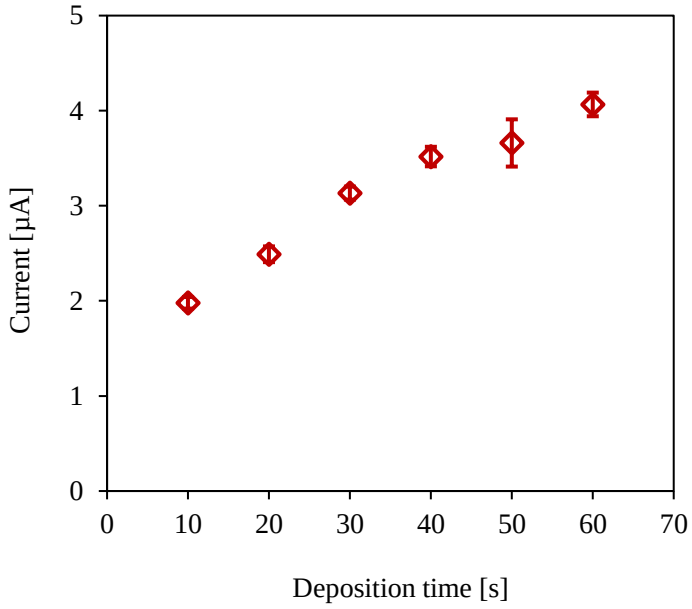

Figure 4-8. Optimization of deposition time to 10 s for ASV with 10 μM Pb. Shortest time was chosen for rapid response over peak current.

The SW-ASV waveform parameters were also optimized. The peak current increases at higher square wave frequency and amplitude (Figs. 4-9 and 4-10). Higher pulse-frequency produces a higher signal variation, although the variation was insignificant for pulse-amplitude below 100 mV. For the pulse-increment, 10 mV step potential was used (Fig. 4-11). These optimized values were then used in Pb ASV for calibration of the sensors:

Table 4-1. Optimized SW-ASV parameters for Pb sensor.

Parameter	Value
Deposition potential (V)	−0.6
Deposition time (s)	10
Pulse frequency (Hz)	10
Amplitude (mV)	100
Increment (mV)	10

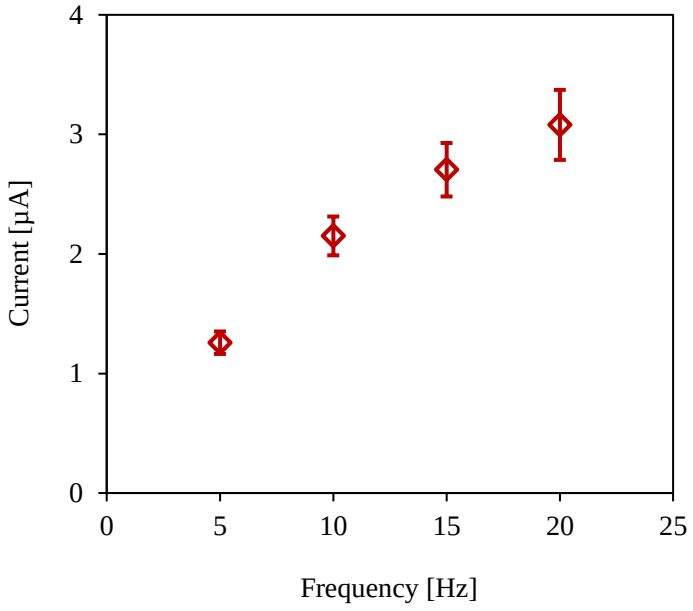

Figure 4-9. Optimization of square wave frequency to 10 Hz for ASV with 10 μM Pb.

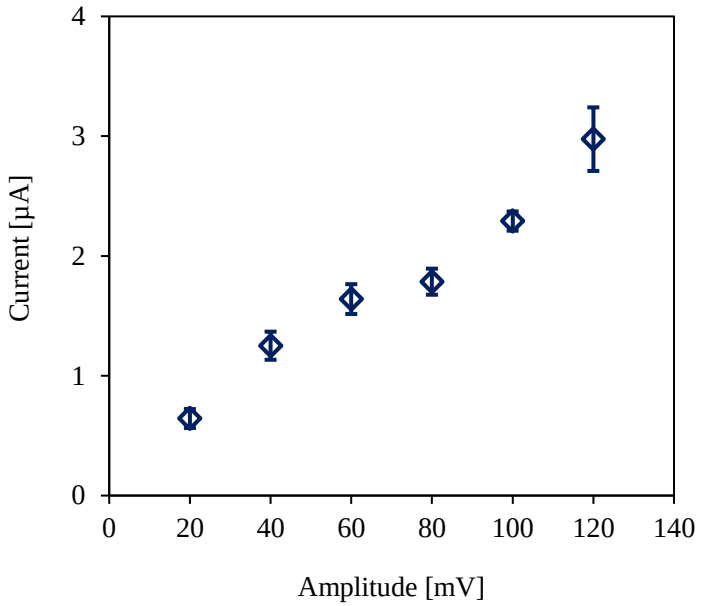

Figure 4-10. Optimization of square wave amplitude to 100 mV for ASV with 10 μM Pb. A tradeoff between low coefficient of variation and peak current was established.

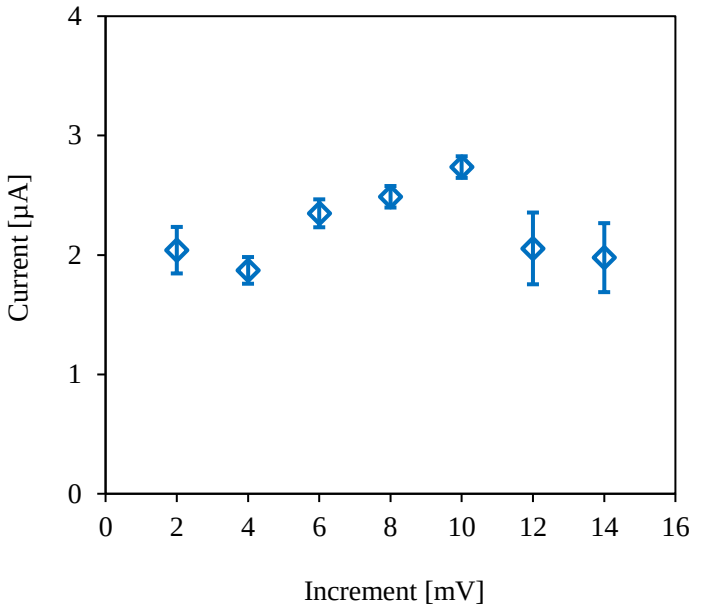

Figure 4-11. Optimization of pulse increment to 10 mV for ASV with 10 μM. This value produced the maximum peak current.

4.4.3 Anodic stripping voltammetry for Pb detection

Fig. 4-12 shows the stripping peak profile of Pb in deoxygenated acetate buffer split into concentration ranges of 10 μM − 1 μM and 1 μM − 1 nM (for better viewing). The ASV of 1 nM − 10 μM Pb produced single stripping peaks whereas Pb concentrations greater than 10 μM produced double peaks. As discussed in Section 4.4.2, ASV of high concentration of Pb registers a second current peak due to initial stripping of Pb atoms from the surface of underlying Pb layer followed by stripping from the electrode surface. The ASV peak amplitudes in both low concentration and high concentration ranges increased linearly as observed in peak profile split views. This behavior is due to the mass transport characteristics of the system [11][36][110]. The mass transport can be related to convection, migration, and diffusion. Since the solution is not mechanically stirred within the PDMS-well, convection does not occur and does not affect the formation of a diffusion layer on the working electrode. Also, the effect of migration is eliminated by introducing high concentration of excess of acetate buffer that acts as an inert electrolyte. Therefore, diffusion is the significant form of mass transport for this integrated three-electrode system. Fig. 4-12 also shows the potential stability of $Cu/CuCl_2$ RE, with the current peaks for Pb oxidation repeating at ca. ─400 mV throughout the experiments.

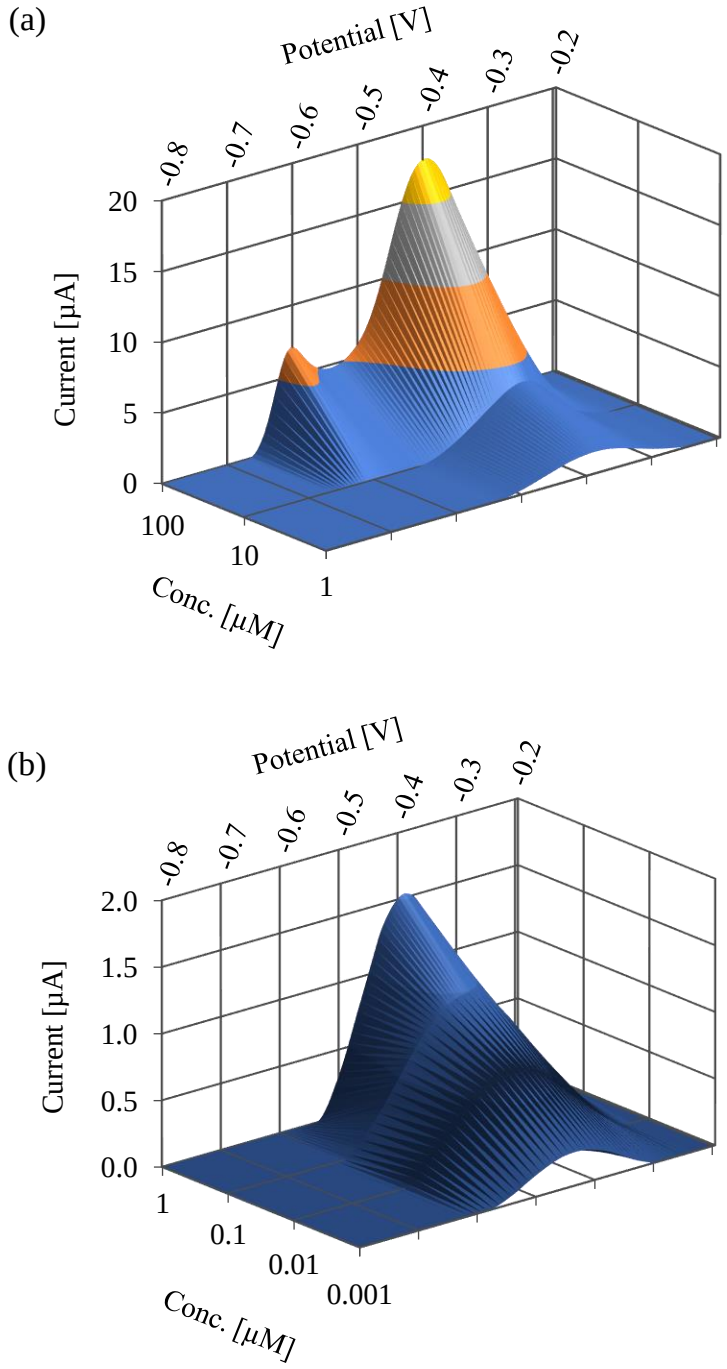

Figure 4-12. ASV peak profile with Type 2 sensors split as: (a) 100 μM − 1 μM Pb, and (b) 1 μM – 1 nM Pb in deoxygenated acetate buffer. Data presented as mean of 10 replicates.

4.4.4 Sensor performance

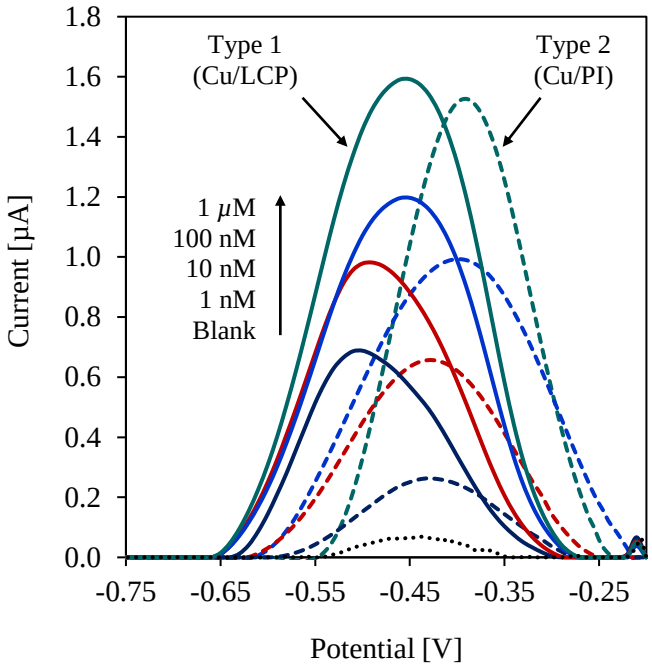

Figure 4-13. ASV of 1 nM − 1 μM Pb using Type 1 (directly-bonded Cu/LCP) and Type 2 (Cu/PI laminate) sensors. Data presented as mean of 10 replicates.

Fig. 4-13 shows the ASV stripping peaks of varying Pb concentrations recorded with both Type 1 (Cu/LCP) and Type 2 (Cu/PI) sensors. The difference in stripping peak potentials between the two types of sensors may be due to the difference in RE elemental composition. Type 1 sensor is based on bulk Cu foil directly bonded to LCP by a SAB process. Type 2 sensor (Cu/PI) is based on a proprietary specimen from Dupont that may contain an intermediate adhesive layer of metal (such as Ti) between Cu/PI. This results in a different half-cell potential than plain Cu/LCP. While further investigation is needed to

identify the underlayer in Cu/PI and understand how it affects the Pb oxidation peak potential, we leave it as a future work.

Our next observation was a slight shift of respective voltammogram sets of Type 1 and 2 sensors towards a more positive potential at higher Pb concentrations. This shift is reported for most electrochemical sensors and is due to the logarithmic dependence of electrochemical (electrode) potential on the analyte concentration [110]. Kang (2017) also investigated the pH dependency of the stripping peak potential and observed that the peak position varies linearly between pH 5 − 6.5 (more acidic pH shifts the peak potential to a more positive value [36]). This is because the electron-transfer (between WE and AE) during Pb redox reactions on the WE is facilitated by the oxidation of electrolyte itself on the AE that involves H^+ and OH^- ions. When H^+ ions get involved in the cell reaction, the cell potential also depends on the pH. Kang (2017) demonstrated that the pH change mostly affects the signal variation of the stripping peaks without changing the peak amplitude. This is significant for our sensors because our test environment is a solution with pH 5.2, whereas drinking water is limited to pH 6.2–8.2. We used pH 5.2 because that is the pH of the acetate buffer that we used, and we did not wish to add variability to the calibration process by having to adjust the pH of the solution. The conclusions from Kang (2017) demonstrate that this is not expected to have significant impact on the peak amplitude and therefore does not affect the conclusions we make in this thesis regarding our sensor performance. Any shift in the peak potential can be accounted for during sensor calibration. For a disposable sensor, this trade-off should not be much of a concern comparing to the fabrication ease and cost.

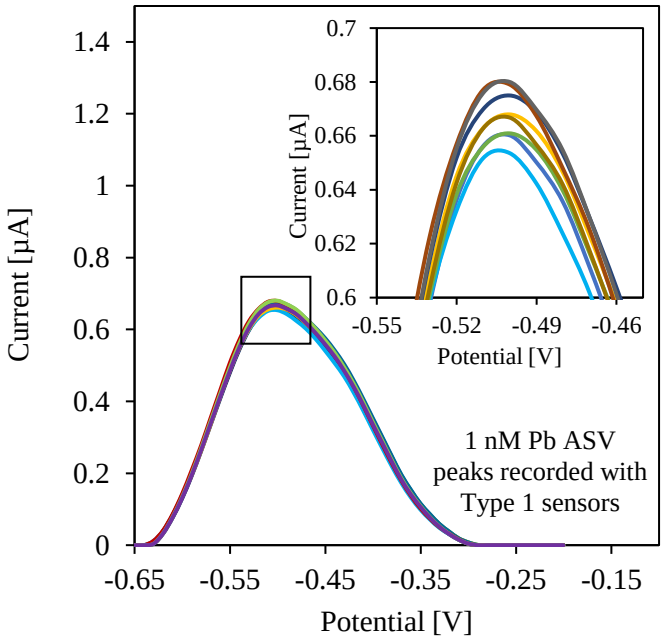

Figure 4-14. ASV dataset for 1 nM Pb detected by a Type 1 sensor. Inset shows magnified peaks.

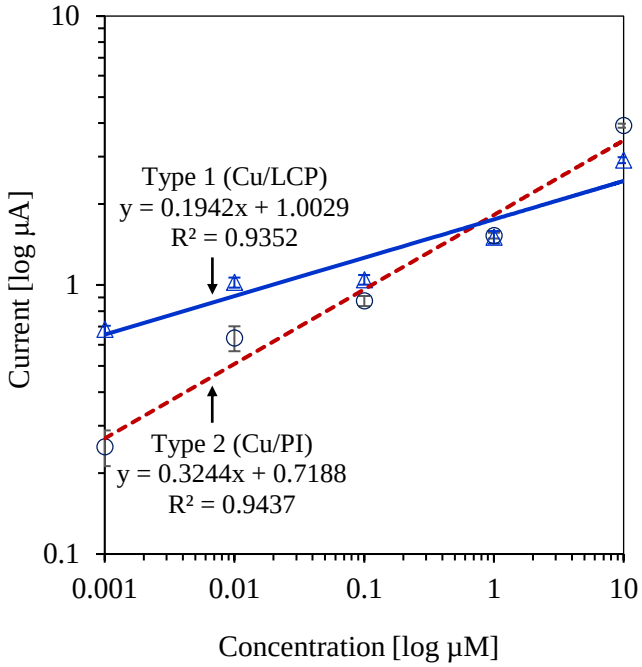

Figure 4-15. Calibration of Type 1 and Type 2 sensors. Standard deviation obtained for n = 3 (Type 1) and n = 10 (Type 2).

Fig. 4-14 shows the ASV datasets of the smallest detectable Pb concentration (1 nM) using Type 1 sensors, and the inset shows the variation of the peaks. For each Pb concentration we conducted multiple measurements, each time using a fresh sensor. Figure 4-14 demonstrates the excellent repeatability of results using multiple sensors, hence allowing us to use these data sets for calibration. The error bars shown on the calibration curves were calculated from the variations in these data sets. The average peak current (678 nA) was about 2.6 times more than the stripping current (260 nA) registered for 1 nM Pb by Type 2 sensors. The stronger current registered by Type 1 sensors is due to thicker electrodes compared to that of Type 2 sensors. The extra thickness gives Type 1 electrodes a higher effective surface area than Type 2 electrodes, which then provides a higher peak current.

Finally, Type 1 and 2 sensors were calibrated from the peak currents of Fig. 4-13. Type 1 and 2 sensors demonstrated a sensitivity (slope) of 0.194 μA/μM and 0.324 μA/μM respectively (Fig. 4-15). If a higher peak current (higher sensitivity) is desired, longer deposition time can be used (see Fig. 4-8). The correlation equations between peak current $I(\mu A)$ and Pb concentration $[Pb(\mu M)]$ were identified as $I(\mu A) = 0.1942 \times [Pb(\mu M)] + 1.003$ with $R^2 = 0.935$ for Type 1 sensors, and $I(\mu A) = 0.3244 \times [Pb(\mu M)] + 0.7188$ with $R^2 = 0.944$ for Type 2 sensors. R-squared (R^2) is a statistical measure of how close the data are to the fitted regression line and signifies linearity of the system. Usually a high linearity ($R^2 \rightarrow 0.99$) is desired for any sensor so that the sensitivity and resolution do not vary with a change in input (analyte concentration). Both Type 1 and 2 sensors exhibit good linearity considering the sample distribution across the wide concentration range.

Quantitatively the calibration curve results in a measurement accuracy to within a factor of 2 over the range of concentrations of interest. This is sufficient for most applications (e.g. at the lowest concentration of 0.2 ppb the measurement would indicate an actual concentration between 0.1 and 0.4 ppb). Within this error margin, visual evaluation [111] yields an LOD of 0.2 μg/L for both Type 1 and 2 sensors.

4.4.5 Performance comparison

Table 4-2 compares this work with other Pb sensors reported in the literature. Chen (2014) and Ouyang (2011) reported the lowest LODs of 0.05 μg/L [27] and 0.12 ng/L [37] respectively. Chen (2014) showed that the performance of a GCE can be enhanced by modifying the electrode with overoxidized polypyrrole (OPPy) tethered with 2-mercaptoethanesulfonate (MES), Nafion, and Bi. The polypyrrole is a conductive polymer that increases the conductivity, electrochromic property, redox reversibility, and stability of the electrode in aqueous solution [27]. MES is used to functionalize the polypyrrole so that the electrode can readily react with Pb^{2+} ions. Since Bi electrodes have excellent stripping characteristics, a combination of Bi/Nafion/OPPy-MES offered excellent performance. Similarly, Ouyang (2011) showed that the synergistic effect of mercury (Hg) and Bi as well as the enlarged, activated surface and good electrical conductivity of SW-CNTs on GCE contribute to the enhanced activity of their electrode towards achieving a LOD of 0.12 ng/L Pb. A Hg-Bi coating on the GCE decreases the impedance of the electrode that favors the electron transfer during electrochemical assay of Pb^{2+}. CNTs on the electrode further enhance the electron transfer by providing a higher effective surface area and higher

conductivity. Compared with our approach, both these approaches involve the use of expensive materials and complex processing. Our sensor demonstrates the lowest LOD and shortest measurement time for an all Cu sensor. In addition, the use of Bi and Hg introduce additional problems in terms of disposal and contamination.

In terms of analysis time required for Pb determination, our work features rapid sensing (30 s) and a sub-parts-per-billion level detection limit for Pb ions. In the tradeoff between these two performance parameters, the use of rolled-annealed Cu foil electrodes (Fig. 4-16) offers the best combination. Conventionally, a higher deposition time is desirable when the sensor cannot provide enough peak current either due to low analyte concentration, small electrode surface area, or poor conductivity of the electrode [11]. To address these issues, deposition time, electrode material, and electrode geometry are carefully chosen. For example, using nanostructures such as single-wall carbon nanotubes (SW-CNT) [60] increases the effective surface area of the electrode, but at the price of greater fabrication complexity. Comparing electrodes with the same geometry, rolled-annealed Cu electrodes have better performance over electrodeposited or screen-printed electrodes. Merchant (2004) [50] characterized the cross-sections of rolled-annealed and electrodeposited Cu and identified differences in their grain boundaries. When annealed, rolled Cu foil underwent recovery and recrystallization forming compact columns of vertically aligned grains, whereas the grains in electrodeposited Cu were randomly oriented with weak crystallographic textures. This recrystallization is linked to increased electrical conductivity of RA Cu at higher annealing temperatures [112] and enables detection of small stripping currents from trace analyte, hence offering superior electrode performance.

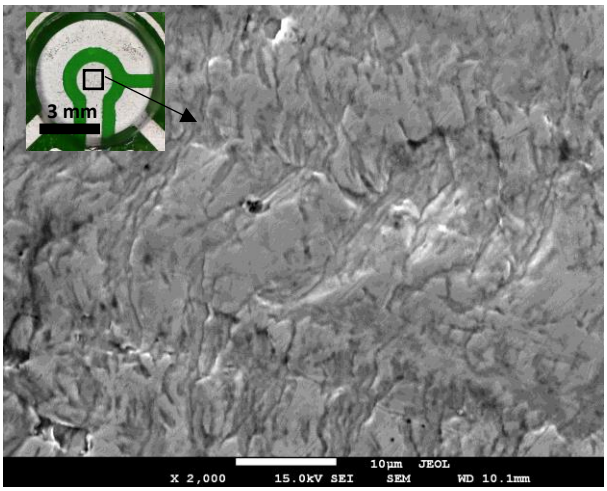

Figure 4-16. SEM micrograph showing the active surface of a rolled-annealed Cu-based WE. Inset shows the optical image of a fabricated sensor.

Table 4-2. Comparison of this work with similar electrochemical Pb sensors.

Electrode material			**Electrode fabrication**	**LOD (μg/L)**	**Deposition time (s)**	**Reference**
WE	**CE**	**RE**				
Cu	Cu	$Cu/CuCl_2$	LaserJet printing of electrode mask on Cu/polymer. Fully integrated 3-electrodes acting as an embedded electrolytic setup in a PDMS chamber.	0.2	10	This work.
Bi-TRGO/Au	Au	Ag/AgCl	Lithographic micro-patterning of TRGO/Si substrate followed by electrodeposition of Bismuth.	0.4	150	[24]
Bi-Nafion-graphene on GCE	Pt	Ag/AgCl	GCE Composite made by dispersion of graphene in Nafion solution and in-situ plating of Bi film.	0.5	120	[26]
Bi/Nafion/poly-pyrrole on GCE	Pt	SCE	Polymerization of pyrrole followed by thiol-ene overoxidation and Nafion coat.	0.05	300	[27]
Bi-C	Pt	Ag/AgCl	Screen printing & electrodeposition of bismuth coated carbon electrode.	0.3	120	[31]
Bi-nanopowder /nafion	Pt	SCE	Dispersion of gas-condensed bismuth nanopowder on carbon with Nafion.	0.17-1.97	180	[32]
Bi	Pt	SCE	Screen printing and electrochemical reduction of Bi_2O_3.	2.3	300	[33]
Bi/GCE	Pt	Ag/AgCl	In-situ deposition of bismuth on GCE.	0.8	120	[34]
Bi nano- hexagons on Cu	Pt	Ag/AgCl	Hexagon-shaped bismuth nano- and micro-architectures electrodeposited onto polycrystalline Cu	0.05	600	[35]

Cu	Cu	$Cu/CuCl_2$	Evaporation of Ti/Cu followed by mask photolithography and Cu etch.	4.4	300	[36]
Hg-Bi/SW-CNT on GCE	Pt	Ag/AgCl	SW-CNT functionalization of GCE by liquid drop followed by ex-situ chemical deposition of Hg and Bi.	0.12 ng/L	300	[37]
Sb-boron doped diamond	C	SCE	Electrochemical modification of antimony nanoparticles on boron-doped diamond electrode.	18.5	120	[41]
Boron doped diamond	Pt	Ag/AgCl	Synthesis of diamond films in a hot filament chemical vapor deposition reactor.	1	180	[42]
Au	C	Ag	Screen printing of Au and Ag.	0.5	120	[58]
Bi/graphene-ionic composite	Pt	Ag/AgCl	Electrochemical reduction of graphene oxide on an ionic liquid followed by in-situ bismuth deposition.	0.1	120	[59]
SWCNT	Pt	SCE	Vacuum filtering of SWCNT on an anodisc membrane followed by photolithographic processing.	0.8	150	[60]
Bi-CNT	Pt	SCE	In-situ bismuth plating on screen-printed CNT electrode.	1.3	300	[61]
Porous Bi	Pt	Ag/AgCl	Electrochemical deposition of bismuth into a polystyrene template.	1.3	90	[63]

4.5 Interference study

We investigated the interference effects of Cd and Zn on the Cu-based sensor because these ions often coexist with Pb in water and their ASV peaks are separated by only a few hundred millivolts [67]. Thus, these peaks may interfere with that of Pb. We compared between the ASV peaks of Pb alone and Pb mixed with Cd and Zn at high and low concentrations. As shown in Fig. 4-17, ASV of equally mixed concentrations (1 mM) of Pb, Cd, and Zn in 0.2 M, pH 5.2 acetate buffer registered two distinct peaks in contrast to a single sharp peak for 1 mM Pb alone. Although one would expect three distinct peaks for Pb, Cd, and Zn, the relative oxidation potential of Zn is more negative than that of Cd [36] and is therefore outside the potential window. Thus, Zn^{2+} is the least interfering ion in this study. This seems obvious since the optimized deposition potential (−0.6V) is not sufficiently negative to reduce (deposit) Zn on the WE in the first place [11].

The peak reduction of Pb for the mixture of 1 mM Pb, Cd, and Zn in Fig. 4-17 however indicates that Cd has some interference. The 1 mM Cd oxidation peak at −750 mV is much smaller compared to the 1 mM Pb oxidation peak at −500 mV, which could signify either one of two things: a) The Cu-WE has poor affinity towards Cd^{2+} ions, or b) The deposition potential used for Pb sensing causes partial deposition of Cd on the WE. Kang (2017) [36] observed similar fractional deposition on the working electrode and explained it in terms of under-potential deposition. Therefore, the interference effects in a Pb sensor may be minimized by careful optimization of the deposition potential.

Next, we repeated ASV of equally mixed low concentrations (1 nM) of Pb, Cd, and Zn and compared it with that of 1 nM Pb alone. As results in Fig. 4-18 show, we recorded ASV peak distortion in the presence of 1 nM interfering ions. The loss in signal amplitude and increased noise adversely affect the sensor LOD. However, Pb and Cd commonly exist in surface waters in the range of 5−30 μg/L and <1 μg/L respectively [36]. Based on this ratio, we expect that even Cd will have negligible interference on the Cu-based sensor for Pb determination. Before concluding this section, we further investigated the effect of varying Cd concentrations while maintaining a fixed Pb concentration. As results in Fig. 4-19 show, all Cd stripping peaks are registered separately and do not overlap with the Pb stripping peak. Inset of Fig. 4-19 shows the isolated Cd stripping peaks. This proves that the fabricated Cu-based sensor can accurately detect Pb even in the presence of Cd and Zn.

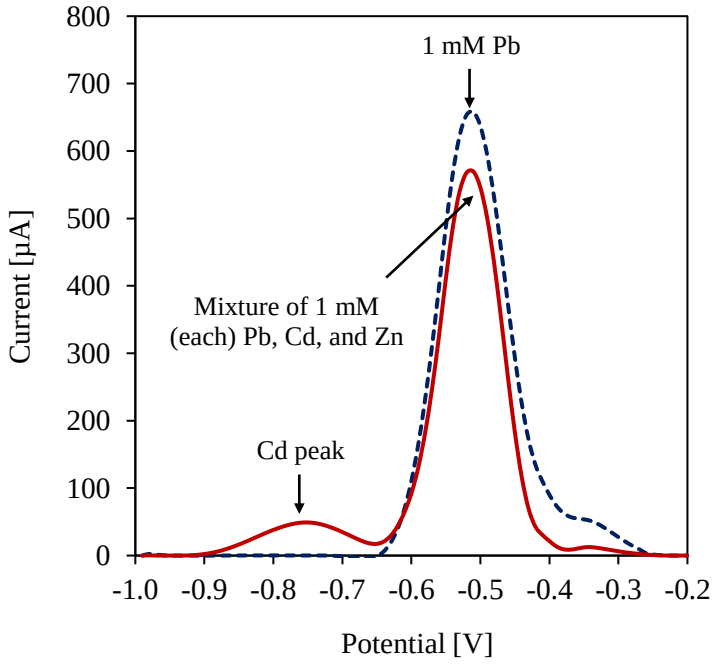

Figure 4-17. Interference effect of 1 mM Pb, Cd, and Zn (mixed) compared to 1 mM Pb alone.

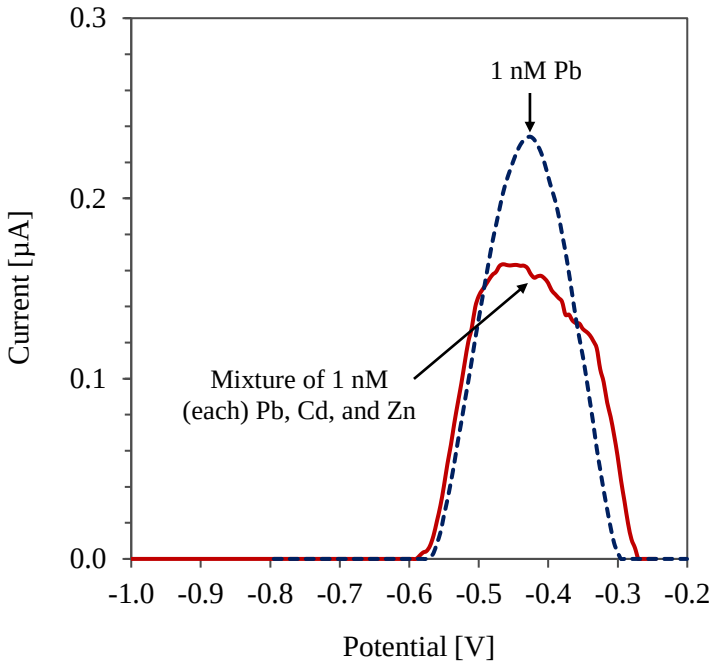

Figure 4-18. Interference effect of 1 nM Pb, Cd, and Zn (mixed) compared to 1 nM Pb alone.

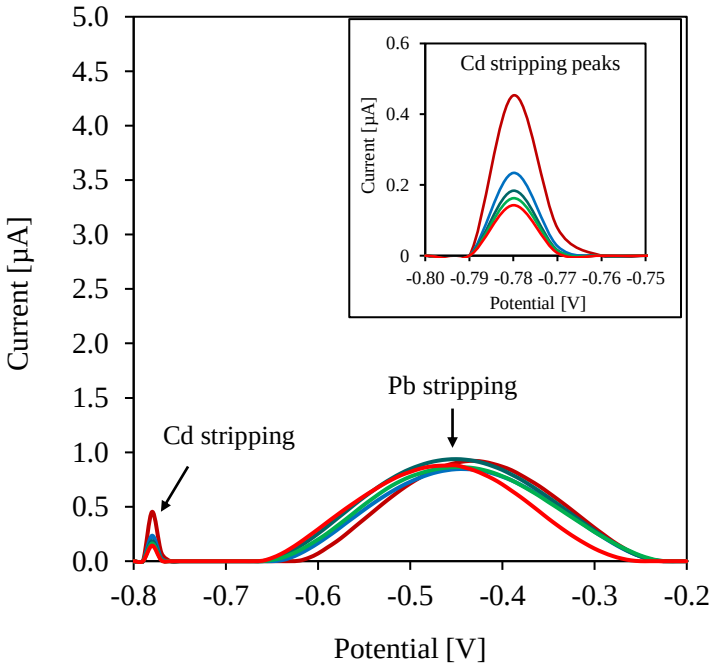

Figure 4-19. ASV of fixed 5 nM Pb with increasing concentrations of Cd in steps of 1 nM, 10 nM, 100 nM, 1 μM, 10 μM, and 100 μM. Inset shows the Cd stripping peaks in magnified scale.

4.6 Limitations of measurement

Each of the fabricated sensors was only used with a single electrolyte concentration as flushing a sensor with water for reuse may not entirely remove Pb from previous experiment. For this reason, no hysteresis study was performed in this work. Instead, each dataset used to calibrate the sensors was repeated for 10 times at every concentration. Also, long term temporal response of the sensor has not been investigated in this work because the soluble layer of $CuCl_2$ on the RE dissolved in buffer during ageing study.

The pH dependent response of the sensor was not studied in this work. Also, pH 5.2 was used for all sensing experiments instead of pH 6 – 8 that is typical of surface water. In fact, performing experiments in a neutral pH condition is not always necessary since the method of standard addition used to measure the unknown analyte concentration can always be spiked with standard solutions of desired pH value. The temperature dependency of the sensor is left as a future work where we propose the integration of a stage microheater to the sensor in Chapter 5. This will provide more reliable data rather than performing the same experiment at this development stage because a 100 µL sample at 40 °C would rapidly cool down to room temperature unless constantly heated.

Chapter 5

Conclusions and future work

5.1 Conclusions

Existing laboratory-based techniques to identify the dissolved lead contents in drinking water are highly accurate and reliable. However, these techniques cannot address the point-of-care needs for water quality monitoring in remote areas and in underdeveloped countries. Although these time- and labor- intensive, and costly analytical techniques have been substituted with low-cost electrochemical methods, the need for a truly low-cost and fully-integrated sensor still exists. This is primarily because electrochemical sensors require a combination of metal electrodes to enable sensitive detection of an analyte, but integration of heterogeneous materials on a planar substrate often leads to increased process complexities. Furthermore, miniaturization of these sensors reduces the sensor's effective surface area which must be compensated by the fabrication of surface-enhancing nanostructures on the electrode surface. Some of these electrode materials are expensive and not ideal for disposable use. Most materials are also limited by their fabrication process compatibilities that require a tradeoff between electrode film thickness, substrate adhesion,

stability, and performance. Specifically, thick film electrodes are often desirable as they do not get consumed during electrochemical sensing. Thick films also offer bulk material properties such as higher conductivity, but they are difficult and inefficient to fabricate with processes that are more compatible with thin-films. Simpler processes like screen-printing can produce thick-film electrodes, but screen-printed electrodes often contain a non-conductive polymer-based binder that enhances substrate adhesion at the cost of shielding the electrode's electrochemical sensitivity. Therefore, the design of a high-performance and cost-effective electrochemical sensor requires careful consideration of the electrode material, dimensions, and fabrication process.

This thesis focused on the design, fabrication, and characterization of a microfabricated lead sensor based on inexpensive Cu foil and polymer. To fabricate the all-Cu-based electrodes of this sensor, we developed a direct bonding process for integrating thick Cu foil to a polymer using less stringent process parameters. The resulting specimen exhibited a strong bond strength that prevented etchant-caused Cu foil undercut during electrode fabrication. The mechanical flexibility of the specimen allowed a one-step transfer of a polyester toner-based electrode mask on Cu using a laser jet printer. This made the fabrication process much simpler, cheaper, and faster compared to conventionally used metal evaporation and photolithography techniques. The developed sensor was based on a three-electrode setup and could sensitively detected 0.2 μg/L (0.2 ppb) Pb in 30 s, even in the presence of interfering Cd and Zn ions. To the best of our knowledge, this is the most rapid detection of such low levels of Pb demonstrated by an all-Cu-based electrochemical sensor.

In Chapter 1, we introduced the importance and background of water quality monitoring. The developed sensor has a detection limit that is much lower than the existing (10 μg/L) and proposed (5 μg/L) water safety guidelines for Pb. Therefore, the fabricated sensor will find applications in environmental research as well as scientific researches. We also briefly introduced the various conventional, traditional, and recent approaches for Pb sensing, followed by identification of research motivations and challenges for this work.

In Chapter 2, a comprehensive review of electrochemical Pb sensors was presented. This review identified several preliminary design factors that were considered and further optimized during sensor fabrication. The review was prepared with existing and future researchers of our group in mind, and to give them a note of electrochemical sensing principles and surface activated bonding fundamentals.

In Chapter 3, we described the SAB process parameters optimization for Cu/LCP bonding followed by outlining the sensor fabrication process. Thick foils of rolled-annealed Cu were directly bonded to a polymer substrate followed by electrode fabrication and packaging to realize a fully-integrated sensor. The demonstrated process may have excellent production feasibility considering the low-cost, high-throughput, and short time required for developing Pb sensors in bulk quantity. Finally, we characterized the plasma-assisted bond formation between Cu sheet and polymer. Plasma treatment resulted in highly hydrophilic Cu and LCP surfaces covered with OH^- dangling sites, which are easy to bond. We observed that thermally grown Cu_2O nanoparticles on the Cu surface might diffuse into LCP when heated under external contact pressure. We believe that these fundamentals will allow further integration of novel materials using SAB.

In Chapter 4, we discussed on the feasibility and performance of Cu-based sensors for detection of trace Pb ions in water. The sensing performance of Cu/LCP-based sensors was compared with that of commercial Cu/PI laminate-based sensors. We demonstrated that the fabricated sensors could sensitively detect 1 nM Pb from only a 100 μL sample in 30 s. This was possible because of the high conductivity of rolled-annealed Cu electrodes, but also due to the successful optimization of sensing process parameters that resulted in a good tradeoff between faster response, lower signal variation, strong current, and resistance to interfering Cd^{2+} and Zn^{2+} ions. The sensor performance has been compared with 18 other works reported in the literature.

5.2 Future work

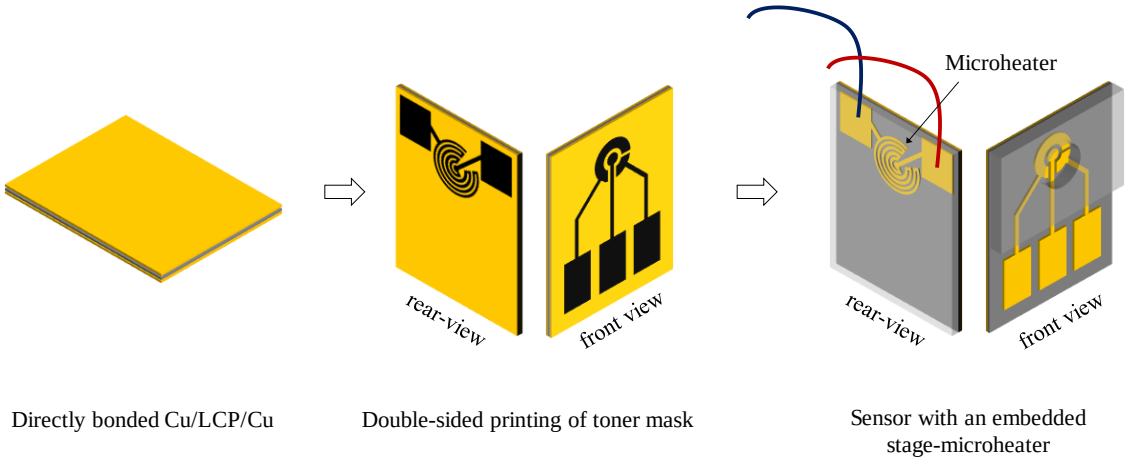

Figure 5-1. 3D-integration of a microheater at the rear side of a directly bonded double-side Cu clad-based Pb sensor. The sensor can be fabricated in a similar way using SAB and laser-printer-assisted mask transfer.

This work creates several research opportunities in the field of low-cost, high-performance electrochemical sensor fabrication and integrated systems development. For example, it has been shown that increasing the temperature of the electrolyte can increase the redox reaction kinetics in a three-electrode system, which results in an enhancement of the stripping peaks during voltammetric detection of ions [113]. It would be interesting to explore if a Cu-coil microheater fabricated on the rear side of the sensor (Fig. 5-1) can further enhance the sensitivity of the Pb sensor. This could be achieved by directly-bonding Cu foils on both sides of a polymer substrate to obtain a double-sided Cu clad, followed by a similar fabrication approach as the Pb sensor. For the readout electronics part of a proposed handheld system, a PCB board featuring a low-cost LMP91000 programmable analog front-end potentiostat chip (Texas Instruments) and an embedded microprocessor

needs to be developed (Fig. 5-2). The developed sensor can interface directly to the LMP91000 to realize a fully functional, low-cost system.

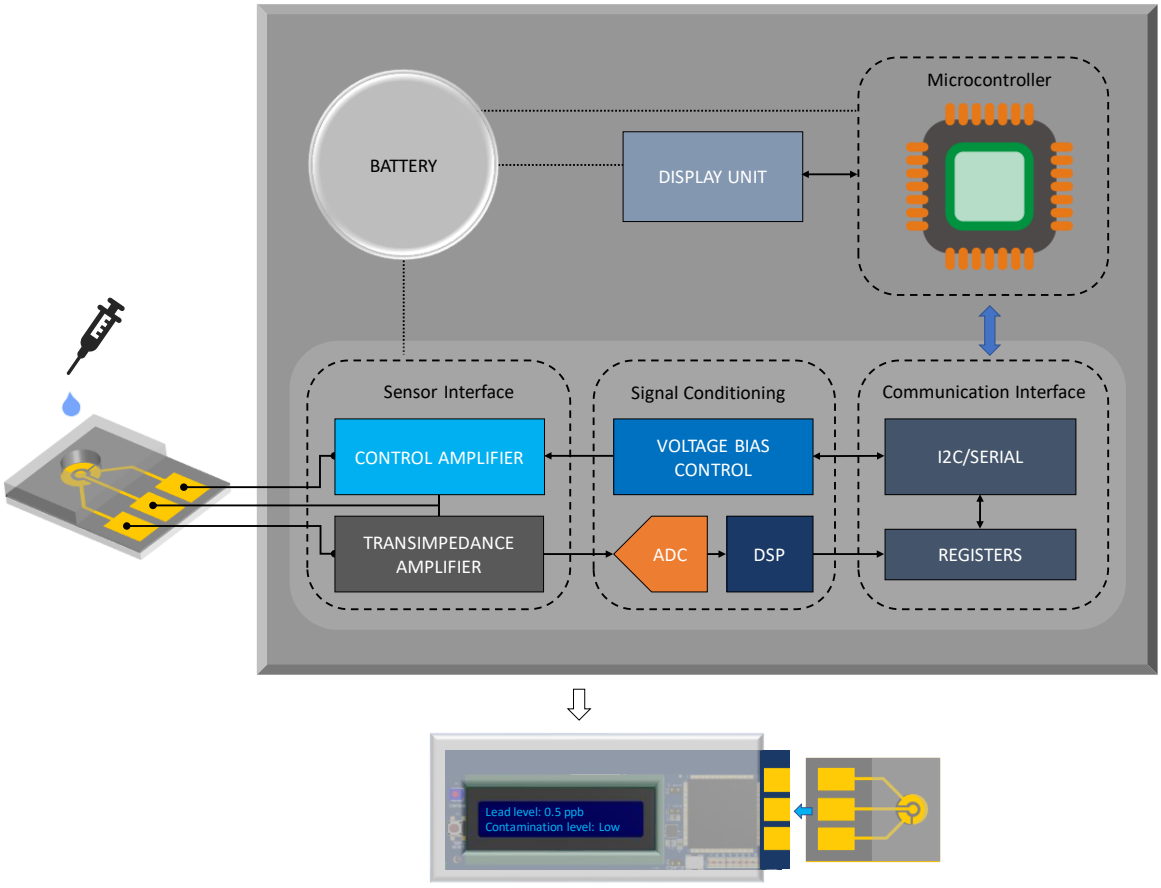

Figure 5-2. Proposed low-cost embedded system for water quality monitoring using fabricated sensor.

A further development of this work could be the mathematical modeling of sensor performance (sensitivity, peak current, potential drift, LOD etc.) in terms of varying electrode size and geometry, voltammetry parameters such as deposition time, and electrolyte conditions (pH, temperature, and presence of interfering ions such as chloride

and other heavy metals). These will help researchers develop more robust micro- and nano-sensors that can self-calibrate and compensate for water parameter changes and still provide accurate and reliable results. If such models are embedded in the on-board processors of the readout electronics unit, multi-analyte sensing could be yet another possibility.

The use of a $Cu/CuCl_2$ quasi-reference electrode is a relatively new concept. Over the years, there have been several researches that aimed at improving the stability and lifetime of reference electrodes. One of the interesting advances in this category is the use of a microfluidic channel to introduce saturated inner filling solution to miniaturized reference electrodes. The fabricated sensor already features a PDMS encapsulant where a separate compartment for the $Cu/CuCl_2$ RE may be fabricated and filled with concentrated KCl solution immediately before introducing the test solution. A diffusion membrane can then be used to connect between the RE and the test electrolyte chambers. This approach will reduce potential drift arising from surface potential changes of the RE.

The work presented in this thesis was a fresh approach to fabricating a fully-integrated electrochemical sensor that is easy-to-use, low-cost, and offers rapid detection of trace analyte. In the process of developing the sensor, we demonstrated a novel direct bonding approach for heterogenous integration of Cu thick films on polymer. We believe that this work will be useful for sensor development in the field of environmental research.

References

[1] Gumpu, M. B., Sethuraman, S., Krishnan, U. M., & Rayappan, J. B. B. (2015). A review on detection of heavy metal ions in water–An electrochemical approach. *Sensors and actuators B: chemical*, *213*, 515-533.

[2] Goyer, R. A. (1993). Lead toxicity: current concerns. *Environmental Health Perspectives*, *100*, 177.

[3] Steenland, K., & Boffetta, P. (2000). Lead and cancer in humans: where are we now?. *American journal of industrial medicine*, *38*(3), 295-299.

[4] Settle, D. M., & Patterson, C. C. (1980). Lead in albacore: guide to lead pollution in Americans. *Science*, *207*(4436), 1167-1176.

[5] Canfield, R. L., Henderson Jr, C. R., Cory-Slechta, D. A., Cox, C., Jusko, T. A., & Lanphear, B. P. (2003). Intellectual impairment in children with blood lead concentrations below 10 μg per deciliter. *New England journal of medicine*, *348*(16), 1517-1526.

[6] Lanphear, B. P., Dietrich, K., Auinger, P., & Cox, C. (2000). Cognitive deficits associated with blood lead concentrations< 10 microg/dL in US children and adolescents. *Public health reports*, *115*(6), 521.

[7] Kuang, H., Xing, C., Hao, C., Liu, L., Wang, L., & Xu, C. (2013). Rapid and highly sensitive detection of lead ions in drinking water based on a strip immunosensor. *Sensors*, *13*(4), 4214-4224.

[8] Tüzen, M. (2003). Determination of heavy metals in fish samples of the middle Black Sea (Turkey) by graphite furnace atomic absorption spectrometry. *Food chemistry*, *80*(1), 119-123.

[9] Jenner, G. A., Longerich, H. P., Jackson, S. E., & Fryer, B. J. (1990). ICP-MS—a powerful tool for high-precision trace-element analysis in earth sciences: evidence from analysis of selected USGS reference samples. *Chemical Geology*, *83*(1-2), 133-148.

[10] Wang, J. (2005). Stripping analysis at bismuth electrodes: a review. *Electroanalysis: An International Journal Devoted to Fundamental and Practical Aspects of Electroanalysis*, *17*(15-16), 1341-1346.

[11] Harvey, D. (2016). Analytical Chemistry 2.0.

[12] Li, J., & Lu, Y. (2000). A highly sensitive and selective catalytic DNA biosensor for lead ions. *Journal of the American Chemical Society*, *122*(42), 10466-10467.

[13] Kim, H. N., Ren, W. X., Kim, J. S., & Yoon, J. (2012). Fluorescent and colorimetric sensors for detection of lead, cadmium, and mercury ions. *Chemical Society Reviews*, *41*(8), 3210-3244.

[14] Xiao, Y., Rowe, A. A., & Plaxco, K. W. (2007). Electrochemical detection of parts-per-billion lead via an electrode-bound DNAzyme assembly. *Journal of the American Chemical Society*, *129*(2), 262-263.

[15] Teh, H. B., Li, H., & Li, S. F. Y. (2014). Highly sensitive and selective detection of Pb 2+ ions using a novel and simple DNAzyme-based quartz crystal microbalance with dissipation biosensor. *Analyst*, *139*(20), 5170-5175.

[16] Cobben, P. L., Egberink, R. J., Bomer, J. G., Bergveld, P., Verboom, W., & Reinhoudt, D. N. (1992). Transduction of selective recognition of heavy metal ions by chemically modified field effect transistors (CHEMFETs). *Journal of the American Chemical Society*, *114*(26), 10573-10582.

[17] Maity, A., Sui, X., Tarman, C. R., Pu, H., Chang, J., Zhou, G., ... & Chen, J. (2017). Pulse-driven capacitive lead ion detection with reduced graphene oxide field-effect

transistor integrated with an analyzing device for rapid water quality monitoring. *ACS sensors*, *2*(11), 1653-1661.

[18] Guselnikova, O., Postnikov, P., Erzina, M., Kalachyova, Y., Švorčík, V., & Lyutakov, O. (2017). Pretreatment-free selective and reproducible SERS-based detection of heavy metal ions on DTPA functionalized plasmonic platform. *Sensors and Actuators B: Chemical*, *253*, 830-838.

[19] Bakker, E., & Telting-Diaz, M. (2002). Electrochemical sensors. *Analytical chemistry*, *74*(12), 2781-2800.

[20] Privett, B. J., Shin, J. H., & Schoenfisch, M. H. (2008). Electrochemical sensors. *Analytical chemistry*, *80*(12), 4499-4517.

[21] Kimmel, D. W., LeBlanc, G., Meschievitz, M. E., & Cliffel, D. E. (2011). Electrochemical sensors and biosensors. *Analytical chemistry*, *84*(2), 685-707.

[22] Kovacs, G. T., Storment, C. W., & Kounaves, S. P. (1995). Microfabricated heavy metal ion sensor. *Sensors and Actuators B: Chemical*, *23*(1), 41-47.

[23] Haddara, Y. M., & Howlader, M. M. (2018). Integration of heterogeneous materials for wearable sensors. *Polymers*, *10*(1), 60.

[24] Xuan, X., Hossain, M. F., & Park, J. Y. (2016). A fully integrated and miniaturized heavy-metal-detection sensor based on micro-patterned reduced graphene oxide. *Scientific Reports*, *6*, 33125.

[25] Kuila, T., Bose, S., Khanra, P., Mishra, A. K., Kim, N. H., & Lee, J. H. (2011). Recent advances in graphene-based biosensors. *Biosensors and Bioelectronics*, *26*(12), 4637-4648.

[26] Li, J., Guo, S., Zhai, Y., & Wang, E. (2009). High-sensitivity determination of lead and cadmium based on the Nafion-graphene composite film. *Analytica chimica acta*, *649*(2), 196-201.

[27] Chen, L., Li, Z., Meng, Y., Zhang, P., Su, Z., Liu, Y., ... & Yao, S. (2014). Sensitive square wave anodic stripping voltammetric determination of Cd2+ and Pb2+ ions at Bi/Nafion/overoxidized 2-mercaptoethanesulfonate-tethered polypyrrole/glassy carbon electrode. *Sensors and Actuators B: Chemical*, *191*, 94-101.

[28] Walcarius, A. (1998). Analytical Applications of Silica-Modified Electrodes–A Comprehensive Review. *Electroanalysis: An International Journal Devoted to Fundamental and Practical Aspects of Electroanalysis*, *10*(18), 1217-1235.

[29] Kopanica, M., & Stará, V. (1991). Silica gel modified carbon composite electrodes. *Electroanalysis*, *3*(1), 13-16.

[30] Gunasingham, H., & Dalangin, R. R. (1991). Anodic stripping voltammetry of lead using a copper-mercury film electrode. *Analytica chimica acta*, *246*(2), 309-313.

[31] Wang, J., Lu, J., Hocevar, S. B., & Ogorevc, B. (2001). Bismuth-coated screen-printed electrodes for stripping voltammetric measurements of trace lead. *Electroanalysis: An International Journal Devoted to Fundamental and Practical Aspects of Electroanalysis*, *13*(1), 13-16.

[32] Lee, G. J., Kim, C. K., Lee, M. K., & Rhee, C. K. (2010). Simultaneous voltammetric determination of Zn, Cd and Pb at bismuth nanopowder electrodes with various particle size distributions. *Electroanalysis: An International Journal Devoted to Fundamental and Practical Aspects of Electroanalysis*, *22*(5), 530-535.

[33] Hwang, G. H., Han, W. K., Park, J. S., & Kang, S. G. (2008). An electrochemical sensor based on the reduction of screen-printed bismuth oxide for the determination of trace lead and cadmium. *Sensors and Actuators B: Chemical*, *135*(1), 309-316.

[34] Hocevar, S. B., Wang, J., Deo, R. P., & Ogorevc, B. (2002). Potentiometric stripping analysis at bismuth-film electrode. *Electroanalysis: An International Journal Devoted to Fundamental and Practical Aspects of Electroanalysis*, *14*(2), 112-115.

[35] Rajamani, A. R., Ragula, U. B. R., Kothurkar, N., & Rangarajan, M. (2014). Nano- and micro-hexagons of bismuth on polycrystalline copper: electrodeposition and heavy metal sensing. *CrystEngComm*, *16*(10), 2032-2038.

[36] Kang, W., Pei, X., Rusinek, C. A., Bange, A., Haynes, E. N., Heineman, W. R., & Papautsky, I. (2017). Determination of lead with a copper-based electrochemical sensor. *Analytical chemistry*, *89*(6), 3345-3352.

[37] Ouyang, R., Zhu, Z., Tatum, C. E., Chambers, J. Q., & Xue, Z. L. (2011). Simultaneous stripping detection of Zn (II), Cd (II) and Pb (II) using a bimetallic Hg–Bi/single-walled carbon nanotubes composite electrode. *Journal of electroanalytical chemistry*, *656*(1-2), 78-84.

[38] Pumera, M., Merkoçi, A., & Alegret, S. (2006). Carbon nanotube-epoxy composites for electrochemical sensing. *Sensors and Actuators B: Chemical*, *113*(2), 617-622.

[39] Culková, E., Švorc, Ľ., Tomčík, P., Durdiak, J., Rievaj, M., Bustin, D., ... & Lokaj, J. (2013). Boron-Doped Diamond Electrode as Sensitive and Selective Green Electroanalytical Tool for Heavy Metals Environmental Monitoring: Zinc Detection in Rubber Industry Waste. *Polish Journal of Environmental Studies*, *22*(5).

[40] Zhang, T., Li, C., Mao, B., & An, Y. (2015). Determination of Cd 2+ by ultrasound-assisted square wave anodic stripping voltammetry with a boron-doped diamond electrode. *Ionics*, *21*(6), 1761-1769.

[41] Toghill, K. E., Xiao, L., Wildgoose, G. G., & Compton, R. G. (2009). Electroanalytical determination of cadmium (II) and lead (II) using an antimony nanoparticle modified boron-doped diamond electrode. *Electroanalysis: An International Journal Devoted to Fundamental and Practical Aspects of Electroanalysis*, *21*(10), 1113-1118.

[42] Arantes, T. M., Sardinha, A., Baldan, M. R., Cristovan, F. H., & Ferreira, N. G. (2014). Lead detection using micro/nanocrystalline boron-doped diamond by square-wave anodic stripping voltammetry. *Talanta*, *128*, 132-140.

[43] Jiang, Y., Liu, D., Jiang, Z., Mao, B., Ma, X., & Li, Q. (2014). Investigation on electrochemically cathodic polarization of boron-doped diamond electrodes and its influence on lead ions analysis. *Journal of The Electrochemical Society*, *161*(6), H410-H415.

[44] Bonfil, Y., Brand, M., & Kirowa-Eisner, E. (2000). Trace determination of mercury by anodic stripping voltammetry at the rotating gold electrode. *Analytica chimica acta*, *424*(1), 65-76.

[45] Lin, W. C., Li, Z., & Burns, M. A. (2017). A drinking water sensor for lead and other heavy metals. *Analytical chemistry*, *89*(17), 8748-8756.

[46] Avuthu, S. G. R., Narakathu, B. B., Eshkeiti, A., Emamian, S., Bazuin, B. J., Joyce, M., & Atashbar, M. Z. (2014, November). Detection of heavy metals using fully printed three electrode electrochemical sensor. In *SENSORS, 2014 IEEE* (pp. 669-672). IEEE.

[47] Redhwan, T. Z., Alam, A. U., Haddara, Y. M., & Howlader, M. M. (2018). Copper and liquid crystal polymer bonding towards lead sensing. *Japanese Journal of Applied Physics*, *57*(2S1), 02BB03.

[48] Howlader, M. M., Alam, A. U., Sharma, R. P., & Deen, M. J. (2015). Materials analyses and electrochemical impedance of implantable metal electrodes. *Physical Chemistry Chemical Physics*, *17*(15), 10135-10145.

[49] Heidelbach, F., Wenk, H. R., Chen, S. R., Pospiech, J., & Wright, S. I. (1996). Orientation and misorientation characteristics of annealed, rolled and recrystallized copper. *Materials Science and Engineering: A*, *215*(1-2), 39-49.

[50] Merchant, H. D., Liu, W. C., Giannuzzi, L. A., & Morris, J. G. (2004). Grain structure of thin electrodeposited and rolled copper foils. *Materials characterization*, *53*(5), 335-360.

[51] Brist, G., Hall, S., Clouser, S., & Liang, T. (2005, February). Non-classical conductor losses due to copper foil roughness and treatment. In *2005 IPC Electronic Circuits World Convention*.

[52] Coonrod, J. (2012). Different copper foils for different reasons. *The PCB Magazine*, 60-64.

[53] Howlader, M. M. R., Doyle, T. E., Mohtashami, S., & Kish, J. R. (2013). Charge transfer and stability of implantable electrodes on flexible substrate. *Sensors and Actuators B: Chemical*, *178*, 132-139.

[54] Howlader, M. M. R., Suga, T., Takahashi, A., Saijo, K., Ozawa, S., & Nanbu, K. (2005). Surface activated bonding of LCP/Cu for electronic packaging. *Journal of materials science*, *40*(12), 3177-3184.

[55] Howlader, M. M. R., Iwashita, M., Nanbu, K., Saijo, K., & Suga, T. (2005). Enhanced Cu/LCP adhesion by pre-sputter cleaning prior to Cu deposition. *IEEE transactions on advanced packaging*, *28*(3), 495-502.

[56] Howlader, M. M. R., Selvaganapathy, P. R., Deen, M. J., & Suga, T. (2011). Nanobonding technology toward electronic, fluidic, and photonic systems integration. *IEEE Journal of Selected Topics in Quantum Electronics*, *17*(3), 689-703.

[57] Maloy, J. T. (1983). Factors affecting the shape of current-potential curves.

[58] Laschi, S., Palchetti, I., & Mascini, M. (2006). Gold-based screen-printed sensor for detection of trace lead. *Sensors and Actuators B: Chemical*, *114*(1), 460-465.

[59] Wang, Z., Wang, H., Zhang, Z., & Liu, G. (2014). Electrochemical determination of lead and cadmium in rice by a disposable bismuth/electrochemically reduced graphene/ionic liquid composite modified screen-printed electrode. *Sensors and Actuators B: Chemical*, *199*, 7-14.

[60] Bui, M. P. N., Li, C. A., Han, K. N., Pham, X. H., & Seong, G. H. (2012). Electrochemical determination of cadmium and lead on pristine single-walled carbon nanotube electrodes. *Analytical Sciences*, *28*(7), 699-704.

[61] Hwang, G. H., Han, W. K., Park, J. S., & Kang, S. G. (2008). Determination of trace metals by anodic stripping voltammetry using a bismuth-modified carbon nanotube electrode. *Talanta*, *76*(2), 301-308.

[62] Lee, G. J., Kim, C. K., Lee, M. K., & Rhee, C. K. (2010). Simultaneous voltammetric determination of Zn, Cd and Pb at bismuth nanopowder electrodes with various particle size distributions. *Electroanalysis: An International Journal Devoted to Fundamental and Practical Aspects of Electroanalysis*, *22*(5), 530-535.

[63] Urbanová, V., Bartoš, M., Vytřas, K., & Kuhn, A. (2010). Porous bismuth film electrodes for signal increase in anodic stripping voltammetry. *Electroanalysis*, *22*(13), 1524-1530.

[64] Ouyang, R., Zhu, Z., Tatum, C. E., Chambers, J. Q., & Xue, Z. L. (2011). Simultaneous stripping detection of Zn (II), Cd (II) and Pb (II) using a bimetallic Hg–Bi/single-walled carbon nanotubes composite electrode. *Journal of electroanalytical chemistry*, *656*(1-2), 78-84.

[65] Sahoo, P. K., Panigrahy, B., Sahoo, S., Satpati, A. K., Li, D., & Bahadur, D. (2013). In situ synthesis and properties of reduced graphene oxide/Bi nanocomposites: As an electroactive material for analysis of heavy metals. *Biosensors and Bioelectronics*, *43*, 293-296.

[66] Wang, J., Lu, J., Hocevar, S. B., & Ogorevc, B. (2001). Bismuth-coated screen-printed electrodes for stripping voltammetric measurements of trace lead. *Electroanalysis: An International Journal Devoted to Fundamental and Practical Aspects of Electroanalysis*, *13*(1), 13-16.

[67] Pei, X., Kang, W., Yue, W., Bange, A., Heineman, W. R., & Papautsky, I. (2014). Disposable copper-based electrochemical sensor for anodic stripping voltammetry. *Analytical chemistry*, *86*(10), 4893-4900.

[68] Jothimuthu, P., Wilson, R. A., Herren, J., Haynes, E. N., Heineman, W. R., & Papautsky, I. (2011). Lab-on-a-chip sensor for detection of highly electronegative heavy metals by anodic stripping voltammetry. *Biomedical microdevices*, *13*(4), 695-703.

[69] Sandison, M. E., Anicet, N., Glidle, A., & Cooper, J. M. (2002). Optimization of the geometry and porosity of microelectrode arrays for sensor design. *Analytical chemistry*, *74*(22), 5717-5725.

[70] Zhang, W., Zhang, H., Williams, S. E., & Zhou, A. (2015). Microfabricated three-electrode on-chip PDMS device with a vibration motor for stripping voltammetric detection of heavy metal ions. *Talanta*, *132*, 321-326.

[71] Wolfrum, B., Kätelhön, E., Yakushenko, A., Krause, K. J., Adly, N., Hüske, M., & Rinklin, P. (2016). Nanoscale electrochemical sensor arrays: redox cycling amplification in dual-electrode systems. *Accounts of chemical research*, *49*(9), 2031-2040.

[72] Kätelhön, E., Mayer, D., Banzet, M., Offenhäusser, A., & Wolfrum, B. (2014). Nanocavity crossbar arrays for parallel electrochemical sensing on a chip. *Beilstein journal of nanotechnology*, *5*, 1137.

[73] Wan, H., Ha, D., Zhang, W., Zhao, H., Wang, X., Sun, Q., & Wang, P. (2014). Design of a novel hybrid sensor with microelectrode array and LAPS for heavy metal determination using multivariate nonlinear calibration. *Sensors and Actuators B: Chemical*, *192*, 755-761.

[74] Kokkinos, C., Economou, A., & Raptis, I. (2012). Microfabricated disposable lab-on-a-chip sensors with integrated bismuth microelectrode arrays for voltammetric determination of trace metals. *Analytica chimica acta*, *710*, 1-8.

[75] Kokkinos, C., & Economou, A. (2014). Disposable microfabricated 3-electrode electrochemical devices with integrated antimony working electrode for stripping voltammetric determination of selected trace metals. *Sensors and Actuators B: Chemical*, *192*, 572-577.

[76] Feng, Q. M., Zhang, Q., Shi, C. G., Xu, J. J., Bao, N., & Gu, H. Y. (2013). Using nanostructured conductive carbon tape modified with bismuth as the disposable working electrode for stripping analysis in paper-based analytical devices. *Talanta*, *115*, 235-240.

[77] Jung, W., Jang, A., Bishop, P. L., & Ahn, C. H. (2011). A polymer lab chip sensor with microfabricated planar silver electrode for continuous and on-site heavy metal measurement. *Sensors and Actuators B: Chemical*, *155*(1), 145-153.

[78] Wei, H., Sun, J. J., Xie, Y., Lin, C. G., Wang, Y. M., Yin, W. H., & Chen, G. N. (2007). Enhanced electrochemical performance at screen-printed carbon electrodes by a new pretreating procedure. *Analytica chimica acta*, *588*(2), 297-303.

[79] Howlader, M. M. R., Selvaganapathy, P. R., Deen, M. J., & Suga, T. (2011). Nanobonding technology toward electronic, fluidic, and photonic systems integration. *IEEE Journal of Selected Topics in Quantum Electronics*, *17*(3), 689-703.

[80] Kim, T. H., Howlader, M. M. R., Itoh, T., & Suga, T. (2003). Room temperature Cu–Cu direct bonding using surface activated bonding method. *Journal of Vacuum Science & Technology A: Vacuum, Surfaces, and Films*, *21*(2), 449-453.

[81] Howlader, M. M. R., Watanabe, T., & Suga, T. (2001). Investigation of the bonding strength and interface current of p-Si/n-GaAs wafers bonded by surface activated bonding at room temperature. *Journal of Vacuum Science & Technology B: Microelectronics and Nanometer Structures Processing, Measurement, and Phenomena*, *19*(6), 2114-2118.

[82] Yu, T., Howlader, M. R., Zhang, F., & Bakr, M. (2011). Nanobonding for multi-junction solar cells at room temperature. *ECS Transactions*, *35*(2), 3-10.

[83] Howlader, M. M. R., Suga, T., Zhang, F., Lee, T. H., & Kim, M. J. (2010). Interfacial behavior of surface activated p-GaP/n-GaAs bonded wafers at room temperature. *Electrochemical and Solid-State Letters*, *13*(3), H61-H65.

[84] Howlader, M. M. R., Kaga, T., & Suga, T. (2010). Investigation of bonding strength and sealing behavior of aluminum/stainless steel bonded at room temperature. *Vacuum*, *84*(11), 1334-1340.

[85] Howlader, M. M. R., Okada, H., Kim, T. H., Itoh, T., & Suga, T. (2004). Wafer level surface activated bonding tool for MEMS packaging. *Journal of The Electrochemical Society*, *151*(7), G461-G467.

[86] Matsumae, T., Fujino, M., & Suga, T. (2015). Room-temperature bonding method for polymer substrate of flexible electronics by surface activation using nano-adhesion layers. *Japanese Journal of Applied Physics*, *54*(10), 101602.

[87] Howlader, M. M. R., Suehara, S., & Suga, T. (2006). Room temperature wafer level glass/glass bonding. *Sensors and Actuators A: Physical*, *127*(1), 31-36.

[88] Howlader, M. M. R., Suehara, S., Takagi, H., Kim, T. H., Maeda, R., & Suga, T. (2006). Room-temperature microfluidics packaging using sequential plasma activation process. *IEEE transactions on advanced packaging*, *29*(3), 448-456.

[89] Howlader, M. M. R., Suga, T., Itoh, H., Lee, T. H., & Kim, M. J. (2009). Role of heating on plasma-activated silicon wafers bonding. *Journal of The Electrochemical Society*, *156*(11), H846-H851.

[90] Kibria, M. G., Zhang, F., Lee, T. H., Kim, M. J., & Howlader, M. M. R. (2010). Comprehensive investigation of sequential plasma activated Si/Si bonded interfaces for nano-integration on the wafer scale. *Nanotechnology*, *21*(13), 134011.

[91] Howlader, M. M. R., Kibria, M. G., Zhang, F., & Kim, M. J. (2010). Hybrid plasma bonding for void-free strong bonded interface of silicon/glass at 200 C. *Talanta*, *82*(2), 508-515.

[92] Howlader, M. M. R., Kibria, M. G., & Zhang, F. (2010). Hybrid plasma bonding of germanium and glass wafers at low temperature. *Materials Letters*, *64*(13), 1532-1535.

[93] Alam, A. U., Qin, Y., Howlader, M. M., & Deen, M. J. (2016). Direct bonding of liquid crystal polymer to glass. *RSC Advances*, *6*(109), 107200-107207.

[94] Hin, T. Y., Liu, C., & Conway, P. P. (2009). Surface characterisation of plasma treated flexible substrates for waveguide-on-flex application. *Surface and Coatings Technology*, *203*(24), 3741-3749.

[95] Suni, T., Henttinen, K., Suni, I., & Mäkinen, J. (2002). Effects of plasma activation on hydrophilic bonding of Si and SiO2. *Journal of the Electrochemical Society*, *149*(6), G348-G351.

[96] Shinwari, M. W., Zhitomirsky, D., Deen, I. A., Selvaganapathy, P. R., Deen, M. J., & Landheer, D. (2010). Microfabricated reference electrodes and their biosensing applications. *Sensors*, *10*(3), 1679-1715.

[97] Li, X., Wu, N., Rojanasakul, Y., & Liu, Y. (2013). Selective stamp bonding of PDMS microfluidic devices to polymer substrates for biological applications. *Sensors and Actuators A: Physical*, *193*, 186-192.

[98] Nakamura, Y., Suzuki, Y., & Watanabe, Y. (1996). Effect of oxygen plasma etching on adhesion between polyimide films and metal. *Thin Solid Films*, *290*, 367-369.

[99] Nyquist, R. A., Putzig, C. L., & Leugers, M. A. (1996). *Handbook of Infrared and Raman Spectra of Inorganic Compounds and Organic Salts: Infrared Spectra*. Academic press.

[100] "Cuprous oxide", *Webbook.nist.gov*, 2017. [Online]. Available: http://bit.ly/2qInOL5

[101] Laokroekkiat, S., Hara, M., Nagano, S., & Nagao, Y. (2016). Metal–Organic Coordination Network Thin Film by Surface-Induced Assembly. *Langmuir*, *32*(26), 6648-6655.

[102] Inagaki, N. (2009). Role of polymer chain end groups in plasma modification for surface metallization of polymeric materials. *Polymer International*, *58*(6), 585-593.

[103] Ikeo, N., Iijima, Y., Niimura, N., Sigematsu, M., Tazawa, T., Matsumoto, S., ... & Nagasawa, Y. (1991). Handbook of X-ray photoelectron spectroscopy. *JEOL, Tokyo*, *71*.

[104] Beamson, G. (1992). High resolution XPS of organic polymers. *The Scienta ESCA 300 Database*.

[105] Moulder, J. F., Stickle, W. F., Sobol, P. E., & Bomben, K. D. Handbook of X-ray Photoelectron Spectroscopy (Physical Electronics, Inc., 1995). *Google Scholar*, 108.

[106] Howlader, M. M., Kagami, G., Lee, S. H., Wang, J. G., Kim, M. J., & Yamauchi, A. (2010). Sequential plasma-activated bonding mechanism of silicon/silicon wafers. *Journal of Microelectromechanical Systems*, *19*(4), 840-848.

[107] Redhwan, T. Z., Alam, A. U., Catalano, M., Wang, L., Kim, M. J., Haddara, Y. M., & Howlader, M. M. (2018). Direct bonding of copper and liquid crystal polymer. *Materials Letters*, *212*, 214-217.

[108] Koch, R., Hu, D., & Das, A. K. (2005). Compressive stress in polycrystalline Volmer-Weber films. *Physical review letters*, *94*(14), 146101.

[109] Floro, J. A., Chason, E., Cammarata, R. C., & Srolovitz, D. J. (2002). Physical origins of intrinsic stresses in Volmer–Weber thin films. *MRS bulletin*, *27*(1), 19-25.

[110] Shinwari, M. W., Zhitomirsky, D., Deen, I. A., Selvaganapathy, P. R., Deen, M. J., & Landheer, D. (2010). Microfabricated reference electrodes and their biosensing applications. *Sensors*, *10*(3), 1679-1715.

[111] Shrivastava, A., & Gupta, V. B. (2011). Methods for the determination of limit of detection and limit of quantitation of the analytical methods. *Chronicles of Young Scientists*, *2*(1), 21.

[112] Nestorović, S., Milićević, B., & Marković, D. (2002). Anneal hardening effect in sintered copper alloys. *Science of sintering*, *34*(2), 169-174.

[113] Aragay, G., Pons, J., & Merkoçi, A. (2011). Enhanced electrochemical detection of heavy metals at heated graphite nanoparticle-based screen-printed electrodes. *Journal of Materials Chemistry*, *21*(12), 4326-4331.